UNIVERSITÀ DI PARMA

UNIVERSITÀ DEGLI STUDI DI PARMA

DOTTORATO DI RICERCA IN
"TECNOLOGIE DELL'INFORMAZIONE"

CICLO XXXV

Applications of Laser Light: Scribing of Solar Cells and Treatment of Ocular Diseases

Coordinatore:
Chiar.mo Prof. Marco Locatelli

Tutore:
Chiar.ma Prof. Annamaria Cucinotta

Dottoranda: Wahida Chowdhury

October 2024

I dedicate my thesis to my daughter Ayzal and my husband Joy whose unwavering sacrifice, love, and support have been my foundation throughout this journey. Without their endless love, encouragement, and sacrifices, I would never be able to achieve my goal. Their companionship and inspiration have lifted me through challenging times. I am grateful and honored to have them. I appreciate everything that they have done for me.

Contents

List of Figures

List of Tables

Introduction

Over the last five decades, laser technology has encountered endless intricate development processes. Since the invention of the initial functional laser in 1960, which was engineered by American physicist Theodore Harold Maiman at Hughes Research Laboratories, laser technology has made significant progress and established widespread applications across numerous domains [1]. This radical achievement by Maiman is considered a milestone of the laser era, which intensely impacted several fields of science. The prompt advancement in laser technology has led to the innovation of special types of lasers and their applications [2][3]. The acronym of LASER stands for "light amplification by stimulated emission of radiation" [4]. One of the most significant characteristics of lasers is their ability to produce highly focused and coherent beams of light compared to conventional light sources. In various scientific experiments and research, the laser plays an important role by offering highly precise and focused light beams [4]. The laser can be described as a device that produces an extremely focused light, like an advanced flashlight. Yet, it varies from regular flashlight light in four fundamental aspects. The laser light is extremely intense, though few of them are less powerful. Thus, even certain low-power lasers that emit a few milli-watts can achieve significant brightness within a narrow beam just a millimeter wide in diameter, like natural light. However, a standard light bulb emits more light, and this spreads over an area. Some lasers can continuously produce several watts, while others can deliver trillions of watts in a pulse. Another important aspect of laser beams is their directionalities This can be depicted by the properties of producing narrow beams, that prevents laser lights to spread out as conventional beams of light [5].

The revolutionary transformation in the field of scientific research by using laser tools for precise measurements and many experimental setups has occurred [6]. Besides, in high-speed communication systems laser and optical fibers are integral components. Laser plays a crucial role in telecommunication such as fiber optics technologies that enable long-distance and high-speed communication networks. The medical field has profited intensively from lasers in surgeries, such as eye surgery, dermatological treatments [7], and dental treatments [8]. Integration of lasers provides many benefits in surgeries by reducing recovery time, patient rehabilitation, and improving the results of operations. Furthermore, with the help of different laser applications the industrial and manufacturing sectors have also advanced impressively. For instance, laser cutting, scribing, and welding to 3D printing and materials processing [9].

This research activity includes two main parts. The first activity of the project focuses on laser scribing on thin film solar cells (TFSC). This was undertaken in collaboration with a joint project between the Department of Engineering and Architecture of the University of Parma and IMEM-CNR, Institute of Materials for Electronics and Magnetism. Thin film solar cells offer a prospective approach for global and astronomical photovoltaic (PV) purposes consistently. Regarding the design and manufacturing of the devices, TFSC offers a wide range of possibilities. Several substrates like flexible, rigid, metallic, and insulating can be utilized in depositing various layers such as contacts, absorbers, reflectors, and others.

The deposition process on different substrates can be accomplished by employing respective techniques for example Physical Vapor Deposition (PVD), Chemical Vapor Deposition (CVD), Electrochemical Deposition (ECD), plasma-based methods, and hybrid approaches. This flexibility in the selection of materials and methods of different deposition techniques facilitates the modification and development of the layers to improve the performance of the devices drastically [10].

Nevertheless, the process of fabrication becomes challenging, and it requires precise control of this whole system during the production of large-area thin film devices which are specifically crucial for practical purposes [10]. Currently, in 2003 photovoltaic technology reached half a century [11]. After the revolutionary innovation of p-n junction silicon (Si) photovoltaic devices in 1954, a significant progression has

been introduced in the fields of science and technology of photovoltaic devices. This is mainly in the advancement of solar cell technology, and the methods that enable their functionality. Most progressive single-crystal silicon solar cells have 24% efficiency. That is considered a remarkable percentage compared to the theoretical value. Despite this fact, it is below the theoretical maximum efficiency which is 30% [12]. In 2002, global production of solar cells (single-crystal Si cells at about 40%, multicrystalline Si cells, and amorphous thin-film silicon cells at 51% and 8% respectively) exceeded 500 MWp [13]. In several applications, nearly 2 GW of solar cells is currently in use globally. Many developing and industrialized countries are trying persistently to grow their photovoltaic industries to use solar energy most effectively [14]. From the early stage of solar cell technology development, it is always challenging because of the high cost of silicon material. To overcome this issue, it is considered that the production of solar cells relies on the use of available inexpensive materials and cost-effective technologies. By employing an economical technique called the "Clevite process" the first Cu_2S / CdS thin/thick film was fabricated [15]. In this approach, only a few millimeters thick CdS film was deposited on a plastic substrate that was metal or metalized. After that, the layer of CdS surface was topotaxially transformed to Cu_2S by an etching process that involves acid and immersion in a heated solution of cupric chlorides. Thus, this process changes the properties and characteristics of the substrate [16]. The second part of the research work focused on the Laser light application for the treatment of ocular disease. Specifically, yellow fiber laser system for the treatment of eye diseases. In this part of the work analyzing the impact of numerical and experimental parameters on Dysprosium-doped yellow fiber lasers for the treatment of eye diseases is presented. The project is a collaboration with Politecnico di Torino, Politecnico di Milano, Università degli Studi di Modena, and Reggio Emilia.

In ophthalmology treatment application of laser light is globally well-recognized nowadays. This is because of the highly precise and controlled beam quality of different laser types. These unique properties of a special kind of laser light are structured and engineered for specific ocular treatments. These developments in laser design help to avoid damage to the eye tissues and deliver the most efficient results compared

to other conventional methods. Laser photocoagulation for the treatment of diabetic macular edema (DME) is highly accepted in many developed countries [17, 18]. Diabetic macular edema (DME), diabetic retinopathy is a common ocular disease that is age-related macular degeneration that causes vision loss over time. Photocoagulation is the most effective treatment for this kind of eye issue. It could be the only option for some patients with wet age-related macular degeneration (AMD). It depends on the condition of retinal vessels inside the eye condition. this method might help to prevent gradual eye loss. This also offers some challenges to photocoagulation. If the laser is not carefully handled it may cause scars and blind spots, bleeding into the eyes, and damage to retinal areas. Recent developments in laser photocoagulation technologies can overcome many challenges that were impossible by other conventional technology. A navigated laser system is one of the most significant inventions. also, other methods such as pattern scan laser systems [19], and subthreshold laser therapies are other options for this treatment [20, 21]. Multi imaging method makes this procedure more precise and more effective accurate for the targeted area of the eye. Yellow laser is typically a potential candidate for this kind of treatment. Photodynamic therapy is another way that includes light-sensitive drug injecting into the abnormal vessels. This therapy allows to extinguishment of the affected vessels. Rhegmatogenous retinal detachments and retinal tears are the most serious eye condition. many patients suffer from blindness and minimal improvements. This requires proper surgical treatments [22]. Glaucoma is another problem that is responsible for blindness. There are some treatments to overcome this situation. Laser procedures trabeculoplasty is mainly utilized to treat this issue [23]. This is considered as a traditional glaucoma surgery but many new techniques and tools or devices like glaucoma drainage device minimally invasive glaucoma surgery (MIGS) have been introduced [24]. YAG laser is also used for some ocular surgery. Phototherapeutic keratectomy is a technique to treat the corneal disorder. The femtosecond laser is used to minimize the superficial corneal opacity. and smooth the irregularities of the surface or cornea [25]. In the ophthalmology field lasers can be used in many ways. And the recent advancements in laser technologies in medical treatment have a significant role. The advantages of using a laser are the treatment and recovery time is much faster.

Precise and targeted areas can be treated. That allows for harmless surgery. Also, different available wavelengths can be used according to the needs and conditions of the patients. However, some challenges need to be considered. Sometimes surrounding tissues might be at risk if a very high-power laser is not carefully operated. Some treatments need to be repeated, and this causes harm to the eye [26].

For our analysis, a dysprosium-doped fiber laser has been modeled to analyze the laser parameters to achieve the highest efficiency and to observe the effects of different parameters on the output power.

This dissertation is structured as follows:

Chapter 1 introduces the fundamentals of solar cells and their applications in various fields. working principle of Photovoltaic cells and some types of PV cells has been briefly explained.

Chapter 2 describes the basics of the Laser scribing process on solar cells and available scribing techniques. Three different steps for laser scribing of thin film solar cells are also explained. A basic overview of the optical setup for our scribing experiments is demonstrated in this section.

Chapter 3 presents the results and discusses laser scribing for different solar cell samples. This technique is mainly applied to the following structures: standard CIGS solar cells on glass, PV cells with alternative absorbers (Sb_2Se_3) on glass, and innovative semi-transparent solar cells (CuInGaS) for tandems on silicon-based solar cells. This section demonstrates SEM analysis and EDAX measurements of laser scribing methods. The important parameters for the scribing process are mentioned.

Chapter 4 provides a basic review of fiber amplifiers and lasers. It demonstrates a dysprosium-doped ZBLAN fiber laser and analyzes the verification of the explicit forward time-centered spaced method. Finally, the theoretical analysis of dy-doped visible fiber lasers is investigated by varying physical and numerical parameters for the proposed fiber laser. Also, the effect of ESA and ASE is considered for the laser output power.

Chapter 1

Solar Cell Fundamentals

This chapter aims to highlight the fundamentals and operating principles of solar cells, including the p-n junction, the formation of the depletion region, and the behavior of a p-n junction solar cell under applied voltage. Furthermore, it provides an overview of various categories of solar cells.

1.1 Overview of Solar Cell Fundamentals

Sunlight is the most powerful, vast, unlimited, and oldest energy source. In recent years, the demand for renewable energy has drawn more attention to energy conversion technology since solar energy conversion plays a crucial role in overcoming the global crisis of progressively growing energy demands also, it is considered a sustainable approach that could lessen the dependency on fossil fuels responsible for global warming. One of the most promising and practical solutions is to convert solar power to electrical energy through a physical and chemical phenomenon, known as the photovoltaic (PV) effect [27, 28, 29]. To generate an environment-friendly source of electricity, the abundant source of sunlight could bring revolutions in the power supply system of domestic, industrial, and public consumers [28]. The solar cell works sustainably besides in many remote and off-grid areas where electricity is not available it can produce electricity. Furthermore, advanced modern science and

technologies offer many substitute methods for energy production.

The PV cell is an electronic device that directly converts sunlight to electrical energy, because of the electrical current flow between two different semiconductor layers, DC voltage is produced due to the exposure of the sunlight to the material [29]. While light rays irradiate the solar cell surface, they generate electric current and voltage. This technique requires a specific material that can absorb light which will excite electrons to higher energy states. The electron then discharges its energy in the external circuit before returning to the solar cell [30].

1.1.1 Objectives of using solar cell

Numerous materials and approaches can hypothetically accomplish the principles, necessary for photovoltaic energy transformation. Nevertheless, in practical circumstances, it is notable that almost all instances of photovoltaic energy conversion mostly depend on the deployment of semiconductor materials, which are fundamentally designed in the form of a p-n junction [30, 31]. Many unique properties make solar power attractive and promising. The major factors of solar power are they are eco-friendly, it generates clean energy and there are no Polluting exhalations, additionally, the construction is less complex, highly flexible, and durable since there are no moving components and no possibility of breaking down the structure. Besides being very easy to care for, solar cells require low maintenance, have a significantly long lifespan (20 to 30 years), and incur minimal operating expenses. Due to these advantages, rural areas can generate sufficient power supplies, which can then be distributed to homes, businesses, institutions, and other locations where conventional electricity supply is inadequate. Despite these advantages, solar cells have a few drawbacks. The amount of sunlight available largely depends on geographical location and weather conditions. Additionally, the initial setup and equipment costs are also important factors to consider. [29, 30, 31, 32].

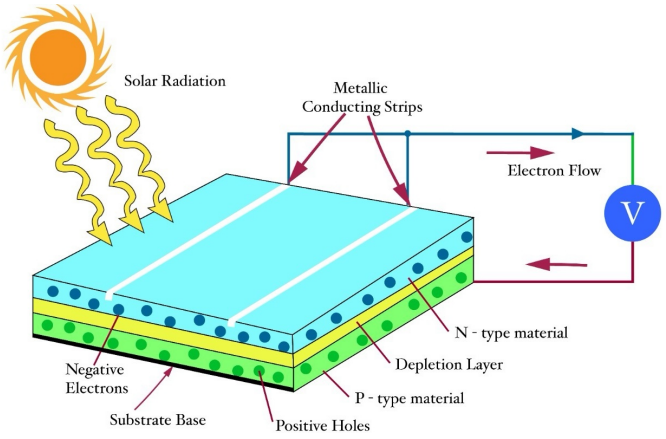

Figure 1.1: Schematic of photovoltaic cell with layers of n-type and p- type material [33].

1.2 Principles of solar cell operation

The operational principle of solar cells or photovoltaic cells is grounded on photovoltaic effects. The radiation of solar cells quickly converts into electrical energy in this phenomenon. It is basically a p-n junction device. Figure 1.1 illustrates how sun rays are transformed into electricity through electrons and hole movement in the cell structure [33, 34]. The configuration of photovoltaic solar cells involves two semiconductor regions with different electron concentrations, which can be either n-type or p-type. N-type semiconductor materials have excess negatively charged electrons, while p-type materials have positively charged carriers known as holes. Both n-type and p-type materials are electrically neutral, although they differ in their charge carriers. [35].

The photovoltaic effect primarily involves three essential processes, which are discussed below:

Absorption of Photon: In this step when photons (light particles) strike the surface of a semiconductor material, such as silicon. The semiconductor absorbs the energy from photons, which causes electron excitation. These excited electrons break

their atomic bonds. Electron-hole pair generation in a p-n junction semiconductor happens because of photon absorption. If a photon with energy E=hν (where h is Planck's constant and ν is the frequency of the light) has energy above the semiconductor's bandgap energy Eg, it can excite an electron to the conduction band from a lower energy level which is known as the valence band. This generates a positive charge hole in the valence band [36, 37, 38]. A minimum energy is needed to create an electron-hole pair, and it can exceed the energy of the absorbed photon, this energy can be represented by $h\nu_0$. This excess energy $(h\nu - h\nu_0)$ provides additional kinetic energy to the excited electron or hole. However, the remaining energy does not stay in the system. In semiconductor, it dissipated as heat [36, 38].

Electron–hole generation: When photons are absorbed, they generate charge carrier pairs known as free electrons and holes. In this process, holes move across the p-region, while electrons flow through the n-region and the external solar circuit. Eventually, electrons and holes recombine after traveling through the circuit.

Separation of charge: In this step, the electric field of the PV cell separates the electrons and holes. Electrons flow toward the negative side which is an n-type layer, whereas holes move toward the p-type layer or the positive side. A voltage is created across the PV cell by this charge separation process. The layer of the n-type should be thinner compared to the p-layer. therefore, electrons can flow rapidly throughout the circuit. Furthermore, it helps to electric current generation before hole recombination process. Also, the n-layer needs to be coated by using an anti-reflection coating. This provides the advantage of reducing the reflection on the surface and additionally aids in improving the semiconductor light absorption; thus, results of efficiency increase [28, 35].

1.2.1 The P-N Junction

The combination of the p-type region with the n-type region creates a P-N junction. fundamental structure of a semiconductor diode is formed in this process. majority of charge carriers are free electrons in the n-type region and there are few thermally generated holes. On the other hand, holes are the predominant carriers, with a small number of thermally generated free electrons works as minority carriers.

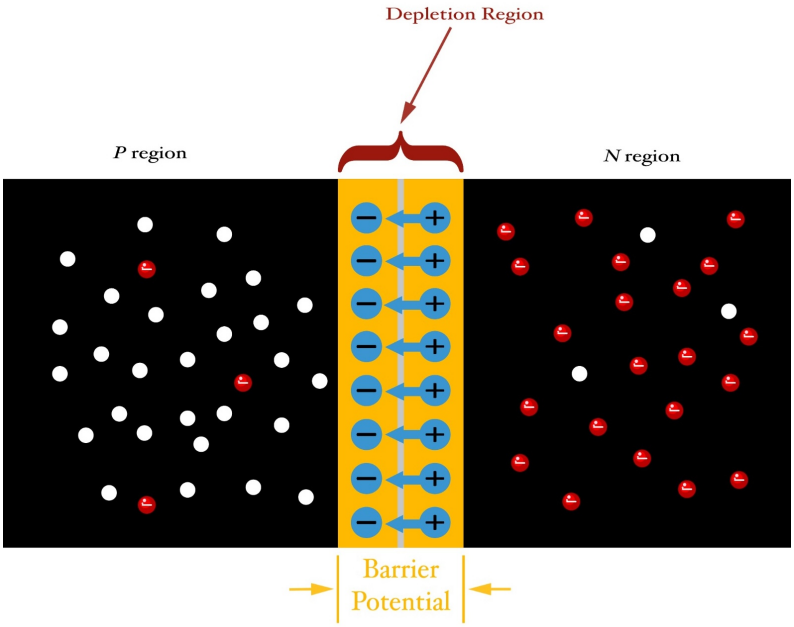

Figure 1.2: The basic structure of the semiconductor P-N junction [39].

A photovoltaic cell is a semiconductor diode designed to convert sunlight into electrical energy. It is made of a single silicon crystal, where one side is doped with pentavalent impurities to create a n-type layer, while another region is doped with trivalent impurities to form a p-type layer. An additional charge carrier to both sides has been introduce by this doping process. Electrons from the n-side diffuse into the p-side when these n-type and p-type regions come into contact and leave behind positively charged atoms near the junction. Correspondingly, holes move into the n-

type from the p-type region, creating negatively charged atoms. Since electrons and holes transfer, diffusion current (I_{diff}) is produced, which forms a charge-free zone called the depletion region or space charge region. Any further flow of electrons or holes is prevented by the electric field forms in this area [39].

In a semiconductor, under an equilibrium state, two types of currents are generated. These currents are produced by electrons and holes flow in semiconductors. One is known as drift current which is caused by the junction electric field, and the other one is diffusion current (I_{diff}), which results from the difference in concentration. Electrons diffusion current can be expressed as I_{n-diff}. The equation can be written as:

$$I_{n-diff} = eD_n \frac{dn}{dx} \tag{1.1}$$

Again, diffusion current density of holes:

$$I_{p-diff} = -eD_p \frac{dp}{dx} \tag{1.2}$$

The ratios representing the change in particle density relative to the change in diffusion distance for electrons and holes are given by $\frac{dn}{dx}$ for electrons and $\frac{dp}{dx}$ for holes. I_{drift} is developed from the electric field. The diffusion current is reversed to the drift current. Drift current $(I_{n-drift})$ is generated from drift electrons. The expression is given below:

$$I_{n-diff} = en\mu_n E = env_{dn} \tag{1.3}$$

Where, μ_n is the mobility of electrons, E is the electric field in the depletion region, and it denotes the drift velocity of electrons. Similarly, the drift current $I_{p-drift}$ due to the movement of holes is expressed as follows:

$$I_{p-diff} = ep\mu_n E = epv_{dp} \tag{1.4}$$

Hole mobility is denoted as $_p$ and average drift velocity of holes is, v_{dp}. Net

$$I_{drift} = e(\mu_n n + \mu_p P)E \tag{1.5}$$

And

$$\rho = e(\mu_n n + \mu_p p) \tag{1.6}$$

So, I_{drift} can be written,

$$I_{drift} = e(\mu_n n + \mu_p P)E = \rho E \tag{1.7}$$

Where the conductivity of the electronic semiconductor is ρ [38].

In the depletion region of non-degenerate semiconductors, the electric field within this region drives out free electrons and holes, thereby preventing net currents. This helps to balance the I_{drift} and I_{diff} in the equilibrium states. The balance among diffusion and drift current in a non-degenerate semiconductor leads to the **Einstein relation**, which connects the diffusion coefficient D and the mobility μ of charge carriers [38]. The Einstein relation is,

$$\frac{D}{\mu} = \frac{KT}{e} \tag{1.8}$$

Where "k" is Boltzmann's constant, "T" is the absolute temperature in kelvins, and "e" is the electron charge.

The mechanism of a P-N Junction Solar Cell in applied voltage is like a conventional P-N junction diode. The depletion region shrinks while connecting the diode to a forward-biased external voltage. The positive and negative charge carriers (holes and electrons) are repelled in the direction of the p-n junction from both negative and positive terminals. As a result, less energy is required for the charge carriers to flow across the depletion region. Electrons begin to move across the space charge area, as the voltage applied reaches the barrier potential. In forward bias mode, the diode current is described by the ideal Shockley equation. When the external forward voltage rises, the current rises exponentially [40].

$$I_d = I_0(exp(\frac{eV}{KT}) - 1) \tag{1.9}$$

where the diode current is I_d, while free carriers flow across the junction; saturation diode current in the depletion region can be defined as I_0' while temperature of room T is 300 K. External voltage is V, Boltzmann's constant, K= $1.3805x10^{-23}$ J/K,

and e is the electron charge, $1.60217657x10^{-19}$ coulombs [41, 42]. The photovoltaic effect occurs by exposing the PV cells to the sunlight, which is the basic principle behind transforming solar energy into electrical energy or solar power generation. In a semiconductor, the formation of a p-n junction occurs while incident light is absorbed by the surface. pairs of positive and negative charges create. Through the negative terminal, electrons move to the metal contacts from the n-region then it flow through the load. consequently, electrons again return to the positive contact and then go through the p-region. electrons can recombine with holes again in the p area.

1.3 Types of photovoltaic or solar cell

Solar cells are categorized based on the types of semiconductor materials used. The efficiency of PV cells varies depending on the materials used in their design, as each material has a specific capacity to absorb sunlight. Solar cells can feature either a single junction or multiple junctions. The three main types of PV cells are classified as first, second, and third-generation cells. First-generation solar cells are made from crystalline silicon, including monocrystalline and polycrystalline types. Monocrystalline solar cells are in high demand, accounting for about 80% of the global commercial market. [43].

Second-generation solar cell technology, also known as thin-film solar cell technology, reduces fabrication costs. Unlike traditional silicon crystal technology, which requires pure crystalline silicon—a complex and costly process—thin-film technology uses significantly less deposited silicon than the conventional wafer-based approach. [44].

Third-generation solar cells encompass a variety of thin-film technologies, most of which are still in the research or development stages, making commercial implementation currently unfeasible. Many approaches involve organic materials, such as organometallic compounds, in addition to inorganic components. However, these methods have traditionally shown low efficiency and limited stability in absorber materials, rendering them unsuitable for commercial applications. Therefore, extensive research is ongoing to explore their potential for delivering cost-effective, high-

efficiency solar cells. [45]. In the section below, some important types of solar cells are discussed.

1.3.1 Amorphous Silicon Solar Cell

Non-crystalline form of silicon is known as Amorphous silicon. This considered as most advanced thin-film technology, with more than one decay of commercial availability. It is usually used in devices like pocket calculators and also, applied in power systems of residential areas, commercial buildings, and remote installations. United Solar Systems Corporation has been a leader in the development of amorphous silicon solar cells and continues to be a major manufacturer in the market. By the vapor-deposition method, A-Si panels form a thin silicon layer, approximately a thickness of 1 micrometer, onto a glass or metal substrate. Also, moderately low temperatures, as low as 75°C are required for depositing. This property helps to deposit plastic materials. The formation of the cell structure involves a p-i-n single sequence layer. On the other hand, when single-layer cells are exposed to sunlight, their power output significantly decreases (by 15–35%). This loss of efficiency is due to a phenomenon known as the Staebler-Wronski Effect [29].

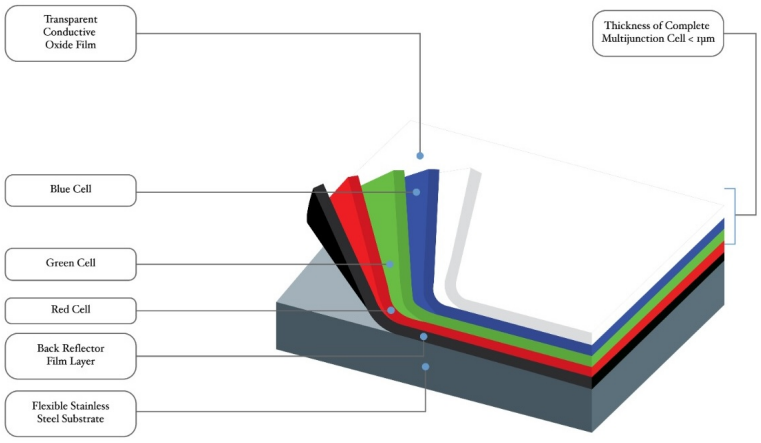

Figure 1.3: The schematic representation of triple layer amorphous silicon from Unisolar [29].

Total thickness triple junction solar cell is just 1 micron, or approximately 1/300th of mono-crystalline silicon solar cell the size. Cost-effectiveness and lower manufacturing expenses is the key advantage of A-Si.

1.3.2 Biohybrid Solar Cell

Solar cells, designed with a combination of organic materials, particularly photosystem I, and inorganic components are recognized as Biohybrid solar cell. By using photosystem I, a photoactive protein complex, found in the thylakoid membrane, scientists at Vanderbilt University have developed biohybrid solar cells that reproduce photosynthesis naturally and improve solar energy conversion efficiency. In the renewable energy industry, this invention demonstrates a promising progression.[46].

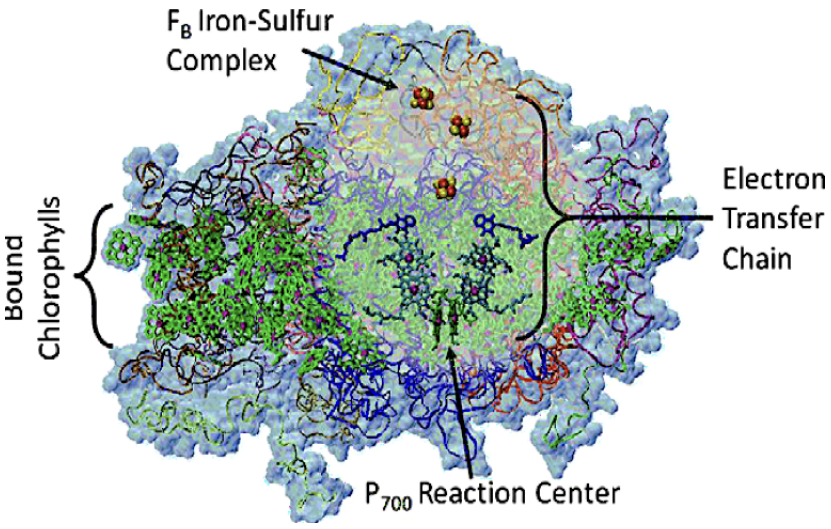

Figure 1.4: Multilayered Bio-Hybrid Solar cells [47]

Photonic energy is absorbed by the multiple layers of photosystem I, where it is converted into chemical energy, allowing the generated current to flow through the cell. The cell is constructed from many of the same inorganic materials used in conventional solar cells, with the addition of photosystem I complexes. These complexes are gradually introduced and assembled within a gold layer over several days,

eventually forming a thin green film. This film plays a crucial role in enhancing the cell's energy conversion efficiency. Nevertheless, further research is still required to advance these types of cells. [46, 47, 48].

1.3.3 Features of a laser-grooved Buried Contact Solar Cells

In buried contact solar cells, plated metal contacts are used to form laser-formed grooves. This is known as a commercially highly efficient technology. A key feature enhancing the high efficiency of buried contact solar cells is the embedding of metal contacts within laser-formed grooves in the silicon cell. Several drawbacks in screen-printed contacts can be mitigated with this design, resulting in an improvement of solar cell performance by up to 25 percent compared to traditional screen-printed solar cells. A cross-section of laser-grooved buried contact PV cells is demonstrated in Figure 1.5 below [29, 49].

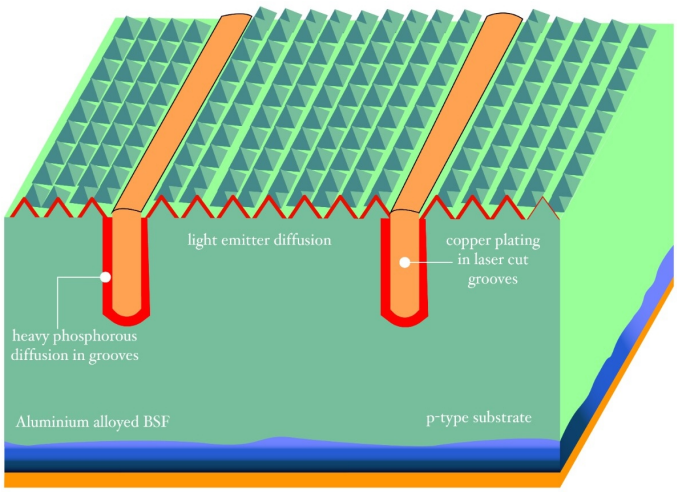

Figure 1.5: Schematic of the buried contact solar cell

The buried contact configuration features a large metal height-to-width ratio, this facilitates a significant amount of metal to be used in the contact fingers without requiring wide metal strips on the surface. This design allows the arrangement of

several closely spaced fingers, maintaining a high level of transparency. In larger solar cells, traditional screen-printed models can experience shading losses of approximately 10 to 15%. Whereas the buried contact technique reduces those losses to just 2 to 3%. This reduction in shading leads to less reflection and higher short-circuit currents, which eventually improves efficiency. In buried contact solar cells, the metallization design leads to enhanced performance of the emitter. In screen-printed cells, the emitter area is highly doped to diminish the loss of resistivity. On the surface of the cell, it allows to form a "dead" layer. As emitter losses are insignificant in a buried contact cell, the doping of the emitter can be modified to achieve higher open-circuit voltages and short-circuit currents. In concentrators, this solar cell structure plays a significant role [49, 50].

1.3.4 Cadmium Telluride Photovoltaic Cell (CdTe)

CdTe photovoltaics is a method that uses cadmium telluride, a thin semiconductor layer, to convert sunlight into electricity [51]. In contrast to other conventional crystalline silicon solar cells, Cadmium telluride is the least expensive thin film technology. The duration of energy payback for CdTe is below one year, facilitating rapid carbon reductions without creating an immediate energy lack. However, environmental concerns arise because of the toxicity of cadmium. these issues are eased through the reutilizing of CdTe modules once they reach the end of their lifecycle [52, 53, 54].

Near future, employing rare materials is a constraining factor for the industrial scalability of CdTe technology. The scarcity of tellurium, which is the anionic form of telluride, is similar to platinum in the Earth's crust, significantly impacting the overall cost of the modules. CdTe photovoltaics are already employed in some of the largest solar power plants in the world, including the Topaz Solar Farm. In 2013, CdTe technology represented 5.1% of global PV production and made up over half of the thin film market [54, 55]. Cadmium is an extremely toxic material, although cadmium telluride (CdTe) is considered less dangerous for short-term exposure. However, it can still be harmful if ingested, inhaled as dust, or conducted without proper safety measures. The harmfulness isn't just from cadmium itself but also from the reactivity of CdTe, which can cause cellular damage. Although there are concerns about

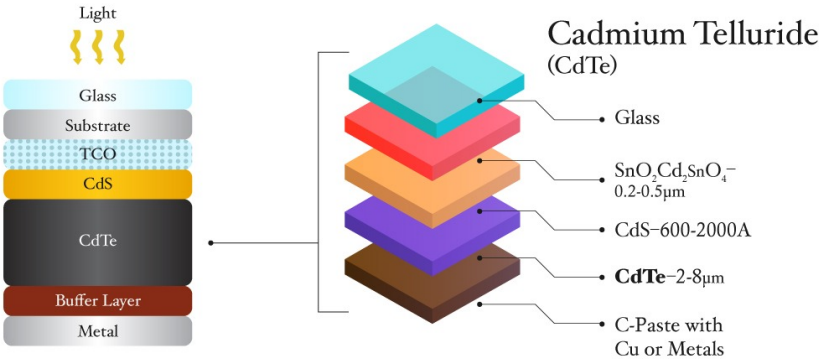

Figure 1.6: (a) configuration of substrate on CdTe PV cells. (b)graphical presentation of cadmium tellurium solar cells.

the disposal and long-term safety of CdTe in solar panels, research, including studies from the U.S. Department of Energy, shows minimal risk when recycled. While the European Union classified cadmium compounds as carcinogenic, using CdTe in solar panels is considered safe in current rooftop installations. It does not present any significant problems in the environment [56].

1.3.5 Copper Indium Gallium Selenide Solar Cells

A copper indium gallium selenide (CIGS) solar cell, also known as a CIGS or CIS cell, it is a type of thin-film PV cell that converts solar energy into electricity. By depositing a thin layer of copper, indium, gallium, and selenide onto a glass or plastic substrate CIGS are fabricated. With electrodes on both sides to accumulate the electric current. Due to its high absorption coefficient, CIGS efficiently absorbs sunlight, so a thinner film compared to other semiconductor materials is required. It is one of the main thin-film photovoltaic (PV) technologies, along with cadmium telluride and amorphous silicon. CIGS can be placed on flexible surfaces since they are very thin and flexible [29, 55].

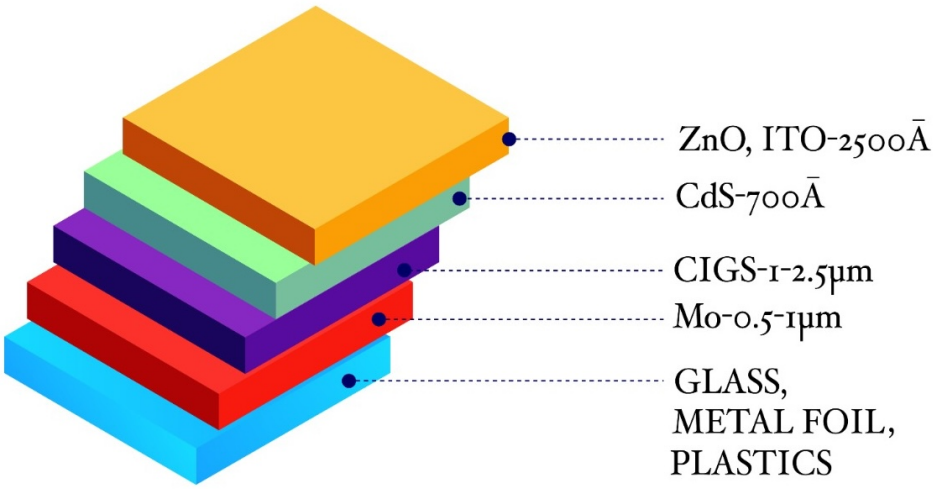

Figure 1.7: Schematic demonstration of Copper Indium Gallium Selenide Solar Cells.

Despite the use of high-temperature deposition techniques for optimal performance, normally on glass substrates, recent advancements in low-temperature deposition methods have significantly minimized the change in performance with modern polysilicon panels. CIGS is widely accepted due to its flexible application, less less-weight solar panels, also efficiency enhancement has proven CIGS as a consistent alternative in the solar cell industry [55].

1.3.6 Gallium Arsenide Germanium Solar Cell

Gallium arsenide (GaAs) consists of gallium and arsenic. These two elements together form a compound with numerous significant properties. As a semiconductor, compared to silicon wafers GaAs have higher mobility of electrons and a faster saturated electron velocity. Semiconductors are materials with electrical conductivity that lie between insulators and conductors, and their conductivity can change based on the temperature. This property is beneficial for numerous purposes. One unique feature of gallium arsenide is its direct band gap, which allows it to produce light efficiently. GaAs have a zinc blend crystal structure and belong to the III-V semicon-

ductor. It's widely used in producing devices such as microwave integrated circuits, infrared LEDs, laser diodes, solar cells, and optical windows.

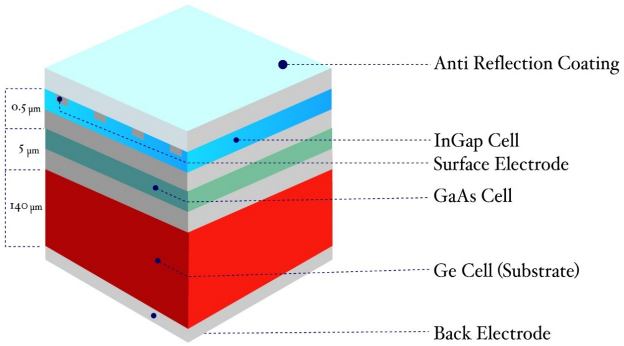

Figure 1.8: InGaP/GaAs/Ge solar cell diagram

There is also a larger breakdown voltage in gallium arsenide. Breakdown voltage refers to the minimum reverse voltage needed to make a component conductive, allowing current to flow in a reverse direction. Because of its unique properties, gallium arsenide (GaAs) is appropriate for a variety of electrical applications, from everyday devices to high-tech systems. For instance, mobile phones, satellite communications, micro and nano-sized semiconductors, and radar systems, can be utilized in nanotechnology-based solar power [57, 58].

1.3.7 Hybrid solar cells

The beneficial effects of organic and inorganic semiconductors are merged in hybrid solar cells. organic materials made of conjugated polymers function as light-absorbing donors and transport holes in hybrid photovoltaics [59]. In contrast, the function of inorganic materials is they work as acceptors and electron transporters inside the solar cell structure. These types of PV devices offer the potential for less expensive production through roll-to-roll processing, as well as scalable solar power transformation [60]. In hybrid solar cells, an organic material is merged with a high electron transport material to form the photoactive layer. This combination is

arranged in a heterojunction structure, that delivers better efficiency of power conversion than using just one single type of material [61].

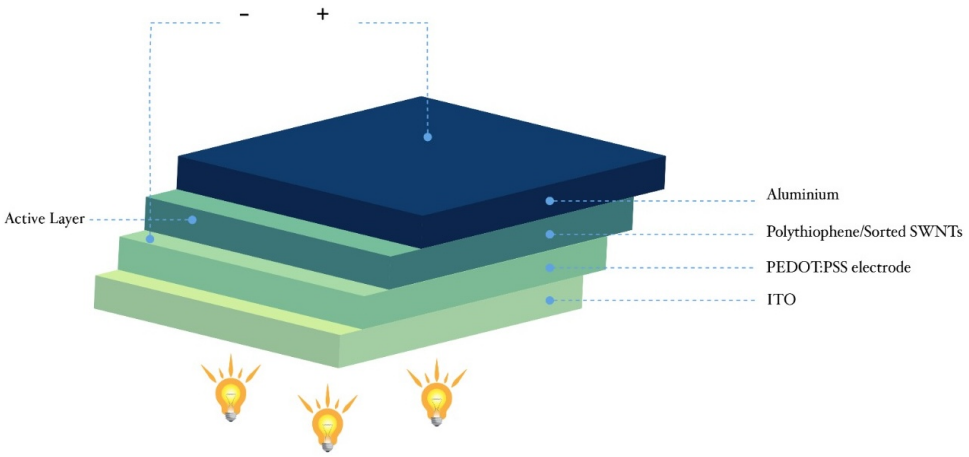

Figure 1.9: Carbon nanotube Photovoltaic cell structure [62].

One material acts as the photon absorber and provides excitons, while the other assists in dissociating excitons at the junction. After an exciton is generated in the donor and delocalized on a donor-acceptor complex, the charge is then transported and separated [63].

1.3.8 Multi-crystalline or Poly-crystalline Solar Cell

Polycrystalline silicon, signified as polysilicon or poly-Si, which is an extremely pure silicon with a crystalline structure, in the PV and electronics industries it is mainly utilized as a raw material. It is produced through a chemical purification method, the Siemens process, which includes distilling volatile silicon compounds and decomposing them into silicon through intense heat. An additional novel refinement procedure employs a fluidized bed reactor (FBR). Mainly, FBR is a reactor that is designed to perform several chemical reactions involving multiple phases. Upgraded metallurgical-grade silicon (UMG-Si) through metallurgical is also manufactured in PV industries. metallurgical is used rather than chemical purification. Polysilicon fab-

ricated for the electronics industry has impurity levels of less than one part per billion (ppb), whereas, solar-grade polycrystalline silicon (SoGSi) is usually less pure. In 2013, major producers of the global supply of around 230,000 tons included companies like GCL-Poly, Wacker Chemie, OCI, Hemlock Semiconductor, and REC, headquartered in Norway [64, 65].

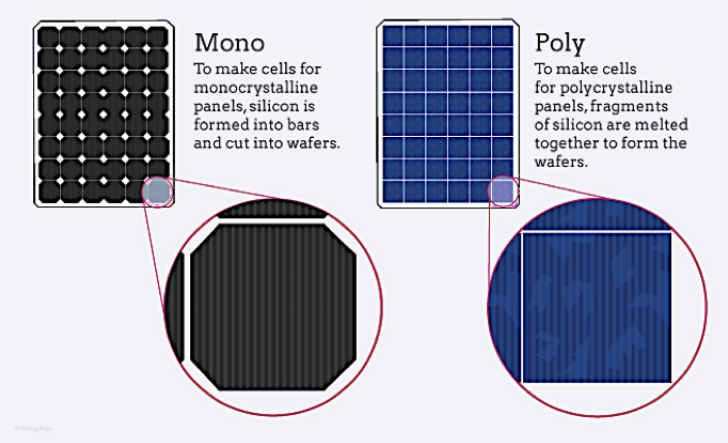

Figure 1.10: Different types solar panel (Mono and Polycrystalline) [65].

Typically, big rods segmented into precisely sized chunks and packed in clean rooms for distribution, polysilicon feedstock is either cast straight into multi-crystalline ingots or undergoes a recrystallization process to generate single crystal boules. The products are later cut into fine thin silicon wafers, which work as necessary components in the manufacturing of PV cells, ICs, and various semiconductor devices. Polysilicon consists of crystallites. It is basically a small crystalline structure, that assists in imparting a characteristic metallic flake appearance. Although the terms polysilicon and multi-silicon are normally similar, multi-crystalline typically signifies crystals that exceed 1 mm in size. Multi-crystalline PV cells are the predominant category in the rapidly developing photovoltaic (PV) industries and consume the majority of polysilicon produced globally. The production of conventional solar modules requires approximately 5 tons of polysilicon to generate 1 megawatt (MW) of energy [66].

1.3.9 Thin Film Solar Cell (TFSC)

A thin-film solar cell (TFSC) is classified as a second-generation Photovoltaic technology. TFSC is fabricated by a thin layer of semiconducting material (CGIS, CdTe, and a-Si) onto substrates such as glass, plastic, or metal. Thin-film solar cells are employed in various forms, including cadmium telluride (CdTe), copper indium gallium selenide (CIGS), and other groups of thin-film silicon for instance, (a-Si, TF-Si). The range of diverse materials selection, lightweight, and design flexibility allows this to be utilized in numerous applications. These cells can be integrated into conventional rooftop solar panels and more innovative uses such as solar windows, building facades, and portable solar chargers. This flexibility makes thin-film technology especially attractive in urban locations. These solar panels can be essential in areas with limited space.

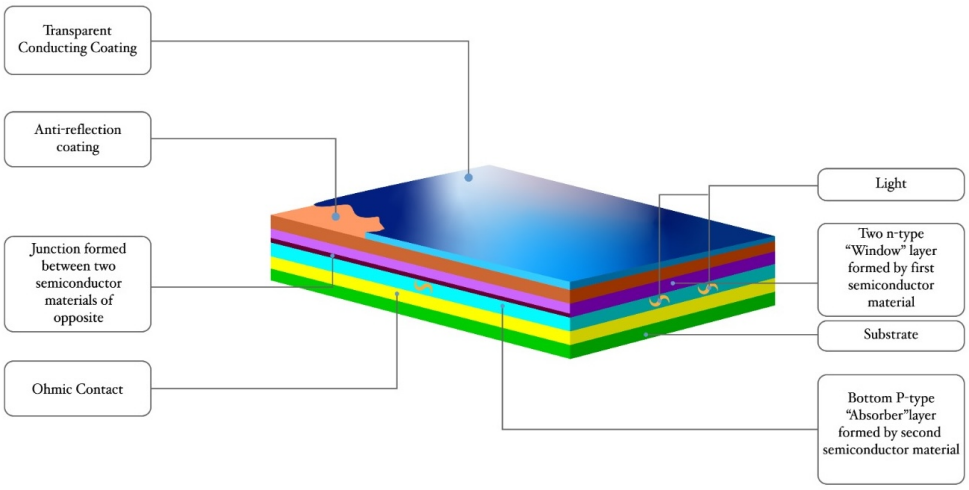

Figure 1.11: Design of thin film solar cell structure.

Thin film solar cell's width or thickness ranges are approximately a few nanometers (nm) to several tens of micrometers (μm), making them significantly thinner than first-generation crystalline silicon solar cells (c-Si), which utilize silicon wafers as thick as 200 micrometers. It shows greater flexibility because of its thin structure,

also reduces its weight, and minimizes drag. Thin-film solar cells are often used in building-integrated photovoltaics and as semi-transparent glazing that can be laminated onto windows. Additionally, rigid thin-film solar panels, sealed between two layers of glass, are utilized in some of the world's largest photovoltaic power plants. [67, 68].

Chapter 2

Laser Scribing

2.1 Basics of Laser scribing process

The development of energy solutions that lessen the ecological impact in comparison to existing fossil fuel-based systems is crucial, to the environmental issues associated with greenhouse gas production [69, 70]. Solar cell technology represents a significant sector within renewable energy, serving a critical function for electricity generation. This importance is amplified by the escalating global energy demand, which is propelled by the instantaneous growth in population [71]. The field of PV cell technology has experienced substantial advancements over recent decades. Crystalline solar cells, which have been in use for a long period, can accomplish standard efficiency requirements. Laboratory analyses have demonstrated efficiencies of 26.8% for monocrystalline silicon solar cells and 23.3% for polycrystalline silicon solar cells [72]. The excessive expense of manufacturing has led to improvements in thin film technology aimed at reducing material consumption [73]. The main types of solar thin films that have significantly influenced the market include amorphous silicon, cadmium telluride (CdTe), and copper indium gallium selenide (CIGS) [74, 75]. Recent progress in new generations of solar thin films, employing numerous materials, has focused on overcoming challenges such as cutting production costs, supporting large-scale manufacturing, improving durability, addressing environmental impacts,

and boosting efficiency.

In solar technology that uses thin films, there are three specific stages of scribing required to reduce the amount of photocurrent and resistance losses. These approaches are tried-and-true methods to reduce ohmic losses [76, 77]. In addition, the application of a serial connectivity architecture lowers losses while simultaneously limiting the output current of the solar cell, which raises the output voltage [78]. To obtain the efficiency and performance achieved in a laboratory setup for cells smaller than 1 cm^2, a high active surface area of approximately 95% of the total sub-module area is needed to enhance the efficiency of solar cells [79]. Laser scribing is an invaluable process in the fabrication of thin-film solar cells, this method is mostly composed of multiple layers of materials applied onto a substrate. Nevertheless, the laser scribing process can yield distinct output results which are controlled by variations in material characteristics, the thickness of the film, and the architecture of the PV cells. This variability highlights the necessity for tailored laser scribing systems and conditions. To achieve optimal efficiency, acquiring a comprehensive understanding of the effects of different materials is crucial. besides observing how solar cell materials respond to the laser scribing process. Despite these challenges, laser scribing holds significant potential for improving the commercialization of next-generation solar cells, for instance, perovskite, which demands further study due to its intricate structure [72].

2.2 Laser Scribing Processes of Solar Cell Fabrication

The manufacturing process of thin film solar cells encompasses numerous phases, including various film deposition methods and three distinct scribing operations, referred to as P1, P2, and P3. These operations are crucial for describing individual cells and establishing electrical interconnections between adjacent cells in series, so lessening current and ohmic losses while enhancing voltage [72]. As represented in Figure 2.1 below, the P1 stage requires a thorough incision through the back conductive layer on the substrate, facilitating a dynamic electrical isolation step that enables obligatory cell separation [80]. The P2 scribing process involves the removal of the

absorber layer from the back contact layer, for establishing electrical connectivity between the back and front conductive layers. This is another essential step. thus, this step enables current flow between neighboring submodules [81, 82]. This scribing is typically accomplished following the deposition of the absorber layer onto the back contact layer [82]. The final step is P3 scribing, which is intended to create a line on the front contact layer to complete the isolation process, similar to the P1 scribing step. In some cases, both the front contact layer and the absorber layer may be selectively removed to ensure full isolation of this layer. [78].

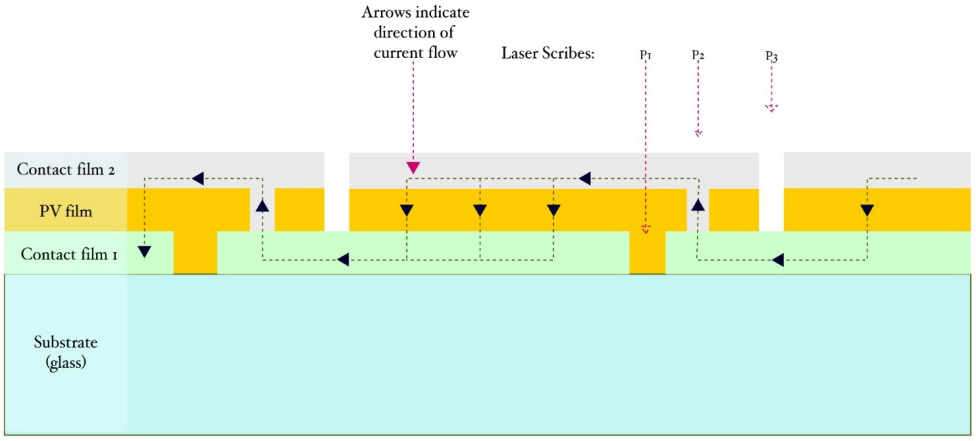

Figure 2.1: Schematic of three different scribing steps of a solar cell also the performance of cells.

In figure 2.1 represents a layout of laser scribing processes (P1, P2, and P3), that illustrate the definition of individual cells and the creation of a monolithic serial interconnection. [72].

Dead Area is the space between the P1 and P3 scribes, which does not contribute to electricity generation. To improve the active region, it is necessary to lower the size of the dead zone by reducing the space among the P3 scribe and the following P1. As a result, the positioning and thickness of each scribe pattern are significant aspects in optimizing the performance of PV cells and the effective utilization of the solar cell region. Furthermore, the scribing procedure must present a high precision

level that should be carefully controlled, to enable the selective removal of the chosen thin film while maintaining the integrity of the underlying layers. The scribes must remain clean and undamaged, especially for P2, since the top and bottom contacts are connected by P2. The thickest layer is the absorber layer. Partial removal causes an increase in electrical resistance between cells and decreases the efficiency. The P2 step of the scribing process is the most challenging one among all of them. Since it is hard to achieve an undamaged clean scribe. Higher speeds of laser scribing are necessary for efficiency enhancements [83].

2.3 Types of Scribing technique

2.3.1 Mechanical Scribing

Mechanical scribing represents a traditional method for creating monolithic serial interconnections. This method utilizes a needle to remove material from the underlying deposited layer, thereby forming a channel that measures several hundred microns in width and approximately 500 microns in depth [84]. The pressure exerted by the needle creates the necessary tension to detach the material, eventually resulting in delamination and the formation of chips [85]. This method is primarily designed for P2 and P3 scribing due to the high susceptibility of the underlying material, which necessitates intense precision. Despite its ability to achieve significant efficiencies, there is drawbacks [86, 87]. The mechanical scribing technique goes through many wears and tear, necessitating the implementation of a method for needle replacement. Additionally, issues such as uncontrolled breakout and inaccuracies may occur, influenced by the material's ductility and adhesion properties [88]. In the case of ductile materials, there is a tendency for material to accumulate on either side of the scribed grooves. As a result, adjacent scribes must be positioned further away from the uneven grooves to prevent overlap, [85] which sequentially increases the distance of the dead area. While mechanical scribing remains a conventional technique that offers remarkable quality, the growing demand for enhanced efficiency, precision in scribing, and accelerated processing speeds have prompted thin-film photovoltaic mechanisms to explore more advanced and precise alternatives.

2.3.2 Laser Scribing

While using mechanical scribing methods researchers faced numerous challenges. therefore, as an alternative technique laser scribing method showed tremendous results. The difference between the two scribing techniques, mechanical and laser scribes is demonstrated in Figure 2.2 below [85]. It is observed that the conventional scribing technique (mechanical) creates an uneven scribe, this characteristic of getting an uneven pattern is mostly associated with debris and material breakout from the intended path. However, laser scribing presents more precise, sharp, and smoother lines or patterns. This results, in significantly reducing the effects of generated debris.

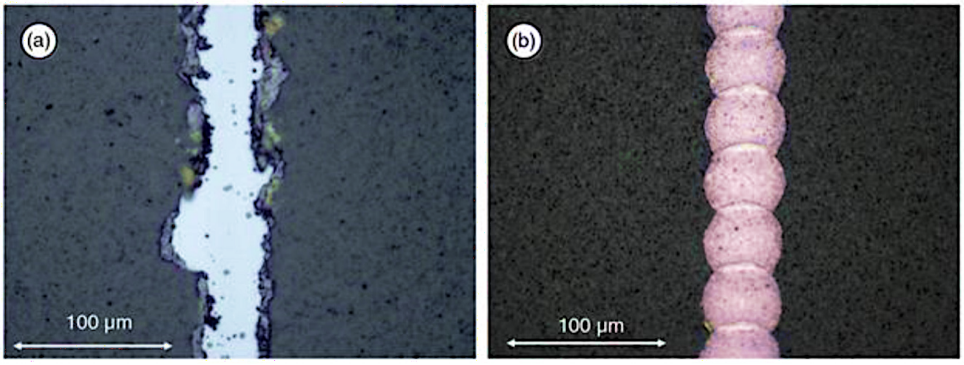

Figure 2.2: Evaluation of the scribes accomplished by both scribing techniques, (a) the left figure demonstrates mechanical scribing and (b) the right one shows laser scribing

By laser scribing method fine scribing lines with straight edges can be achieved. this technique keeps the process clear and clean. To achieve these properties, scribing must be devoid of thermo-mechanical and damage due to chemicals. The melting of the central absorber layer, which contains metallic elements, is the significant reason that causes the development of shunt resistance between the front and back contact layers. Numerous analyses have been performed by researchers from all over the world. Common challenges that affect the surface integrity of the scribes involve the development of mini-cracks, the heat-affected zone (HAZ), diffusion, and the

formation of debris. Since Laser scribing is a thermo-mechanical process, an in-depth understanding of the mechanisms of melting, evaporation, and plasma formation is essential for scientists aiming to enhance the output efficiency of the laser scribing procedure [72].

2.4 P1-P2-P3 laser scribing steps in thin-film solar cells

In the development process of thin-film PV cells, the P1, P2, and P3 laser scribing process plays a crucial role since applying this step helps to define individual cells and form the electrical connections between them. Each step (P1, P2, P3) of scribing emphasizes an individual layer of the material of the solar cell. Individual steps ensure proper electrical isolation and connection among solar cells. In Figure 2.3 process chain of thin film solar cells is explained.

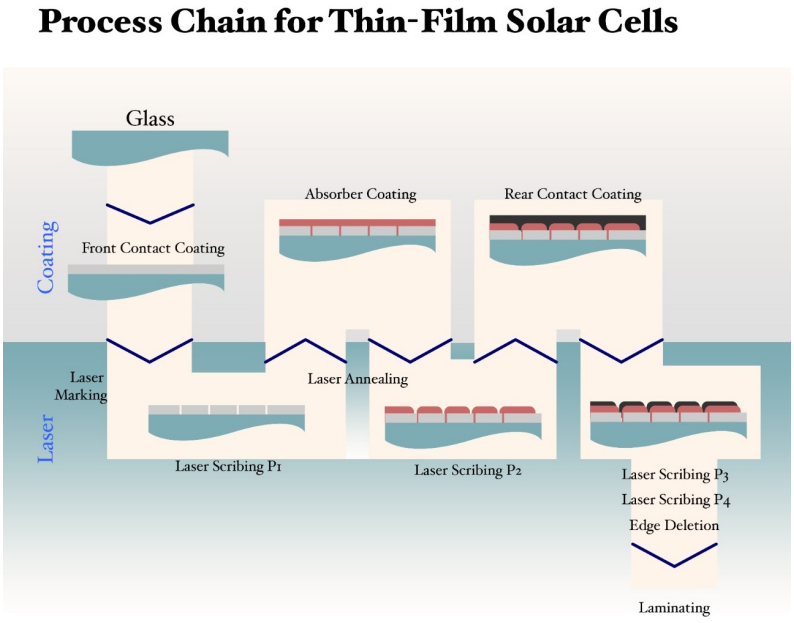

Figure 2.3: Thin-film laser solar cells process [89]

2.4.1 P1 Scribing (Back Electrode Scribing)

In P1 scribing targets the back conductive layer of a solar cell, commonly made of metals. usually molybdenum (Mo) in CIGS cells or aluminum (Al) in other types. The principal objective is to isolate individual cells by cutting through this back electrode. This separation helps prevent short circuits between adjacent cells. Materials: The back conductive layer. typically, molybdenum, and aluminum). The procedure of scribing: An infrared (IR) laser, characteristically with a wavelength of 1064 nm, is used to eliminate the back electrode, cutting down to the substrate (glass or plastic). This ensures that each cell within the solar module is electrically isolated. So as a result, proper electrical isolation between the cells can achieved by this step [90, 91, 92].

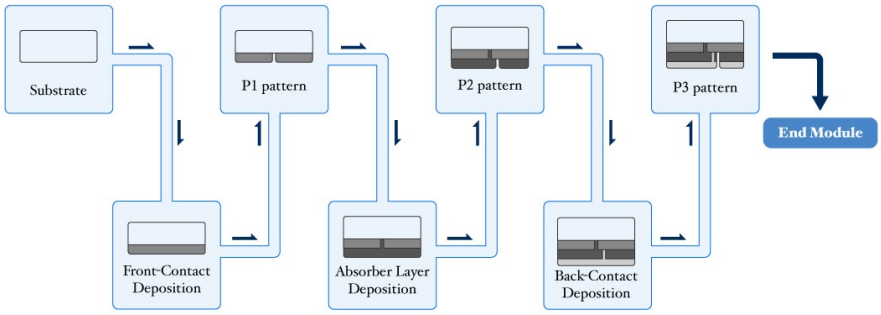

Figure 2.4: Flow chart of thin film solar cell module fabrication process with laser scribing [93].

2.4.2 P2 Scribing (Absorber Layer Scribing)

The absorber layer is the principal focus of the P2 scribing process. This absorber layer is the main photovoltaic layer that converts sunlight into electricity. In the P2 process, the back electrode is exposed and fabricates electrical contact between the back and front conductive layers. the current flow between adjoining cells can be ensured by this step. Material: Absorber layer (such as CIGS, CdTe, or a-Si). Procedure: A green laser (532 nm) or infrared laser is used to remove a thin line of the absorber layer, exposing the underlying back electrode (that is isolated by the P1 step). This allows for electrical contact between the front and back layers of the adjacent cells. Result: Electrical contact between the front and back electrodes is achieved, allowing current flow between cells [92].

2.4.3 P3 Scribing (Front Electrode Scribing)

The P3 scribe includes the front conductive layer, a transparent conductive oxide (TCO) for instance indium tin oxide (ITO) or aluminum-doped zinc oxide (AZO) is referred to as front conductive layers. This step separates the cells by removing a thin strip of the front conductive layer, completing the cell isolation. The material of the Front conductive layer is (ITO, AZO). Procedure: A UV laser (355 nm) or green laser is applied to create a precise cut in the front conductive layer. In specific circumstances, both the front contact and absorber layers are removed to ensure complete separation. The P3 scribe finishes the electrical isolation of the individual solar cells and allows for their series interconnection. Complete isolation of adjacent cells is achieved while maintaining series connections, increasing the voltage output of the module [91, 92].

2.5 Laser Scribing Apparatus of University Parma

(a) Innolight Helios IR (b) Galvanometric head

Figure 2.5: Source used

		EOLITE BOREAS	INNOLIGHT HELIOS	DATALOGIC MW-DY*/MW-M	DATALOGIC AREX
Lunghezza d'onda	nm	1030/512	1064	1064	1064
Average power	W	40(IR) 15(verde)	5	20	20
Pulse Duration		<15ns*	500*-800*ps	10-200	100
Repetition rate	KHz	20-75	30-70	MW-DY:Single shot - 100 MW-M:Single shot - 500	20-100
Pulse energy	mJ	1	0.1	>0.6	1
Max peak power	kW			12	10
Beam quality M^2		<1.3		<1.3	<1.3
Beam diameter	mm	2	2.5-5.5mm	6	6
Beam divergence (half angle)	mrad	0.4			
		* up to 35 KHz	*@30KHz **@70KHx	* Burst da 2x,3x,5x,7x impulsi da 10-30ns	

Table 2.1: Apparatus for Laser scribing(UNIPR) Available sources and characteristics.

2.6 Optical setup of Laser Scribing

A laser source that has a 1064 nm wavelength (Innolight Helios IR) and 530 ps pulse duration is utilized for our experimental setup for the scribing process. In reducing the effect of local melting at the edge of the scribing infrared radiation plays a crucial role. The optical setup consists of a laser source that combines with a rotary wave plate. With this configured setup, both the output power, as well as the beam expander are controlled. The polarization of the laser light can be adjusted by the wave plate. This plays an important role in achieving proper scribing on the sample. The modulation of laser power by changing the polarization state of the laser beam is controlled by the wave plate. Figure 2.6 demonstrates the typical optical setup that was configured according to our requirements for the scribing technique during experiments in the laboratory.

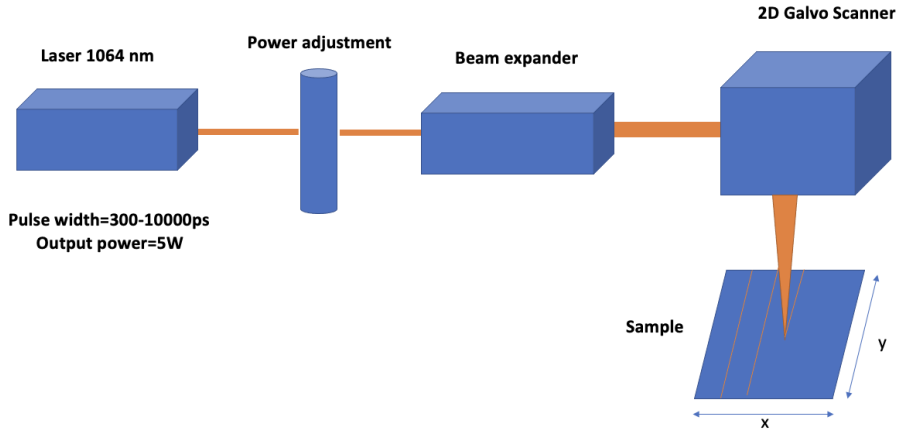

Figure 2.6: Optical setup arrangements for the laser scribing process for the laboratory in University of Parma.

In this experimental setup, a scanner is used, where the focal length of the lens is 540mm, and a beam that is close to the Gaussian intensity distribution is centered on the surface of our desired samples. The scribing process is managed by adjusting the scribing speed. typically, the speed is ranged from approximately a few mm/s

to m/s for the test. By employing a Field-Emission Scanning Electron Microscope (FESEM-FIB, Zeiss Auriga Compact) assembled with an Energy Dispersive X-ray spectrometer (EDX, Oxford) optimized with a Co standard, respective effects such as the microscopical, morphological, and compositional effect of the laser scribing on the Photovoltaic cells is investigated [94].

Chapter 3

Results and Discussion of Laser Scribing

3.1 Laser scribing on solar cells from IMEM-CNR

Among the technologies used to produce thin-film solar cells, CIGS (Copper Indium Gallium Selenide) holds a prominent position due to its adaptability to flexible and lightweight substrates. This makes it a promising option for applications in building integration, the transport sector, and even the space sector. These cells can be produced over large surface areas, but to minimize current losses, it is crucial to divide the surface into smaller, interconnected cells. This is achieved through a scribing technique—either mechanical or laser—carried out in three steps: separating the back contact (P1), cutting the absorber layer (P2), and isolating the top contact (P3) between adjacent cells. This step is pivotal to the overall performance of solar cells and remains the focus of extensive research to achieve precise optimization. The literature features numerous studies investigating the use of different laser sources as alternatives to mechanical scribing, to minimize layer damage such as micro fusions, phase shifts, and aggregate formation, to enhance solar cell efficiency and performance. In this activity, the Innolight Helios IR laser was chosen, operating wavelength of λ = 1064 nm (with the alternative to replacement at 532 nm). At a frequency of 30 kHz,

it generates pulses with 300 ps width. This laser source is combined with an optical system that contains an attenuator for control of the output power, in addition to a beam expander is also used. It helps to collimate the beam onto a galvanometric head. This head of galvanometric, in turn, directs the beam onto the sample with an almost Gaussian distribution and a focal length of 540 mm.

3.1.1 Activity Description

In this line of activity (LA11, WP1) the laser scribing technique previously successfully tested in the LA10 of WP1 has been used on photovoltaic cells with different structures

- Standard CIGS solar cells on glass.
- Cells with alternative absorber, Sb2Se3 on glass.
- Innovative semi-transparent solar cells (CuInGaS) for tandems on silicon-based solar cells.

3.2 Standard CIGS solar cells on glass

The initial samples tested are standard CIGS cells (glass / Mo / CuInGaSe / CdS / ZnO / ZnO: Al) measurement is approximately one square inch built on a glass substrate and complete with TCO and evaporated contacts. The characterization procedure includes conducting electrical measurements with the solar simulator prior to laser scribing (LS), observing the laser scratches underneath the optical microscope, investigating these marks by using an electron microscope to evaluate the composition of specific areas of interest, the cell areas measurements, and lastly, performing new electrical comparison measurements.

The parameters considered for the scribing process on this sample are the wavelength of 1064 nm, pulse frequency 25 kHz, power 3-Watt, distance from the focal plane where the sample is placed, and focus = 0. Two different tracking speeds: 2000 mm /s (group A), and 1000 mm /s (group B).

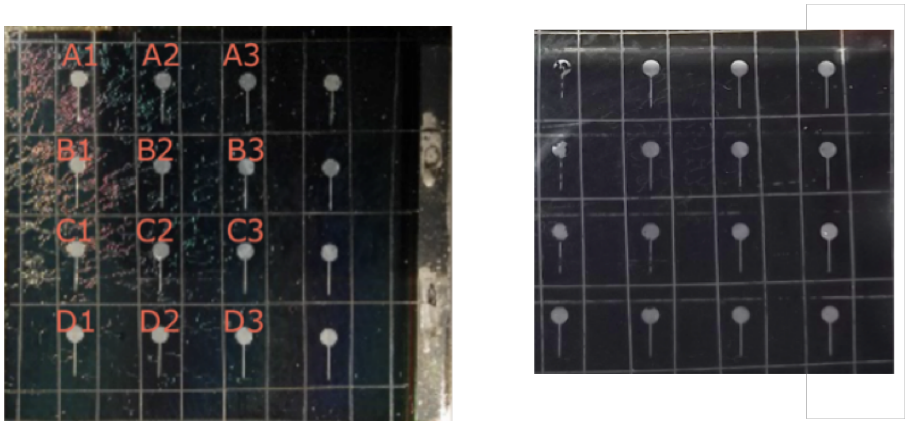

(a) (b)

Figure 3.1: Figure (a) represents the standard CIGS sample before the laser scribing and figure (b) represents after scribing.

As observed, it was determined to involve each cell with a single laser cut; Consequently, of the four sides of each cell, three were marked by mechanical scribing, while one side was replaced with laser scribing. After laser scribing, some characterizations are carried out: visual and optical microscope analysis, electron microscope evaluation, and electrical measurements. This experiment aims to verify the performance of the cells through electrical measurements on the solar simulator:

- Pre-Laser scribing
- Post Laser
- After ultrasonic washing with propanol (for 3 minutes to remove TCO fragments present on the surface)

Cell data before laser scribing: $V_{oc} = 678mV, I_{sc} = 1.82mA, FF = 54.5, Rs = 45Ohm, R_{sh} = 3344Ohm$.

R_{sh} **(shunt resistance):** Resistance that models all the internal losses of the photovoltaic cell. R_s **(series resistance):** Resistance that models all those loss factors that the current encounters in its passage or for example the absorber-back contact

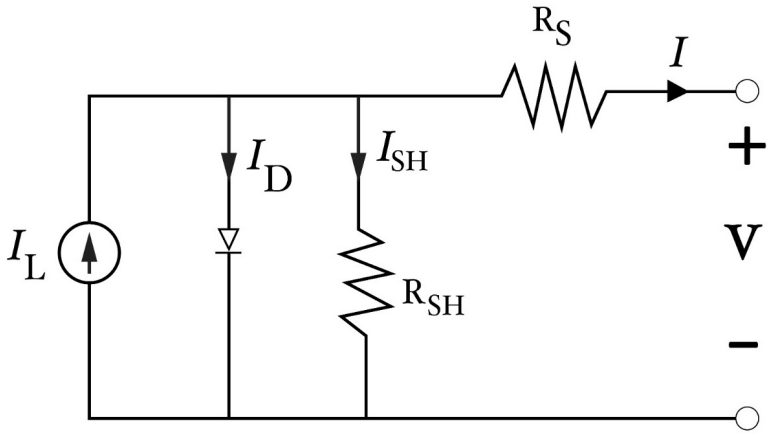

Figure 3.2: Schematic of solar cell

resistance, the resistance of the upper and lower contacts of the entire cell. Fill Factor (FF) is a dimensionless parameter that measures the degree of purity and correct exploitation of the cell as a percentage of achievement of the product's ideality IV.

$$FF = \frac{V_{mpp} I_{mpp}}{V_{oc} I_{sc}} \tag{3.1}$$

3.2.1 Measurement of the cell areas and visual analysis

It must be considered that the original area of the identified cells is reduced by the laser scribing, therefore the current extracted from each of them is also proportionally. The areas are then accurately measured under the electron microscope during the analysis session carried out to characterize the morphology and composition of the scribing.

The table 3.1, shows in the two and three number columns the surface in mm2 of the areas defined by mechanical scribing and laser scribing respectively. The rightmost column shows the percentage of each area obtained compared to the original. On average we have performed a reduction of the area to 80%, consequently we must expect a similar reduction in the I_{sc} currents that we are going to measure.

celle/aree	mm2 mecc	mm2 LS	var
A1	11.1	8.5	0.76
A2	13.1	10.2	0.78
A3	12.5	9.6	0.77
A4	13.4	9.9	0.74
B1	8.9	7.0	0.78
B2	10.9	8.8	0.81
B3	10.7	8.4	0.79
B4	11.4	8.6	0.76
C1	11.7	9.3	0.79
C2	12.1	9.7	0.80
C3	12.4	9.8	0.79
C4	13.9	10.8	0.77
D1	10.2	8.1	0.80
D2	11.8	9.6	0.82
D3	12.3	9.9	0.81
D4	12.6	9.7	0.78
		media	0.784

Table 3.1: Cells area measurements of CIGS sample.

	Voc	Isc	FF	Rs	Rsh		Voc	Isc	FF	Rs	Rsh
A1	707	1.29	52.3	19	2112	C1	716	1.646	51.8	59	3093
A2	674	1.951	50.7	47	1638	C2	699	2.001	58.2	18	3963
A3	583	2.05	42.7	114	1399	C3	663	2.205	56.9	28	3037
B1	719	1.262	50.4	31	2918	D1	703	1.831	62.1	24	9783
B2	703	1.849	62.3	26	2843	D2	690	1.836	56.1	36	5049
B3	648	1.828	55.1	96	2366	D3	631	2.06	55.8	27	1925

Table 3.2: The preliminary measurements of the sample after the mechanical scribing process.

The table 3.2, illustrates the preliminary measurements on the sample after having done the mechanical scribing.

Visual analysis: Analysis under the optical microscope, some disruptions are observed in the A lines (V = 2000 mm/s); and all four traces exhibit a jagged, uneven appearance.

3.2.2 SEM analysis of Standard CIGS solar cells

All scribing traces do not show signs of melting which is the main and most significant issue that occurs in laser scribing and which can determine a net deterioration in the Photovoltaic cell performance. Lines A appear not completely continuous and often involve a double layer of the structure (TCO and CIGS). The B lines are wider, even if it is discontinuous, but seem to affect only the most superficial layer. This is despite the halved speed which would imply a double influence and, therefore greater effectiveness of the incision. However, we must consider that some technical aspects may negatively affect this for example, insufficient uniformity of the thickness of the TCO over the entire sample or a misalignment of the sample in the plane concerning the propagation of the laser beam.

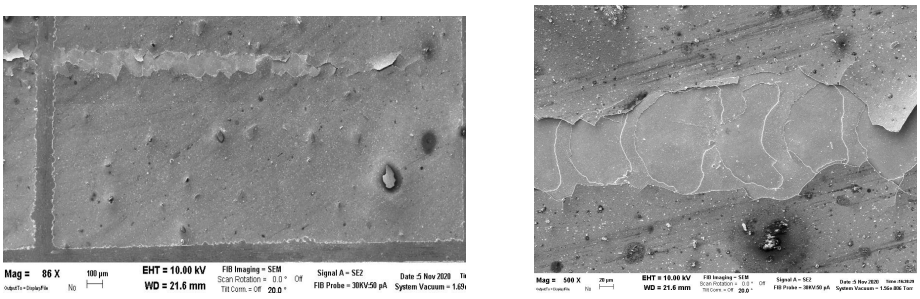

(a) (b)

Figure 3.3: (a) Cells D4, (b) D2: areas with TCO and partial removal of CIGS, inhomogeneity of the cut. In other places the TCO is not removed.

The cells created were thus affected by the laser scribing carried out: V = 2000 mm / s LS A on cells C1, C2, C3, D1, D2, D3 V = 1000 mm / s LS B on cells: A1, A2, A3, B1, B2, B3

The tables 3.3 summarize the percentage variations of the parameters of the cells affected by the two-laser scribing used.

var-1	Voc	-1	Voc
-19	Isc	-15	Isc
-2	FF	3	FF
-23	Sup	-20.5	Sup
121	Rs	20	Rs
15	Rsh	-22	Rsh

Table 3.3: Percentage variations of the parameters of the cells affected by laser scribing

3.2.3 Compositional analysis (EDX) of the Standard CIGS solar cells films

The compositions in the areas inside and outside the laser traces have been verified. It highlights the elimination of the TCO and the presence of the absorber, as desired in the so-called modified LS P3.

Post laser scribing electrical measurements: Under standard lighting conditions with the solar simulator (1KW / m^2 = 100mW / cm^2), the electrical parameters of 12 cells with surfaces of the order of $10mm^2$ were measured.

Summary of mean cell data after laser scribing: $< V_{oc} >= 720mV, < I_{sc} >= 1.59mA < FF >= 55, R_s = 91.5Ohm, R_{sh} = 2962Ohm$

3.3 Data Analysis of Standard CIGS solar cells

The data analysis, grouping the percentage variations of the electrical parameters of the cells and surfaces, allows us to make some observations:
The cell areas have been reduced on average by 20% and the drop in currents observed in laser scribing A is in good agreement with the drop in the cell surface, while in case B it is less. That indicates, in some cases, the effective area of the cell has not been reduced due to superficial scribing or that presents discontinuities (cells C3, D3). The work tensions are essentially unaffected; this is as expected, and it is

an excellent result; which means that the properties of the absorber (CIGS) have not been altered. Also, the fill factor (FF) is on average constant but there are three cases in which it has increased by more than 15% (B1, C1, D2). For this benchmark, the laser scribing on B looks better. The series resistances on average deteriorate in both groups, although there are three cells with an improvement (decrease) of 10% (B2, C1, D2). On the other hand, Shunt resistance improves in the first group while they worsen in the second. However, it should be noted that in the latter they are twice as large on average (4KOhm vs. 2KOhm) Relative changes in efficiencies show wide variability and are therefore not particularly significant in this test. Considering the presence of parts of TCO partially removed but still present on the cells which can be observed in SEM image. After electrical measurements, the sample was washed with propanol in an ultrasonic bath for three minutes and then dried at 50°. The simulator measurements were then repeated. Some important parameters have been observed by these experiments. Such as the V_{ocs} are unchanged, and some I_{sc}have worsened, but during the treatment, the metal contacts deposited on the TCO are partially damaged. The shunt resistances are increased, those of the LS B more; a very good signal indicating better cell insulation. The efficiencies are on average unchanged. In conclusion, the test shows extremely positive results, moreover, the cell efficiencies are unaltered, and an improvement in insulation (R_{sh}) and in some cases also in the fill factor (FF) is observed. This confirms that the proposed idea of carrying out modified P3 scribing, that is, relating to the TCO layer only, can be successfully pursued on CuInGaSe-based solar cells on glass.

3.4 Cell with alternative absorber SB_2Se_3 on glass

Another type of cell consists of a multilayer similar to CIGS cells in which the absorber has been replaced by SB_2Se_3 which is a very interesting compound for its physical properties (high absorption, Eg = 1.17eV, absence of rare elements and/or harmful), also significantly studied and promising.

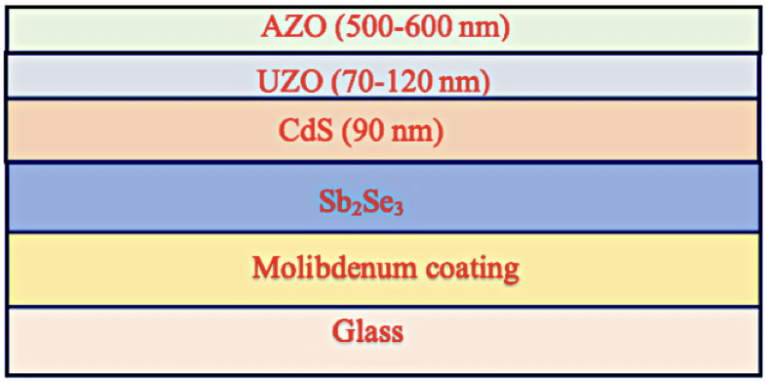

Figure 3.4: Multilayer Structure of Antimony selenide solar cell

The figure 3.4 represents the multilayer structure of the Antimony selenide cells: the structure is deposited with Glass + Mo coating, Sb_2Se_3 (1.5 microns), CdS (90 nm), UZO (70-120 nm), AZO (500-600 nm) respectively.

3.4.1 Detail of the laser scribing parameters

Wavelength=1064 nm Frequency, f = 25 kHz Power, P = 1.5, 1.9, 2.9 W (a, b, c) Mark speed, V = 1000-5000 mm/s (1, 2)

The higher speed allows us to observe the individual spots of the LS and therefore the effect on the multilayer.

3.4.2 Mechanical scribing of solar Cell with alternative absorber SB_2Se_3 on glass

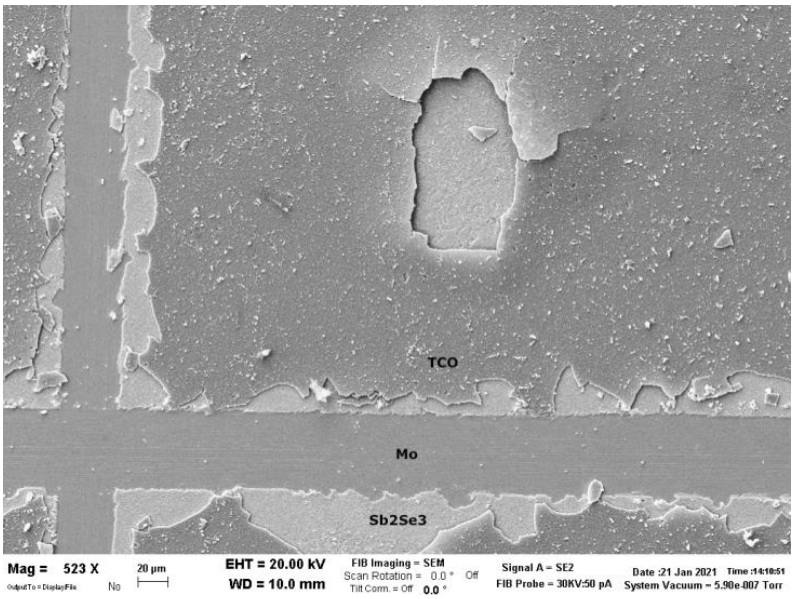

Figure 3.5: SEM of SB_2Se_3

SEM of SB_2Se_3: We can observe 3.5 the removal of the TCO and the conservation of the absorber which is intact. For comparison, mechanical scribing eliminates the various layers up to the Molybdenum that covers the glass.

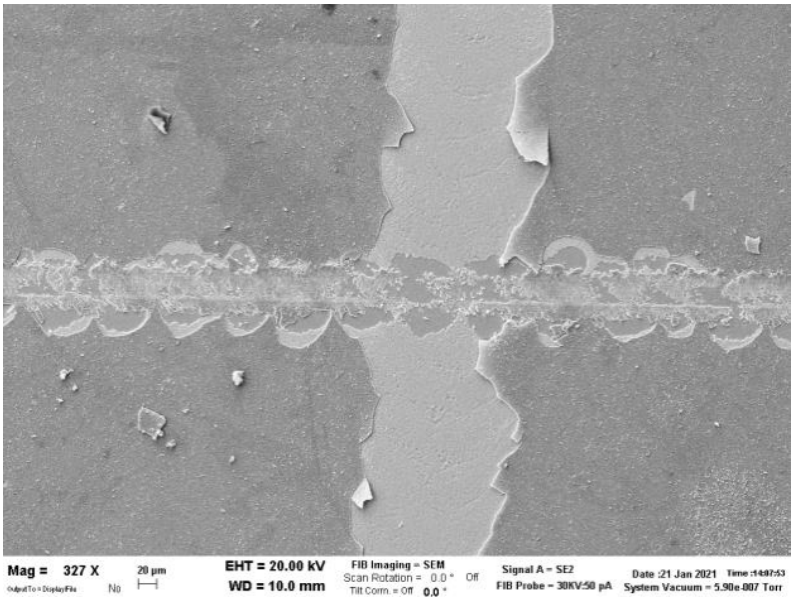

Figure 3.6: Compositional Analysis (EDX)

Compositional Analysis (EDX): In 3.6 we see the Laser scribing vertically and the mechanical scribing horizontally. The greater damage that the latter does on the multilayer compared to the LS is evident. The compositions in the areas inside and outside the scribing were checked both in the continuous track and in the individual spots. It highlights the absence of the TCO and the presence of the absorber, unlike the mechanical scribing.The width of the LS is about 160 μm which is an indication of a marked overlap of various spots which are about 100 μm with the same power. The results of this test are promising. The parameters used (f = 25kHz, P = 2.9 W, V = 1000mm / s) are effective in homogeneously removing the TCO even if the trace is still too wide. It is then necessary to check on functioning cells if there are electrical alterations. The spot traces confirm that the power used is adequate to remove the TCO without altering the underlying layer.

Laser Scribing parameters: Wavelength = 1064 nm, f = 25 kHz, P = 2.9-Watt, V = 1000 (1,2,3), 2000 (4,5,6) mm/s. Hence the source used in this configuration is potentially effective in the LS of Sb2Se3 based cells. Here we report an example of

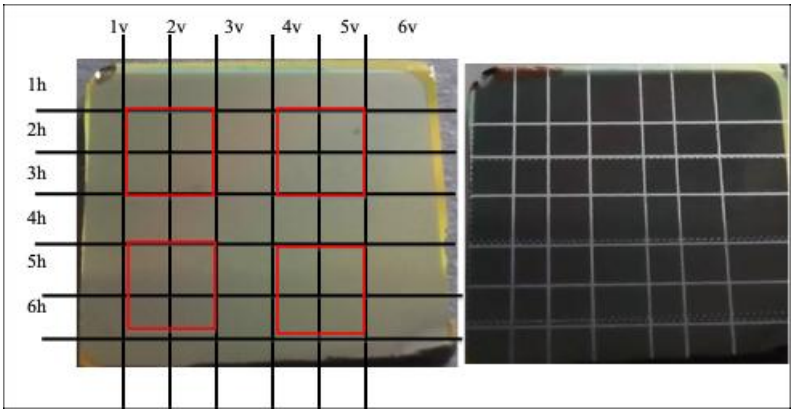

Figure 3.7: Sb_2Se_3 based cells (right before LS and left after LS)

making cells on a sample of one square inch. Two scribing speeds were used (v = 1000 mm / s trace 1-3 and 2000 mm / s trace 4-6) thus identifying four homogeneous groups of cells, see 3.7.

3.4.3 SEM analysis of Sb_2Se_3-based cells Laser scribing

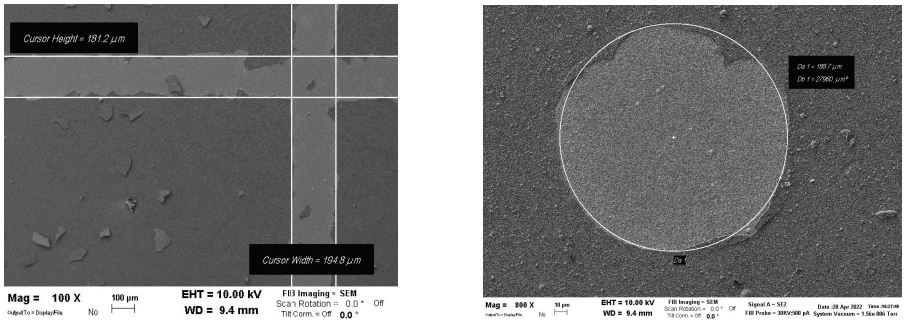

(a) (b)

Figure 3.8: Figure (a) shows the size of the traces of about 200 microns and the presence of fragments of the removed surface layer. Figure (b) shows the effect of the single spot: there is the removal of the TCO, while the underlying surface is intact.

The visual analyses and the SEM images show (in 3.8) that all the traces are visible and defined, with a width of around 200 microns.

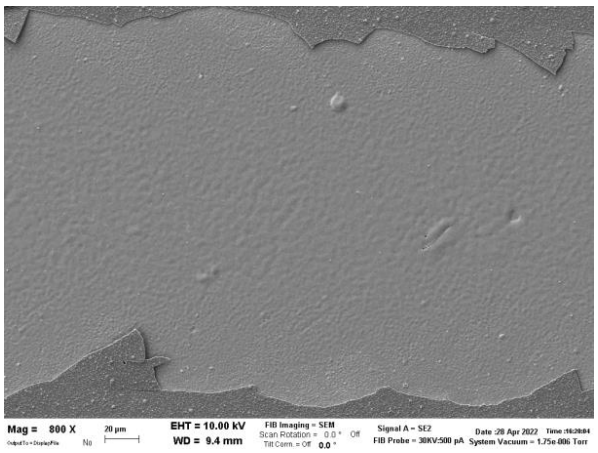

Figure 3.9: These 800x images show that there is no evidence of absorber investment casting within the track (well-known effects).

3.4.4 EDAX measurements of Sb_2Se_3 based solar cells Laser scribing

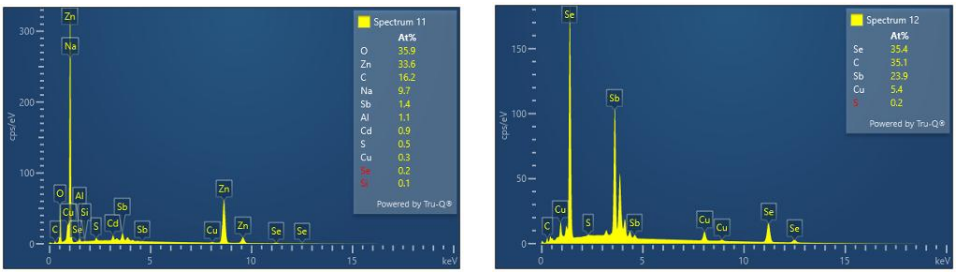

(a) (b)

Figure 3.10: EDAX trace comparison 1000 (2v, 3h) (a) vs. 2000mm/s (5h, 5v) (b)

EDAX measurements inside and outside the traces confirm the removal of the TCO and the preservation of Sb_2Se_3, Figure 3.10.

LS Sb2Se3 solar cell			Riferimento locale su TCO	
linea	Sb%	Se%	Sb%	Se%
2v	24	35.8	2.5	0.4
3h	23.4	35.2	2.5	0.4
5h	23.29	35.4	1.4	0.2
5v	23.9	35.4	1.5	0.2

Table 3.4: Differences between the Laser Scribing of two different speeds and the TCO .

There are no noticeable differences in table 3.4 between the Laser Scribing for two different speeds and the TCO has been completely removed. This indicates that the higher speed (2000 mm / s) can be used effectively. **Electrical measurements on the solar simulator:** The tests were carried out under standard conditions by placing the metal measuring tips directly on the TCO without the affixing of metal contacts (Ag). Molybdenum, back contact is achieved by removing the overlying structure in a small corner of the sample.

The average values of all the identified cells of the characteristic parameters are:

$J_{sc} = 2.7mA/cm^2$
$V_{oc} = 156mV$
$FF = 28.5\%$
$\nu = 0.1$
$R_s = 1.2Ohm * cm^2$
$R_{sh} = 70Ohm * cm^2$

	<Jsc>	<Voc>	<FF>	<ETA>	<Rs>	<Rsh>
LS1000	3.6	114	29	0.1	1.1	36
LS2000/1000	3.2	196	28	0.2	1.1	63
LS1000/2000	2.1	186	30	0.1	1.3	102
LS2000	1.7	128	27	0.1	1.4	78

Table 3.5: Comparison table mechanical scribing for different scribing speeds for four groups of cells.

For comparison, we made a small mechanical scribing in a central area, obtaining very similar values. Considering the four groups of cells drawn, we can verify if there are differences in the speed of the LS performed. The results reported on table 3.5

Considering the presence of TCO fragments that can reduce the electrical performance, the sample was washed with ethanol in ultrasound for 3 minutes. The electrical measurements were then repeated. Unfortunately, there is a reduction in V_{ocs} of over 50% on all cells, while the currents are constant. Therefore, this type of treatment is not recommended for these structures.

3.5 Laser scribing of another type of Sb_2Se_3-based cells

Another experiment was done on a sample of a similar structure in which the cells were made on one half with photolithography (15 cells) and on the other with laser scribing (4 x 8 lines, 21 cells) **Laser Scribing parameters:** λ = 1064 nm f = 25 kHz P = 2.9 Watt V = 2000 mm / s

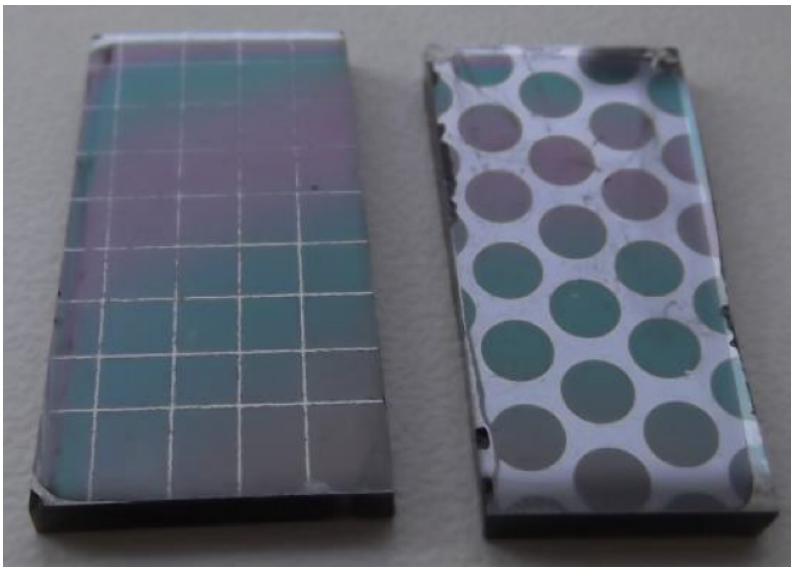

Figure 3.11: Electrical measurements on the solar simulator.

The tests were carried out under standard conditions by placing the metal measuring tips directly on the TCO without the affixing of metal contacts (Ag). Molybdenum, back contact is achieved by removing the overlying structure in a small corner of the sample. See figure 3.11

The average values of the characteristic parameters on all cells obtained by photolithography are described in table 3.6

In the part subjected to laser scribing, the measurements on 13 cells show that they are not correctly isolated from the rest of the sample; in fact, the current values are higher than those observed in the reference sample half and the shunt resistances

Parameters	Values
<Jsc>	11 mA/cm^2
<Voc>	191 mV
<FF>	33%
<v>	0.7
<Rs>	3 Ohm * cm^2
<Rsh>	21 Ohm * cm^2

Table 3.6: The average values obtained by photolithography

are lower than 10 Ohm x cm^2.

Therefore, we consider only seven cells we get these average values in table 3.7

Parameters	Values
<Jsc>	17 mA/cm^2
<Voc>	156 mV
<FF>	29%
<v>	0.8
<Rs>	2 Ohm * cm^2
<Rsh>	12 Ohm * cm^2

Table 3.7: The average values obtained by photolithography (only seven cells are considered)

From this test we can draw some useful indications: considering that the thicknesses of the TCO have a gradient on the sample (see in the photo the colors of the surface) and fluctuations in the subsequent depositions, to obtain an effective isolation in a reproducible way it is advisable to reduce the speed of the scribing at 1000 mm / s, thus increasing the effect of the cut. We observe a significant reduction in V_{oc}; therefore it is necessary to qualitatively improve the LS to reduce the sources of recombination in the cells. In conclusion, we can say that with this test we have consolidated the possibility of using LS on these new Sb_2Se_3 solar cells.

3.6 Semi-transparent solar cells

Another new type of cell is that of semi-transparent cells consisting of transparent electrical contacts on both the front and back and a thinner absorber than traditional cells. The use of semitransparent is coupled with other cells (tandem structure). This project aims to develop cells with CIGS absorbers that can be coupled to silicon-based cells to increase their efficiency. Also, on these structures, it is interesting to understand and develop the possibility of using laser scribing for the P3 stage.

Some tests were then conducted on complete structures as follows:

Glass with SnO_2: F (FTO coating) CuInGaS (by spin coating) CdS (90 nm) UZO (70 - 120 nm) AZO (500-600 nm)

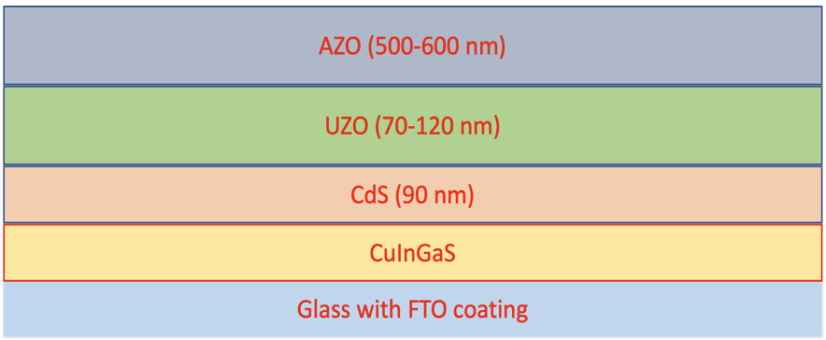

Figure 3.12: Multilayer Structure of semitransparent solar cell

Considering that the final structure (TCO) is the same as used in the standard cells, the parameters of the laser scribing used were the same. Laser scribing parameters: Wavelength = 1064 nm, f = 25 kHz, Power = 2.9 Watt, Scribing speed V = 1000 and 2000 mm /s.

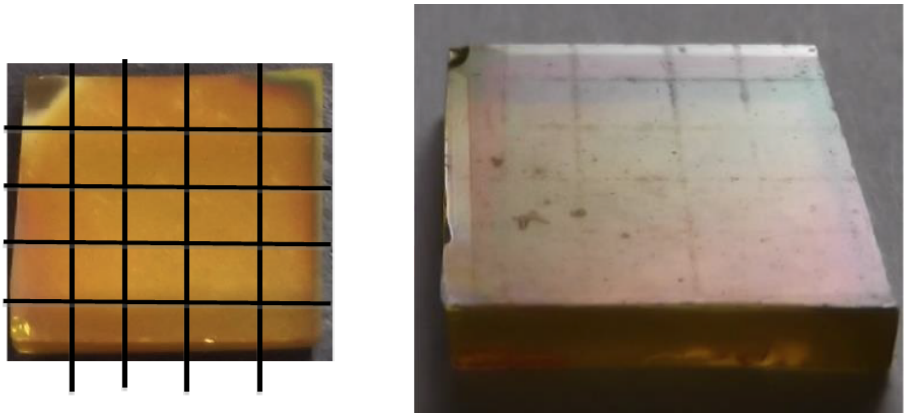

(a) (b)

Figure 3.13: Multi-layer semitransparent cell (a) before LS and (b) after LS.

3.6.1 Semi-transparent solar cells (Scribing speed V = 20, 30, 50, 100, 200, 500 mm /s)

We tested another scribing process with different scribing speeds for each line. Laser scribing parameters: Wavelength = 1064 nm, f = 25 kHz, Power = 2.9 Watt, Scribing speed V = 20, 30, 50, 100, 200, 500 mm /s It can already be seen visually from the picture below, that the traces appear weak and unfortunately, this is confirmed by the electron microscope analysis where we only occasionally see the TCO removed. EDAX measurements confirm the non-removal of the layer. The fluence on the sample was then increased by lowering the etching speed (20, 30, 50, 100, 200, 500 mm /s) and with multiple scribing (50mm /s 2x 3x).

3.6.2 SEM analysis of 50 mm / s 3x, 30 mm / s, 20 mm / s

In Figure 3.15, there are the SEM images of the three traces obtained at speeds (left-right) 50 mm / s 3x, 30 mm / s, and 20 mm / s.

The SEM survey shows that even by greatly reducing the speed of the beam, the surface is engraved but not sufficiently to remove the ZnO layer.

The reduced effectiveness of Laser scribes in removal is due to the reduced ab-

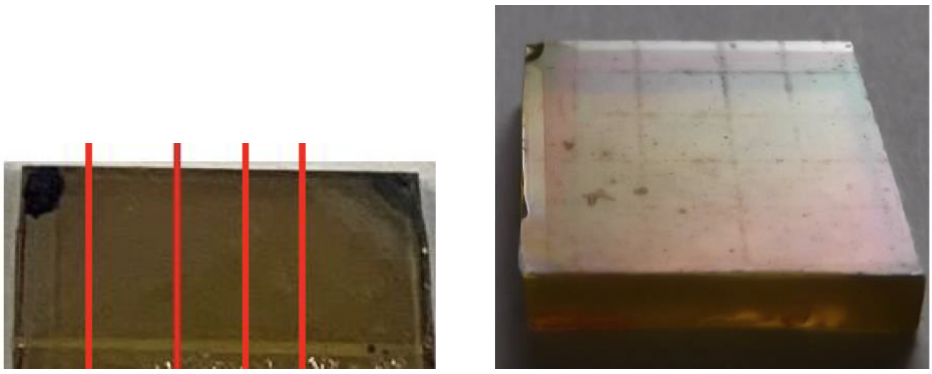

(a) (b)

Figure 3.14: Laser scribing by (50mm / s 2x 3x, 30mm / s, 20mm / s)

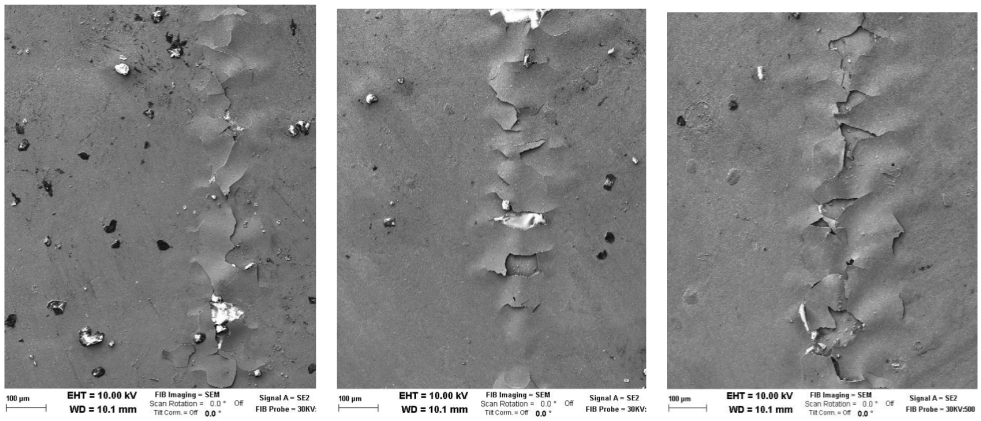

Figure 3.15: SEM image of solar cell for three different speeds (left) 50 mm/s, 3x (middle) 30 mm/s, (right) 20 mm/s

sorption of the radiation used. We then went to verify the optical behavior of this structure with a spectrophotometer optical absorption measurement (Jasco V770 UV-nearIR). Actually, the absorbance at λ = 1064 nm is only 0.35 (see figure below). Since the absorbance is related to the ratio of the fluxes (i.e. the powers) by Abs = Log (1 / T), T = ϕt / ϕi, a small calculation tells us that at 1064 nm the useful power is about 55% of that incident, then 1.6 Watts starting from an initial power of 2.9 Watts.

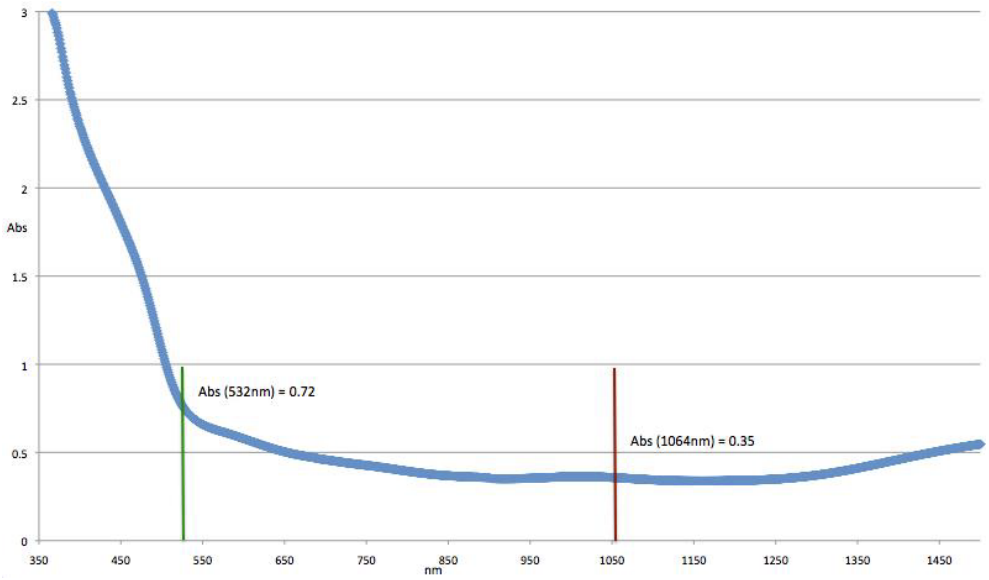

Figure 3.16: Abs graph

Analyzing the curve in figure 3.16, we observe that by doubling the frequency of the radiation emitted by the laser we can increase the effective radiation on the sample from 1.6 W (at 1064nm) to 2.4 W (at 532nm).

3.6.3 Semi-transparent solar cells (Scribing speed 20, 50, 100, 200, 500 mm / s)

Another sample was then tested with the same nominal structure using the following parameters for laser scribing:
λ = 532 nm
f = 25 kHz
P = 2.9 Watt
Five parallel lines at mark speed: 20, 50, 100, 200, 500 mm / s Analyzing the curve,

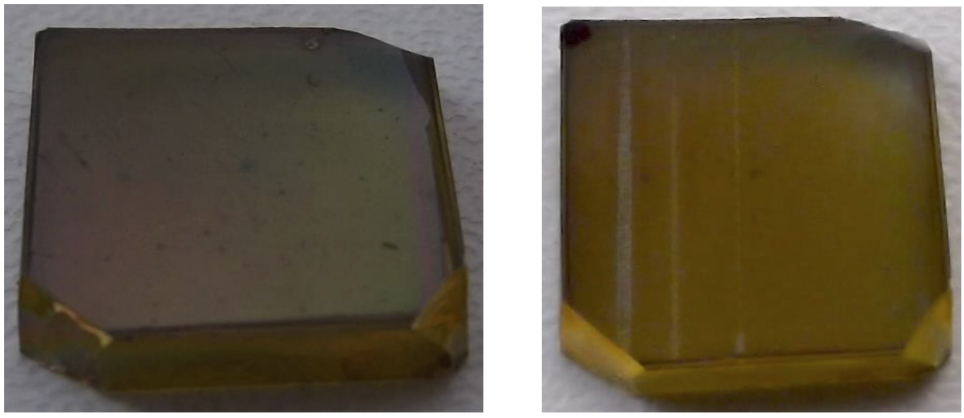

Figure 3.17: Laser scribing by speed 20, 50, 100, 200, 500 mm / s, before (left) and after (right) LS

we observe that by doubling the frequency of the radiation emitted by the laser we can increase the effective radiation on the sample from 1.6 W (at 1064nm) to 2.4 W (at 532nm). Another sample was then tested with the same nominal structure using the following parameters for laser scribing: λ = 532 nm f = 25 Hz P = 2.9 Watt 5 parallel lines at mark speed: 20, 50, 100, 200, 500 mm/s Above the sample (figure 3.17) before and after the test. On visual observation only the three traces at the lowest speed are visible; under the optical microscope, the most homogeneous trace is the one at a speed of 50 mm / s.

3.7 SEM-EDAX analysis (20,50,100 mm/s)

The SEM analysis confirms that the effects are visible at the three lowest speeds; we see in these images (from left to right) that at the speed of 20 mm / s, the trace is very wide (about 500 microns) and the channel is covered by the debris of the structure, rising to 50 mm / s a trace of 160 microns is observed in where there is the removal of the film; the width is comparable with the traces made on the other thin-film cells. Finally, the scribing made at 100 mm / s shows a discontinuous trace.

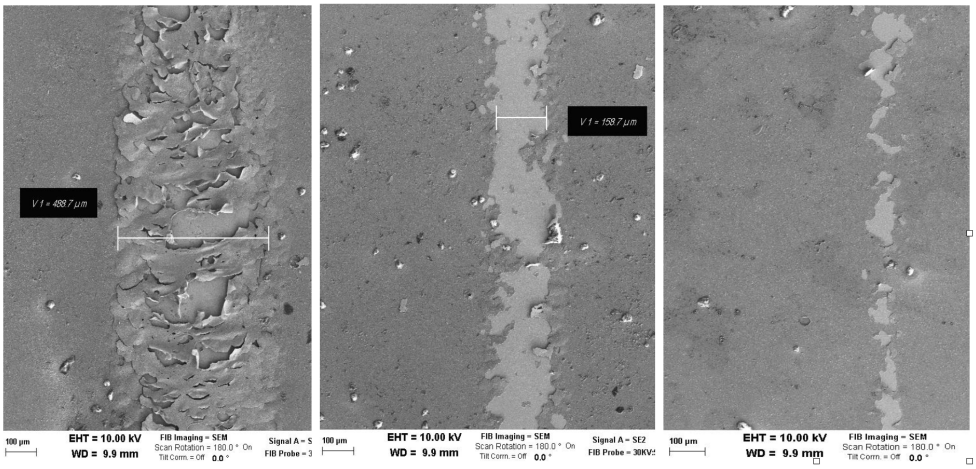

Figure 3.18: SEM-EDAX analysis

The EDAX analysis carried out in the channel of the second trace shows (in figure 3.18) the removal of the structure, so we can say that for this type of CuInGaS-based semitransparent structures, the use of the 532 nm laser source allows the cells to be effectively separated.

Chapter 4

Doped-fiber Lasers

4.1 Fiber Laser

The active medium is doped with rare earth elements in a laser is signified as fiber laser. The core of the fiber laser is doped with rare earth elements for instance, ytterbium (Yb), erbium (Er), thulium (Tm), or dysprosium (Dy). These elements are utilized to dope the core of the laser or active medium where lasing occurs, which helps to focus the light to be emitted in a simulated amplification. The gain of fiber lasers is significantly tremendous because of their compact length, performance, robustness, and capability to offer excessive-power outputs with excellent beam quality compared to conventional laser and gas lasers which are also complex and heavier than fiber lasers [95]. Fiber lasers are economically advantageous and the fabrication process of these lasers is comparatively straightforward. Emitting high-quality beams along numerous parts of the electromagnetic spectrum associated with infrared, visible, and ultraviolet ranges, makes fiber amplifiers and lasers one of the most prosperous tools in diverse areas of the photonic field. because of these remarkable attributes. Fiber lasers are well-suited in telecommunications, medicine, manufacturing, and metrology. To meet these industries' growing needs, various fiber lasers have been developed, including continuous wave, pulsed, narrow-linewidth, single-frequency, tunable, and high-power lasers. The configuration of a fiber laser involves a gain

medium, and this optical fiber is doped with rare-earth ions, along with a feedback mechanism. this is established by a resonant cavity. The feedback can be made using mirrors or a fiber Bragg grating (FBG) embedded in the fiber core. This arrangement helps reflect desired frequencies [96].

4.2 Basic Principle of fiber laser

The picture below illustrates the fundamental working principle of a fiber laser. three main components of a fiber laser are gain medium, pump source, and feedback or optical resonator.

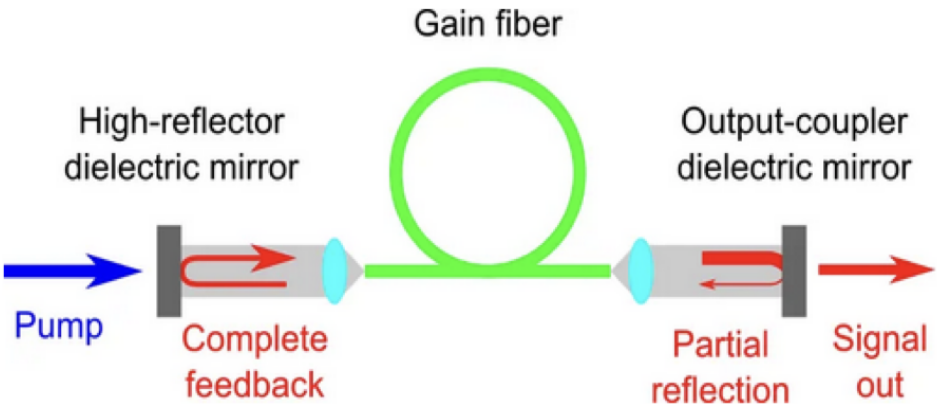

Figure 4.1: Diagram of the setup for a fiber laser. The main components (pump source, gain medium of laser, and feedback) of a fiber laser structure are shown in the figure above [97].

4.2.1 Gain medium of a fiber laser

The core component of a fiber laser is its gain medium. which is also referred to as the heart of the laser, light amplification, through a stimulated emission occurs inside the gain medium. Moreover, it contains an optical fiber that is doped with rare-

earth elements for instance erbium (Er), ytterbium (Yb), neodymium (Nd), and many others. By a pump source of the fiber laser, the energy of the dopants is absorbed. This absorption causes excitation. Emission of photon happens while it come back again to lower energy states. This incident amplifies the light inside the fiber core. The output power and wavelength of a laser is determined by the dopant types. Such as the Er-doped fiber wavelength range (approximately 1550 nm), whereas Yb-doped fiber (around 1060 nm) is used for high-power purposes.

4.2.2 Pump Source

For stimulated emission, the pump source of the fiber laser plays a significant role. It delivers the required energy. that provided energy by the pump source helps to excite the ions inside a gain medium. Laser diodes are usually selected as pump sources in fiber lasers due to their beneficial properties. The efficiency is high for the laser diode, it can also provide high power. The light from the pump diode is directed into the fiber's cladding, which surrounds the core containing the gain medium. The doped ions in the core absorb this energy and release photons via stimulated emission, amplifying the light [98].

4.2.3 Feedback of laser

Laser light can be generated through the feedback mechanism of a laser. Feedback allows pump light to travel back and forth inside the cavity. Since light travels from one end to another, this back-and-forth action simultaneously excites photons from the ions. This occurs by stimulated emission. Two fundamental processes are required to accomplish stimulated emission.

Mirrors: two mirrors are positioned at both ends of the fiber; mirrors permit to reflect the light back into it. More photon emissions are generated by this reflection of light into the cavity.

Fiber Bragg Gratings (FBG): This includes designing a periodic change in the fiber's refractive index. This is also known Bragg filter, which allows reflecting only specific wavelengths of light, and only these specific wavelengths can be amplified

through this filter. Both approaches assist in the circulation of light inside the laser cavity and increase the output efficiency [97, 98].

4.3 Fiber laser wavelengths

Rare earth elements (ytterbium, erbium, dysprosium, thulium, and many more) are integrated into the core of the fiber laser. This material was chosen according to the need for application and efficiency in the required fields. Typically, erbium is used for generating output near the wavelength of 1550 nm, emission range for erbium fiber laser is 1528 nm to 1620 nm. For the application of sensing pulsed fiber lasers wavelength around 1550 nm is mostly acceptable worldwide., since it has high output power near a wavelength range of 1.5 microns that is eye-safe. Particularly, ytterbium has a very unique ability to emit photons in the 1-micrometer range, approximately 1030 nm, 1064 nm, and 1080 nm wavelength. Combining two different rear earth materials such as ytterbium and erbium, obtaining an output power of 5 watts at a wavelength of 1550 nm is possible. In this method, Yb ions excite to transfer energy to erbium ions. In this process, emission is required. [99, 100].

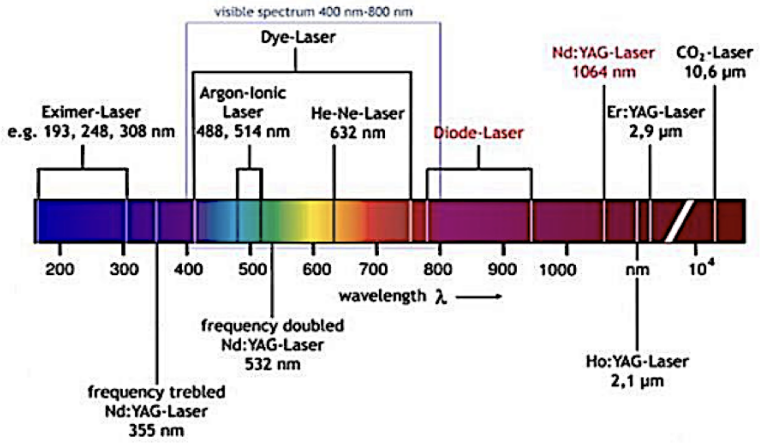

Figure 4.2: Laser wavelength spectrum for different laser types [99].

4.4 Categories of different rare-earth-doped fibers and their emission wavelength

Rare-earth-doped fiber lasers are widely used for numerous purposes of industrial and manufacturing methods for instance during laser cutting, welding, cleaning, and precision processing it is commonly applied. Through multiple wavelength ranges, this laser operated. This includes 1050–1120 nm for ytterbium-doped fiber lasers, 1530–1590 nm for erbium and erbium-ytterbium-doped fiber lasers, and 1900–2100 nm for thulium and holmium-doped fiber lasers [101].

Rare Earth Element	Types of Host Glasses	Wavelengths of Emission
Ytterbium (Yb^{3+})	Silicate glass	1.0-1.1 μm
Neodymium (Nd^{3+})	Silicate and phosphate glasses	1.03-1.1 μm, 0.9-0.95 μm, 1.32-1.35 μm
Erbium (Er^{3+})	Glasses, fluoride glasses	1.5-1.6 μm, 2.7 μm, 0.55 μm
Thulium (Tm^{3+})	Silicate and germanate glasses, fluoride glasses	1.7-2.1 μm, 1.45-1.53 μm, 0.48 μm, 0.8 μm
Praseodymium (Pr^{3+})	Silicate and fluoride glasses	1.3 μm, 0.635 μm, 0.6 μm, 0.52 μm, 0.49 μm
Holmium (Ho^{3+})	Silicate glasses, fluorozirconate glasses	2.1 μm, 2.9 μm

Table 4.1: Commonly used laser-active ions, name of the host glasses, and emission wavelengths for different fiber laser [102, 103].

Erbium (Er^{3+}): erbium fiber laser emits light at 1550 nm. The application of Er3+ in telecommunication and optical sensors has increased significantly over the years. The host glasses for erbium are silicate and fluoride glasses. Ytterbium (Yb^{3+}): For high-power fiber laser it has a wide range of applications. The wavelength from 1030 to 1080 nm is ultimate for material processing, cutting, and welding. Since

the heat management and output energy are tremendously high. Silicate glasses are mainly used as host glasses for ytterbium laser.

Thulium (Tm^{3+}): in medical applications, surgery employs fiber laser, the field of defense, and many research-based projects thulium shows promising results. This is because of their high wavelength and many unique characteristics. Light emits in a wide range, between 1.45 μm and 2.1 μm. in shorter wavelengths such as 0.48 μm and 0.8 μm. Host materials are Silicate, fluoride glasses, and germanate.

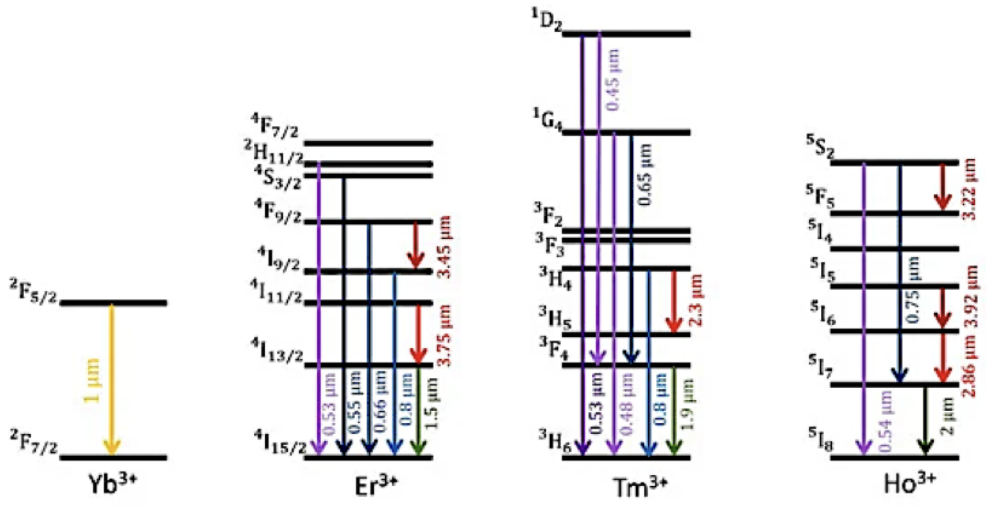

Figure 4.3: Energy levels diagram and transitions for a different doped fiber laser. this figure represents (Yb^{3+}), (Er^{3+}), (Tm^{3+}), and (Ho^{3+}) ions respectively .

Neodymium (Nd^{3+}): In medical technology, industrial machining, and laser indicators, neodymium-doped lasers are tremendously versatile. The emission wavelength is 0.9 μm to 1.35 μm. The host material is phosphate glasses, silicate.

Holmium (Ho^{3+}): In medical laser lithotripsy for kidney stone surgery holmium laser can be utilized. The emission wavelength is 2.1 μm and 2.9 μm. Host glasses are silicate.

Dysprosium (Dy^{3+}): Dysprosium-doped materials can emit light at wavelengths around 2.9 μm (microns), which is within the mid-infrared (IR) region. Fluoride,

phosphate, or germanate glasses are the host materials. Fluoride glasses, for example, ZBLAN (Zirconium Barium Lanthanum Aluminum Sodium Fluoride), are alternatives since they offer low phonon energy, minimizing non-radiative losses that can quench the emission in the mid-IR region [101].

4.5 Dysprosium-doped yellow fiber laser

Dysprosium ions are used in Dy-doped fiber laser. To create yellow light, dysprosium-doped active core of the laser performs a significant role. Direct yellow emission occurs between wavelengths of 570 nm to 590 nm. This advanced yellow laser has potential for the researcher due to its capability to produce yellow emission without any complex features and it has more output efficiency. yellow emission is hard to achieve by other conventional laser gain mediums. Dy-doped fiber lasers are pumped by a blue diode laser [104]. The (Dy^{3+}) ion creates a strong yellow fluorescence due to the transition from the energy level of ${}^4F_{9/2}$ and ${}^6H_{13/2}$ energy levels. In a ground-breaking investigation, the research group of J. Limpert et al. for the very first time demonstrated continuous wave (CW) yellow emission at room temperature from a Dysprosium-doped ZBLAN fiber laser. The wavelength range is 575 nm and 478 nm, and output power is in the milliwatt level. This was achieved by using a bulky, air-cooled Argon-ion laser emitting at 457 nm as the pump source. Later in 2011, advancements were made using a fluoro-aluminate glass-based (Dy^{3+})—doped optical fiber, which had a low loss of 0.3 dB/m at 532 nm, enabling yellow laser oscillation [105]. During 2020, developments in Dy-doped fluoride fiber construction and the progress of high-power Gallium nitride (GaN) laser diodes, basically a blue diode that emits at 445 nm, resulted initial demonstration of a GaN laser diode. which is pumped Dy-doped ZBLAN fiber laser for yellow light emission. This was accomplished by employing a straightforward experimental arrangement, marking an important revolution in the field. In that investigation, the Dy-doped ZBLAN fiber used was initially intended for mid-infrared emission. To investigate the yellow laser performance, the researchers established two special fiber lengths, 0.6m and 5.95 m offer insights into how the length of fiber influences the efficiency of laser and laser

output [105, 106]. In 2021, again the research group of J. Limpert et al. investigated the objective behind the low preliminary slope efficiency they had encountered during the test. They observed that the fiber's background loss and the ESA which is excited state absorption of the intra-cavity for yellow light were dominant aspects. By experimental and hypothetical analysis of the level $^4F_{9/2}$ to $^6H_{13/2}$ lasing in the Dysprosium doped ZBLAN fiber, they observed the output with a maximum 33 % slope efficiency in a yellow laser, which is especially less than half of the Stokes limit, which is nearly 78% [107]. Despite these important progresses in Dy-doped yellow fiber laser research, the output power of the lasers remained controlled to the milliwatt (mW) range. However, the studies assist in an important understanding of Dy-doped fiber sources, attaining higher power is still a challenge in the laser fields [108, 109].

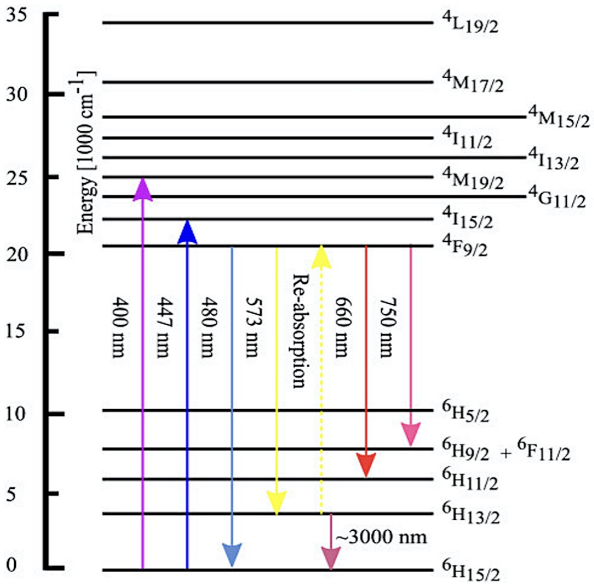

Figure 4.4: Illustration of Energy-level for Dy3+ in ZBLAN glass [107]. In this demonstrated figure ground-state absorption (GSA) for ∽400 nm and ∽447 nm have been marked by upward purple and blue arrows respectively. In ZBLAN glass, the lower laser level, the lifetime of $(^6H_{13/2})$ of the yellow laser is equivalent to the upper laser level $(^4F_{9/2})$, yellow light is re-absorbed [110, 111].

The wavelength range of 565 nm to 590 nm produces yellow emission is raising interest for their proper utilization in modern and prospective applications through a variety of areas, involving metrology, high-resolution spectroscopy, biomedical imaging, laser guide star systems, ophthalmology, and treatments for skin conditions for example acne melasma. These various functions emphasize the significance and versatility of yellow-emitting lasers in both scientific and medical technologies [112, 113, 114, 115, 116]. Dysprosium (Dy3+) is a tremendous candidate for constructing a yellow fiber laser that is more designed and efficient. The transition from the energy level $^4F_{9/2}$ to $^6H_{13/2}$ energy level, demonstrated in Figure 4.4 above, produces strong yellow fluorescence light. Compared to traditional methods such as dye lasers or nonlinear processes Dy3+ is predominantly attractive for emitting yellow

light in an effective approach these methods are more complicated and practically less suitable for compact designs [117, 118]. The erbium-doped fiber amplifier is the standard and easiest three-level energy model system. By this three-level system, important features of the amplifiers can be understood. However, for some rare earth ions with short cavities, this model is not sufficient to explain the system. For better understanding, a system with more than 3 levels is required. Such as: thulium, neodymium, and dysprosium ions. For our experiments, we have considered four four-level systems of Dysprosium fiber laser. The ground state is 0 level and the highest energy level state is three. In this state, usually, we pump the energy level one and level number two. this is considered a lower and upper-level lasing transition. Level 2 has a long lifetime for a highly efficient laser and amplifier compared to other levels. This is also known as a metastable state. N_0, N_1, N_2, N_3 are denoted as the population of the energy levels.

4.5.1 Rate equations of Dy+3 doped fiber laser:

The rate equations [109] explain the population in a four-level system of Dy3+ ions, also applied in Dy-doped fiber lasers. These rate equations show the effect of populations of different energy levels variation over time due to transitions between them, stimulated by pumping and spontaneous or stimulated emission.
Ground state N_0

$$\frac{dN_0}{dt} = -W_{03}N_0 + (W_{30} + A_{30})N_3 + A_{10}N_1 \tag{4.1}$$

First excited state population N_1

$$\frac{dN_1}{dt} = (W_{21} + A_{21} + W_{21f} + W_{21b})N_2 - A_{10}N_1 - (W_{12} + W_{12f} + W_{12b})N_1 \tag{4.2}$$

Second excited state population N_2

$$\frac{dN_2}{dt} = (W_{21} + A_{21} + W_{21f} + W_{21b})N_2 - A_{32}N_3 - (W_{12} + A_{12} + W_{12f} + W_{12b})N_1 \tag{4.3}$$

Third excited state population N_3

$$\frac{dN_3}{dt} = -W_{03}N_0 - (W_{03} + A_{30})N_3 + A_{32}N_3 \tag{4.4}$$

For a steady-state condition, the time derivatives will be zero and this can be written as below:

$$\frac{dN_0}{dt} = \frac{dN_1}{dt} = \frac{dN_2}{dt} = \frac{dN_3}{dt} = 0 \tag{4.5}$$

The total population N_t can be expressed below,

$$N_t = N_0 + N_1 + N_2 + N_3 \tag{4.6}$$

Equation from 4.1 to 4.6 can be written as below:

$$N_1 = \frac{ce - bf}{ae - bd}, N_2 = \frac{af - cd}{ae - bd} \tag{4.7}$$

where the coefficients of a, b, c, d, e, and f are respectively,

$$(W_{12} + W_{12f} + W_{12b} + A_{10}), (W_{21} + A_{21} + W_{21f} + W_{21b}), 0, \tag{4.8}$$

$$\frac{(W_{03} + A_{30} + A_{32} + W_{03})A_{10}}{W_{03}A_{32}} + 1, 1 and 1$$

Where,

$$a = W_{12} + W_{12f} + W_{12b} + A_{10}, b = W_{21} + A_{21} + W_{21f} + W_{21b} \tag{4.9}$$

$$c = 0, d = \frac{(W_{03} + A_{30} + A_{32} + W_{03})A_{10}}{W_{03}A_{32}} + 1, e = 1, f = 1$$

These equations define the population inversion and steady-state performance of a four-level Dy- doped fiber laser system [109]. Mathematical methods are often used to solve them and predict laser performance. P represents the power. whether for the pump or signal power or amplified spontaneous emission, $\sigma 12(21)$ is the absorption or emission cross-section between energy levels 1 and energy level 2.

Paremeter	Definition	Equation or Relation
W_{03}	Pump absorbtion rate at λ_p	$(\sigma_{03}P_p)/h\nu_p$
W_{30}	Stimulated emission rate at λ_p	$(\sigma_{30}P_p)/h\nu_p$
A_{30}	Spontaneous emission rate from level 3	$1/\tau_{03}$
A_{10}	Spontaneous emission rate from level 1	$1/\tau_{10}$
W_{21}	Stimulated emission rate at λ_S	$(\sigma_{21}P_s)/h\nu_s$
A_{21}	Spontaneous emission rate from level 2	$1/\tau_{21}$
W_{21f}	Stimulated emission rate at λ_{ASEf}	ASE term
W_{21b}	Stimulated emission rate at λ_{ASEb}	ASE term
W_{12}	Absorption rate at λ_S	$(\sigma_{21}P_s)/h\nu_s$
W_{12f}	Absorption rate at λ_{ASEf}	ASE term
W_{12b}	Absorption rate at λ_{ASEb}	ASE term

Table 4.2: Representation of the coefficient from the equation 4.1 to 4.7 [109]

4.5.2 Power propagation equations of Dy^{3+}-doped fiber laser

The power propagation equations [109] in a Dy-doped fiber laser explain the methods of the pump and signal powers evolving along the length of the fiber [109]. These equations account for the absorption of the laser pump, the stimulated emission of the signal, and losses in the fiber such as excited-state absorption (ESA) and fiber attenuation.

$$\frac{dp_p}{dz} = -\Gamma_p \sigma_{03} N_0 P_p + \Gamma_p \sigma_{30} N_3 P_0 P - \alpha P_p \tag{4.10}$$

$$\frac{dp_s}{dz} = -\Gamma_s \sigma_{12} N_1 P_s + \Gamma_s \sigma_{21} N_2 P_s - \alpha P_s + ASETerm(\lambda_s)\frac{N_2}{N_1} \tag{4.11}$$

$$\frac{dp_{ASEF}}{dz} = -\Gamma_s \sigma_{12} N_1 P_{ASEF} + \Gamma_s \sigma_{21} N_2 P_{ASEF} - \alpha P_{ASEF} + ASETerm(\lambda_{ASEF})\frac{N_2}{N_1} \tag{4.12}$$

$$\frac{dp_{ASEB}}{dz} = -\Gamma_s \sigma_{12} N_1 P_{ASEB} + \Gamma_s \sigma_{21} N_2 P_{ASEB} - \alpha P_{ASEB} + ASETerm(\lambda_{ASEB})\frac{N_2}{N_1} \tag{4.13}$$

overlap integrals between pump radiation and active ion distribution is Γ_p and overlap integrals between signal light, and active-ion distribution is Γ_s .

$$\Gamma_{p(s)} = \int_0^{2\pi} \int_b^2 i_{p(s)} r(r,\phi) r \frac{dr}{d\phi} \tag{4.14}$$

$$i_{p(s)} = \frac{I_{p(s)}(r,\phi,z)}{P_{p(s)}(z)} \tag{4.15}$$

In the above equation, 4.15 $I_p$is the intensity of the pump beam. Frequency for this laser pump $v_p = \frac{c}{\lambda_p}$. The intensity I_s of the transverse field corresponds to the magnitude of the Poynting vector of the fundamental mode of the fiber at wavelength λs . optical power along z will be:

$$P_s(z) = \int_0^{2\pi} \int_b^{\alpha} I_s(r,\phi,z) r \frac{dr}{d\phi} \tag{4.16}$$

The Dy-doped fiber commonly referenced in most research papers on yellow fiber lasers is manufactured by Le Verre Fluoré [111]. which was founded in 1977 in France, the leading manufacturer of fluoride and germanate optical fiber.

4.5.3 Dy- doped fiber laser model Analysis

We have chosen the FDTD method for developing and analyzing the Laser model. The rate and propagation equations (1) to (12) can be expressed in this section for dysprosium-doped fiber.

$$\frac{\partial N_2(z,t)}{\partial t} = \sum_{k=1}^{k} \frac{\Gamma_k \lambda_k}{h \nu_k A_k} \left[\sigma_{12}(\lambda_k) N_1 - \sigma_{21}(\lambda_k) N_2\right] \left[P_k^+(z,t) + P_k^-(z,t)\right] - \frac{N_2(z,t)}{\tau}[111] \tag{4.17}$$

$$N_t = N_0 + N_1 + N_2 + N_3[111] \tag{4.18}$$

$$\pm \frac{\partial P_p^{\pm}(z,t)}{\partial z} + \frac{1}{v_p} \frac{\partial P_p^{\pm}(z,t)}{\partial t} = -\Gamma_p \left[\sigma^{30}(\lambda_p) N^3 - \sigma^{03}(\lambda_p) N^0\right] P_p^{\pm}(z,t)[111] \tag{4.19}$$

$$-\alpha_p(\lambda_p) P_p^{\pm}(z,t)$$

$$\pm \frac{\partial P_k^{\pm}(z,t)}{\partial z} + \frac{1}{v_p} \frac{\partial P_k^{\pm}(z,t)}{\partial t} = \Gamma_k \left[\sigma_{21}(\lambda_k) N_2 - \sigma_{12}(\lambda_k) N_1\right] P_k^{\pm}(z,t) - \alpha_a(\lambda_k) P_k^{\pm}(z,t)[111] \tag{4.20}$$

$$+ \left(2\sigma_{21}(\lambda_k) N_2 \frac{hc^2}{\lambda_k^3} \Delta\lambda_k\right)$$

The dysprosium dopant concentration is N_1 and is uniformly distributed in the fiber. The ground and stimulated populations are N_0 and N_3. N_1 and N_2 . This represents the lower and upper lasing level populations, respectively. P_P is the pump power and P_k indicates the Amplified spontaneous emission power for the forward signal. P_k can be referred to as the lasing or signal power. ASE can be regarded as a weak background noise. The group velocities of the pump and ASE in the fiber are

denoted as ν_p and ν_k, respectively. In this Dy-doped fiber system, the effect of chromatic dispersion can be disregarded. Hence, ν is independent of wavelength. Here, σ_{03} and σ_{21} represents the pump absorption and yellow signal emission cross sections of dysprosium ions, respectively. A is the doped area of the Dy-doped fiber, and Γ_p (Γ_k) is the overlapping factor between the pump (ASE) field and the fiber-doped area. The initial boundary conditions on the propagating waves associated with the above partial differential equations (PDEs) are written as:

$$P_p^+(0,t) = P_p^+(t)$$

$$P_p^-(L,t) = P_p^-(t)$$

$$P_k^+(0,t) = P_s^+(t), \quad k = s \tag{4.21}$$

$$P_k^+(0,t) = 0, \quad k \neq s$$

$$P_k^-(L,t) = 0, \quad k \neq s$$

In the equation above, $P_p^+(t)$ and $P_p^-(t)$ are forward and backward power. ASE forward and backward powers at the beginning and end of the fiber are zero. $P_k^+(0,t)$, $P_k^-(L,t)$.

4.6 Validation of the Forward-Time Centered-Space approach

For our experiment, we made some analysis with a MATLAB toolbox that is specially designed for Er and Yb doped fiber amplifiers and laser. Forward-Time Centered-Space (FTSC) explicit method is chosen for our numerical experiments. To be more confirmed about the accuracy of the selected model some numerical analysis has been performed for Er doped fiber amplifier. Then this model was modified for our desired four-level system for dy-doped fiber amplifier system [109].

4.6.1 Er-doped fiber amplifier analysis by FTCS method

In fiber optic networks, Erbium-doped fiber amplifiers (EDFAs) are widely used to amplify signal in the long-wavelength range near 1550 nm. It is suitable for long-distance systems utilizing fibers with losses of less than 0.2 dB/km. The most common EDFA arrangement in real-world applications is the forward pumping structure containing a 980 nm pump. This framework is chosen due to its efficient utilization. economical, steady, and fiber amplifiers with low power consumption. An Er-doped fiber amplifier with physical parameters comparable to the one considered in [109], is studied. Energy levels of the Er-doped system, there are three energy levels: the ${}^4I_{15/2}$,${}^4I_{13/2}$, and ${}^4I_{11/2}$ representing respectively the ground state, the upper state, and the metastable state.

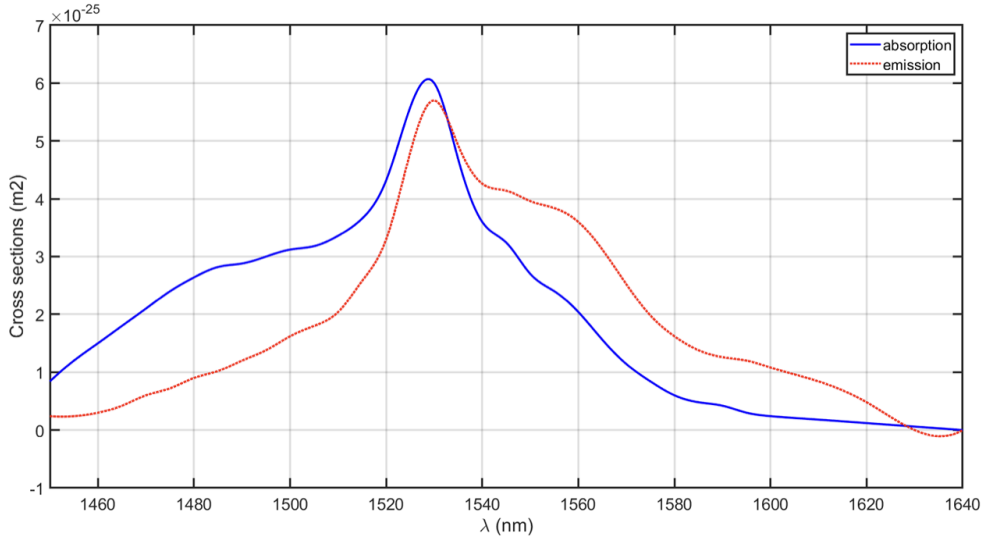

Figure 4.5: Cross-section spectra of an erbium-doped fiber amplifier (absorption and emission).

The populations of the different levels are denoted as N_1, N_2, and N_3. A population inversion is required between levels 1 and 2 to achieve amplification. Since state 1 is the ground state, at least half of the total population of erbium ions needs to

be excited to level 2 to have population inversion. In this observed EDFA, the pump wavelength is considered 980 nm, which excites the ions to the upper level ${}^4I_{11/2}$. The upper-level lifetime is nearly $1\,\mu s$. By non-radiative transition, ions rapidly decay to the metastable state ${}^4I_{13/2}$ due to heat release. The time constant for the metastable energy state is $10\,ms$. The fiber features a core radius of $1.4\,\mu m$ and exhibits a refractive index difference of 0.026 between the core and the cladding. The overlap integral, which measures the interaction between mode intensity and erbium distribution, is $\Gamma = 0.40$ at $1550\,nm$ and $\Gamma = 0.64$ at $980\,nm$. Additionally, this fiber has an Er^{3+} concentration of $N_t = 0.7 \times 10^{19}\,\mathrm{cm}^{-3}$ [119, 120, 111]. This EDFA model was selected due to prior experimental and theoretical evaluations [120, 111]. The absorption and emission cross-section spectra for the EDFA are presented in the figure above. It is shown that for erbium, the emission cross-section exceeds the absorption cross-section within the wavelength range of $1540 - 1620\,nm$, while at the pump wavelength of $980\,nm$, the emission cross-section is zero. Varying pump input powers stimulate the population inversion of the upper state in the Er-doped fiber amplifier. When the pump input power decreases, the FTCS method demonstrates similar behavior of population inversion. To verify this method, some other parameters have been calculated, such as signal gain and ASE. The results are compared to other methods for further confirmation [111].

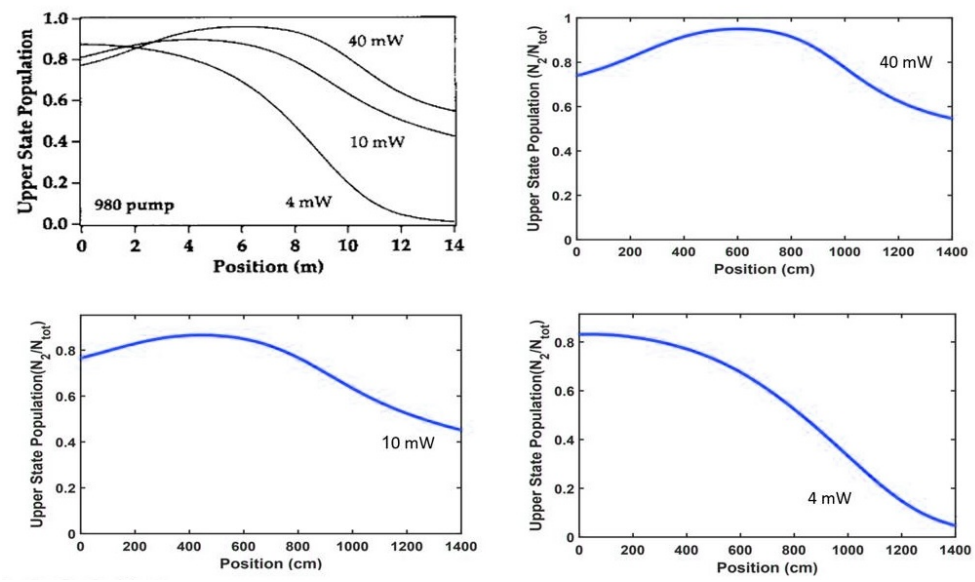

Figure 4.6: Er-doped fiber amplifier, pumped at 980 nm for various pump powers, upper state population along the fiber length (14 meters). For pump power of 40 mW, 10 mW, and 4 mW (Blue lines) respectively. This graph was adapted from [111].

The figure 4.5 represents the absorption emission cross section for an Er-doped fiber amplifier. This has been observed, from approximate wavelength 1540 nm to 1630 nm range, the emission cross-section is higher compared to the absorption cross-section. In the figure 4.6 obtained from [111] demonstrated the depletion behavior of population inversion to the fiber length change while pump power decreases. For pump power of 40 mW, the population inversion reaches a peak in 6 to 8 m fiber length. for the low pump power 4mW, upper state population inversion is very low. Another crucial parameter ASE of erbium doped fiber amplifier is considered to verify the model of EDFA. In the wavelength range for emission cross section from 1450 nm to 1600 nm, forward and backward ASE power is calculated. From figure 4.7 it is demonstrated that the predicted numerical results from the pro-

posed FTCS method show a good agreement in [111]. The backward ASE becomes stronger while it travels through the fiber since flows across a high population inversion region. However, forward ASE moves through a region where the inversion of population decreases gradually. This results in less amplification in fiber. Forward ASE increases deliberately in associated to backward ASE [119, 111].

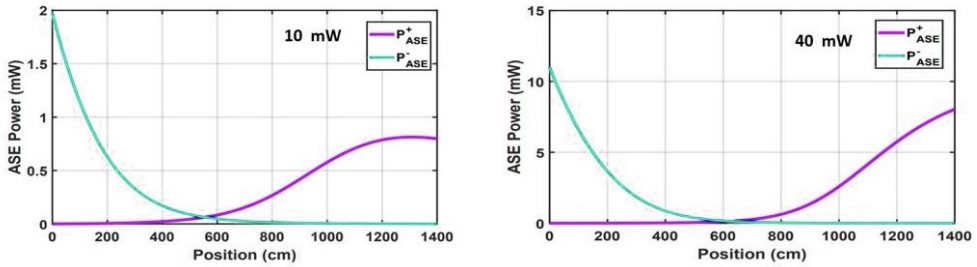

Figure 4.7: Forward and backward ASE power as a function of fiber length 14 m. EDFA pump wavelength 980 nm. For different pump input power: 10 mW (left) and 40 mW (right)[111] .

4.7 Theoretical Analysis of Dy^{3+}-doped ZBLAN Visible Fiber Lasers

In this section after FTCS method verification, this model is used for dysprosium doped fiber laser analysis. To explain the energy levels of dy- doped a simplified energy level diagram is demonstrated figure below. The transition from $^4F_{9/2}$ to $^6H_{13/2}$ level generates yellow emission (573 nm). In the ZBLAN lower level ($^6H_{13/2}$) lifetime is 0.65 ms. This lifetime is comparable to the energy level $^4F_{9/2}$, which is around 1.5 ms. The yellow emission light is also re-absorbed. population accumulation in lower laser level causes the reabsorption of yellow emission.

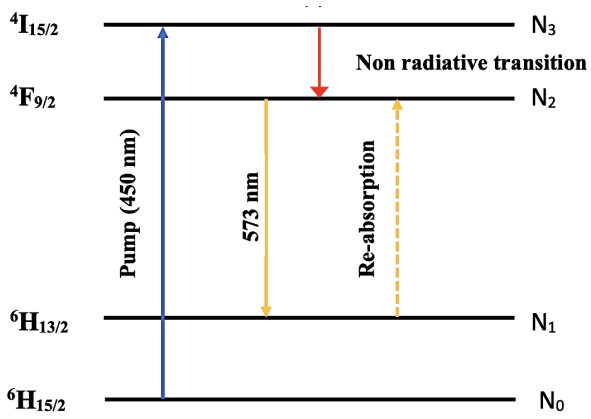

Figure 4.8: Energy level diagram of dy doped fiber laser. the lifetime of the lower laser level $^6H_13/2$ of the yellow transition is comparable to the upper laser level $^4F_{9/2}$ in ZBLAN fiber. Yellow light reabsorption is demonstrated by the yellow dash upward lines.

4.7.1 Dy-doped fiber laser parameters

The dysprosium-doped fiber laser we considered for our analysis is a similar fiber laser fabricated by Le Verre Fluor. (France) [110]. To begin with, the absorption and emission cross-section is demonstrated by the extraction of the experimental data from [107, 110]. The numerical analysis parameters used in the experiments are listed

below. Structural parameters of the investigated Dy-doped ZBLAN fiber laser are listed in Tables 4.3 and 4.4 .

Parameter	Value
λ_{pump}	450 nm
λ_{pump}	573 nm
$\sigma_{ab(p)}$, Pump absorption cross section	$0.64 * 10^{-25} m^2$
$\sigma_{em(p)}$, Pump absorption cross section	0
$\sigma_{ab(p)}$	$0.1 * 10^{-25} m^2$
$\sigma_{em(p)}$	$0.9 * 10^{-25} m^2$
Γ_p, pump overlap factor	0.70
Γ_s, signal overlap factor	0.65
τ_{32}	$100 \mu s$
τ_{10}	$650 \mu s$
τ_{21}	$1.5 ms$
τ_{30}	$1 * 10^{-2} m^{-3}$

Table 4.3: Parameters of dy-doped fiber laser for simulation

Fiber parameter	Value
n_{core}	1.48
n_{clad}	1.47
Numerical aperture	0.16
d_{core}	12.5 μm
Doping concentration	$3.66 * 10^{25} m^{-3}$
Fiber backgroundless	0.18 dB/m
Length	4 meters

Table 4.4: Physical parameters for fiber design.

The absorption, and emission cross-section is calculated from [110] in the wavelength range of 550nm to 600 nm. This fiber is pumped by a GaN laser diode with

emission at 447 nm wavelength.

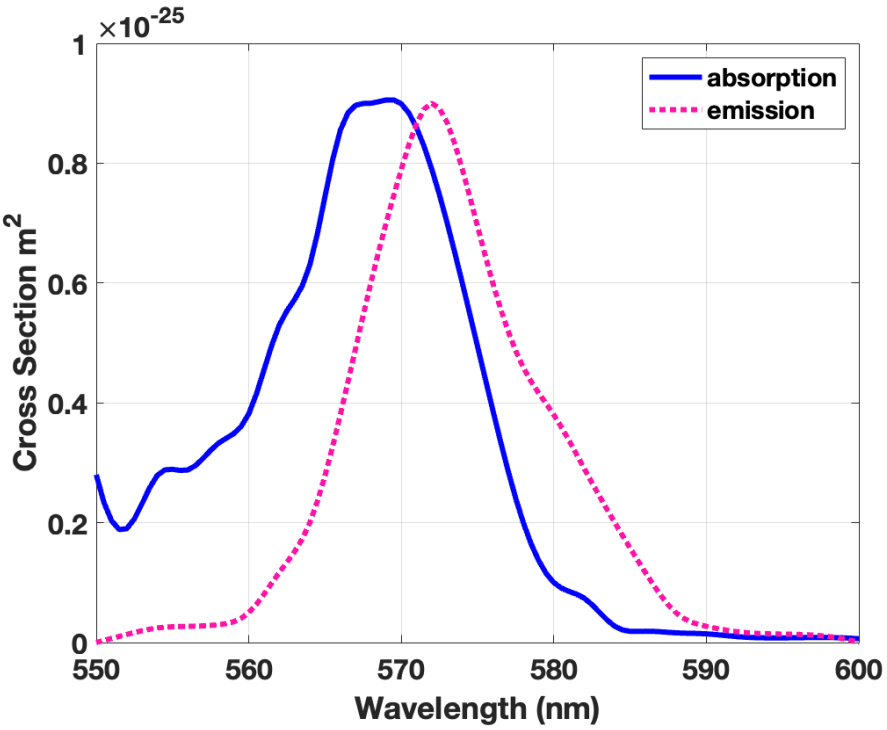

Figure 4.9: Emission and re-absorption cross-sections of two different energy levels, ${}^4F_{9/2}$ to ${}^6H_{13}/2$, in the Dy^{3+} ion, estimated from the established numerical method [106].

From the table of physical and structural parameters of Dy-doped ZBLAN fiber, it is denoted that the absorption cross-section is σ_{abp} for the pump wavelength λ_p. The reabsorption and emission cross-sections are respectively σ_{abs} and σ_{ems} at the signal wavelength λ_s. The Dy-doped fiber laser energy level lifetimes are τ_{32}, τ_{21}, τ_{30}, and τ_{10}. The reflectivities of the input and output mirrors are denoted as R_1, R_2, R_3, and R_4. The input mirror has reflectivity R_1 and the output mirror has reflectivity R_2 at the signal or laser wavelength. Both mirrors are considered to be transparent at the pump wavelength ($R_3 = R_4 = 0$) so that the pump can pass through the fiber once

[111]. The values are $R_1 = 90\%$, $R_2 = 50\%$, $R_3 = 0$, and $R_4 = 0$.

4.7.2 Dy-doped fiber laser normalized population inversion

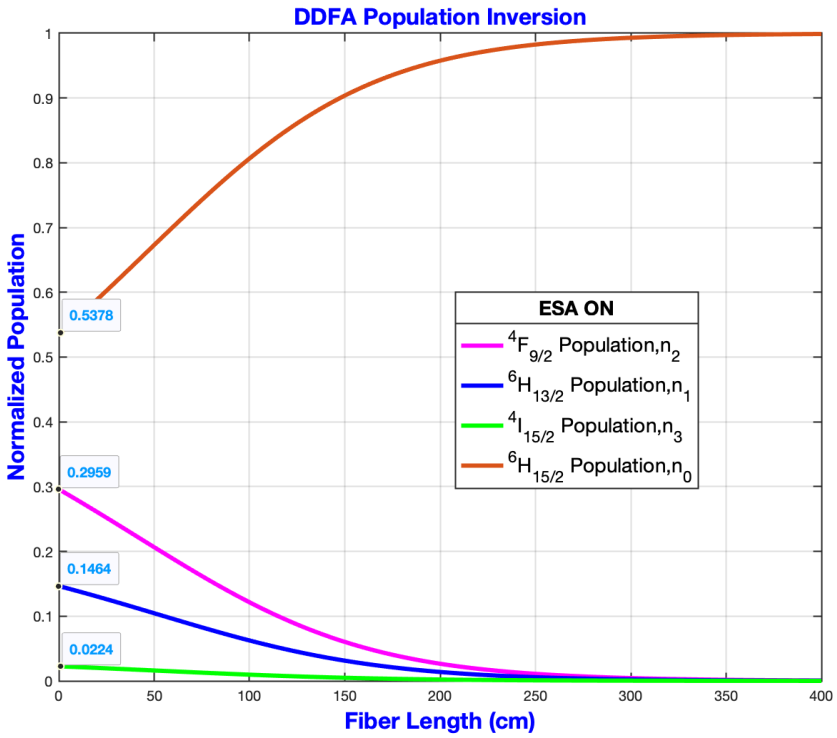

Figure 4.10: Normalized population distribution of different energy levels along 4m dy- doped fiber for ESA ON, P_s is 100 mW .

The numerical analysis is performed by the FTCS method on the Dy-doped rate equations explained in the previous section 4.5.1. The normalized population distributions $N_t = N_0 + N_1 + N_2 + N_3$ for the yellow laser levels have been calculated by the FTCS method as a function of fiber length [111]. For this simulation, we have considered the signal input power of 100 mW and for another simulation signal input power of

150 mWand for both of the simulation the pump input power of 450 mW is considered. When considering the ESA, the normalized population of the $^4F_{9/2}$ level is marginally higher compared to the ESA-off state or when the ESA is ignored during the simulation. This is demonstrated in 4.10 and 4.11

Additionally, if we consider all other energy levels, $^6H_{13/2}$, $^4I_{15/2}$, and $^6H_{15/2}$, when the ESA is ignored, the population increases. The population of $^4I_{15/2}$ is very minor due to the non-radiative transition from the level $^4F_{9/2}$.

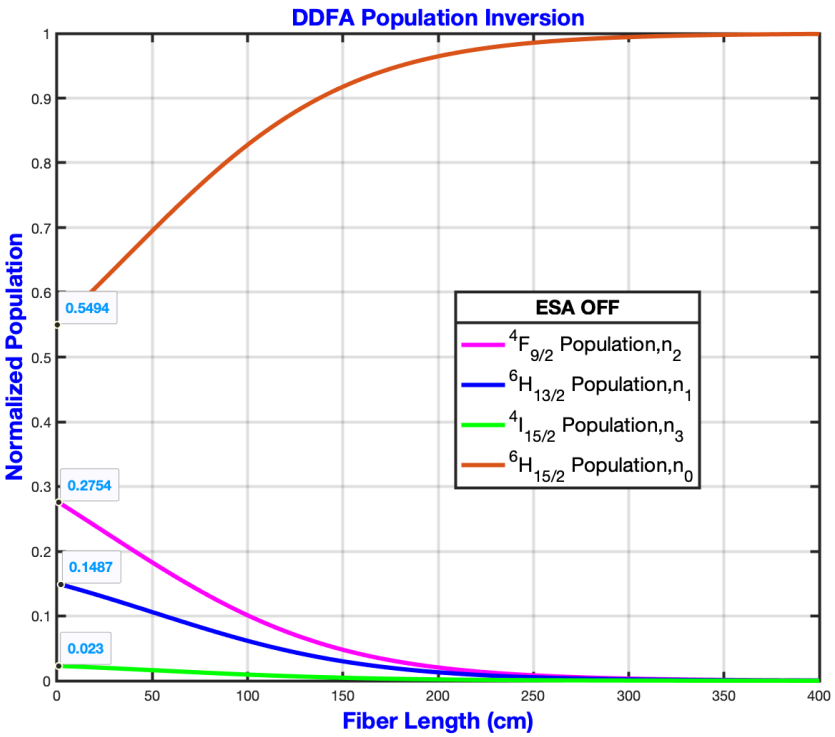

Figure 4.11: Normalized population distribution of different energy levels along 4m dy- doped fiber for ESA OFF, P_s is 100mW .

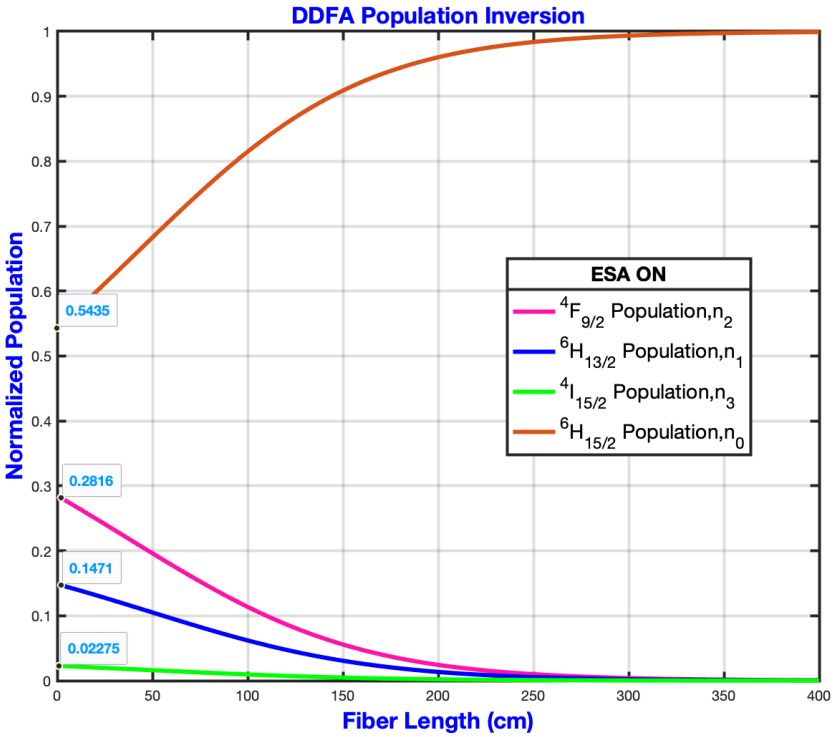

Figure 4.12: Normalized population distribution of different energy levels along 4m dy- doped fiber for ESA ON, P_s is 150mW .

In figure 4.12 and 4.13 the signal input power is increased to 150 mW for Excited state absorption ON or OFF. Again Pump input power is 450 mW For both of the simulations, the population in energy levels is slightly higher compared to the previous signal power of 100 mW. It is noticeable that when ESA is considered the normalized population is significantly higher than ESA OFF state. The population distribution is very negligible for $^4I_{15/2}$ in both situations.

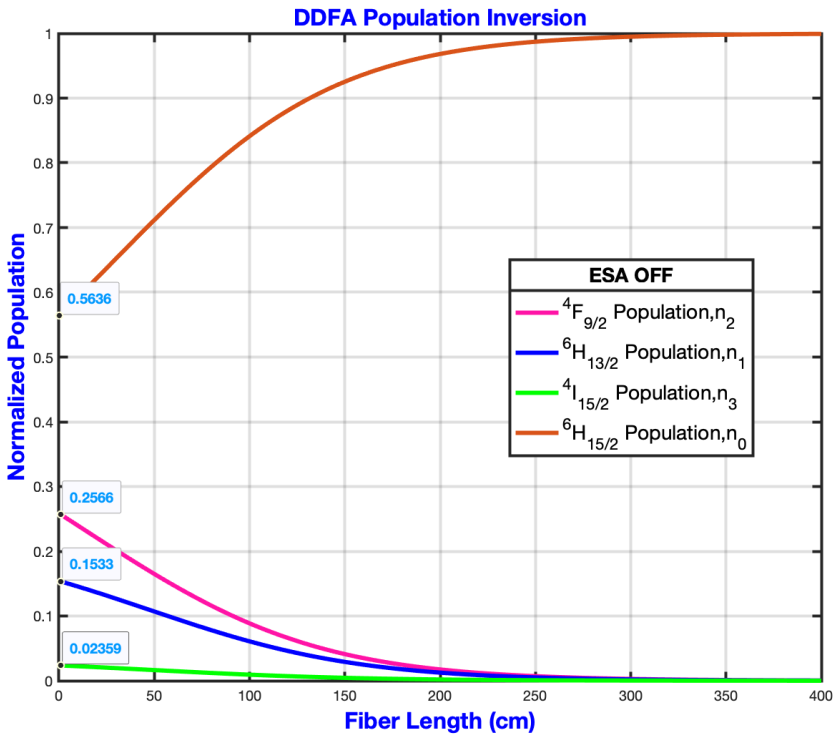

Figure 4.13: Normalized population distribution of different energy levels along 4m dy- doped fiber for ESA OFF, P_s is 150mW .

4.7.3 Effect ESA of power evaluation in Dy-doped fiber laser

In this section we have evaluated the ESA effect for input signal power and input pump power. During this analysis, the pump and signal power along fiber length during ESA ON and OFF is considered. When ESA is accounted signal output power is 147 mW for input signal power 100mW (Figure 4.14). By ignoring ESA, higher output signal power is achieved around 178mW (Figure 4.15). Pump power, for both our numerical simulation is 450mW. Again, the amplification of the signal output power is observed when the signal input power is 150 mW to investigate the effect of ESA during the amplification of the Laser. These results are obtained in (Figure 4.16) and (Figure 4.17).

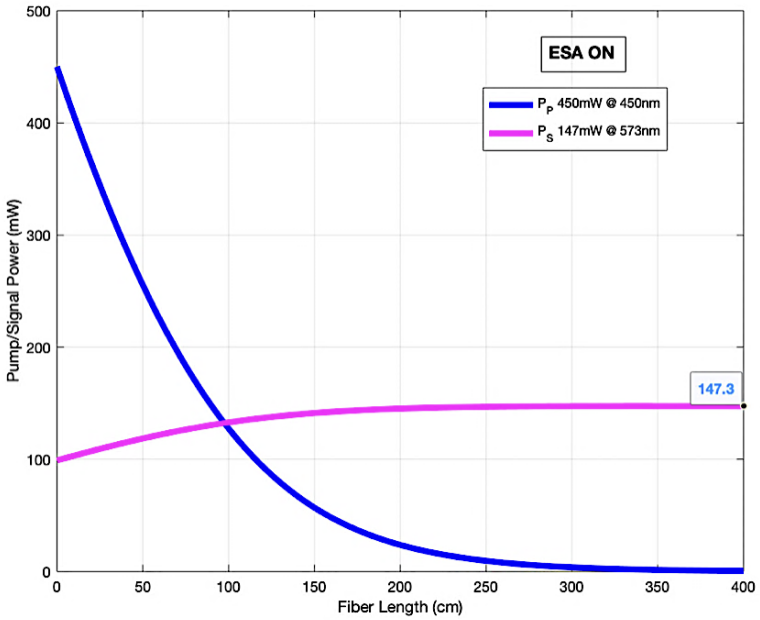

Figure 4.14: Signal power and pump power changes along 4-meter dy doped fiber laser. As an input power 100mW and pump power of 450 mW. For ESA ON.

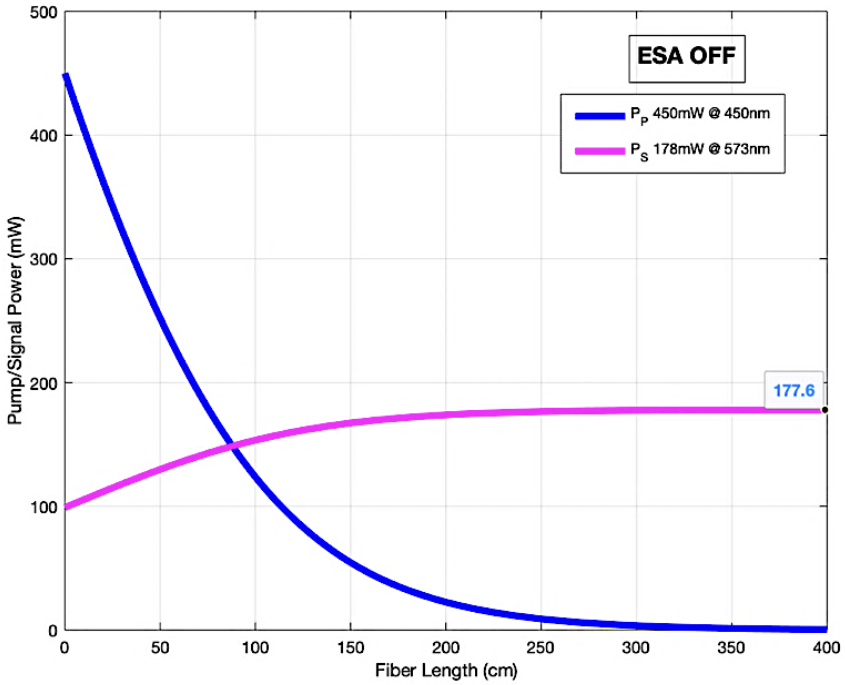

Figure 4.15: Signal power and pump power changes along 4-meter dy-doped fiber laser. As an input power of 100mW and pump power of 450 mW. For ESA OFF.

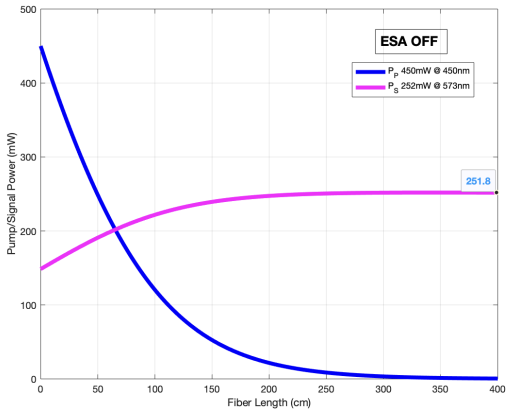

Figure 4.16: Signal and Pump power and Fiber length changes for ESA OFF, P_s is 150 mW .

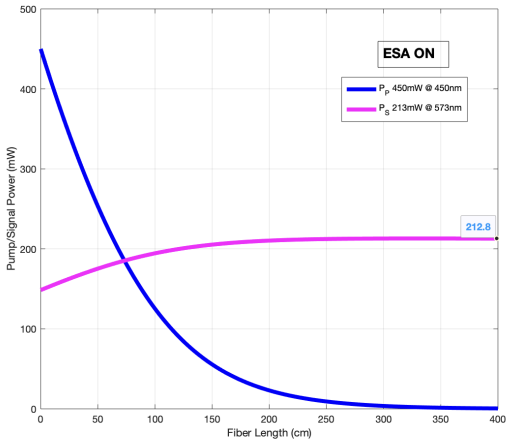

Figure 4.17: Signal power and Fiber length changes for ESA ON, P_s is 150 mW .

The output power (213 mW) (Figure 4.17) is also slightly higher when ESA is considered for input signal power 150 mW. ESA occurs because ion in the long-lived energy level is transferred to higher energy level. While,ignoring ESA output power

is approximately 250mW (Figure 4.16). Which is considered as a significantly higher value compared to the output power during 100 mW input signal power.

To analyze the output power of Dy- doped fiber laser as a function of input signal power, signal power is varied from 70 mW to 130 mW. The Pump power 450 mW is considered for our simulation. The output power has significantly increased while ESA is ignored. For the same input signal power, the output power impressively changes. For instance, 70 mW input signal power output power is 106 mW (Figure 4.18). and 130 mW (Figure 4.19) for ESA ON and ESA OFF respectively. So, it has been illustrated by comparing the output power while ignoring the effect of ESA according to higher signal input power a significantly higher output power is achieved,

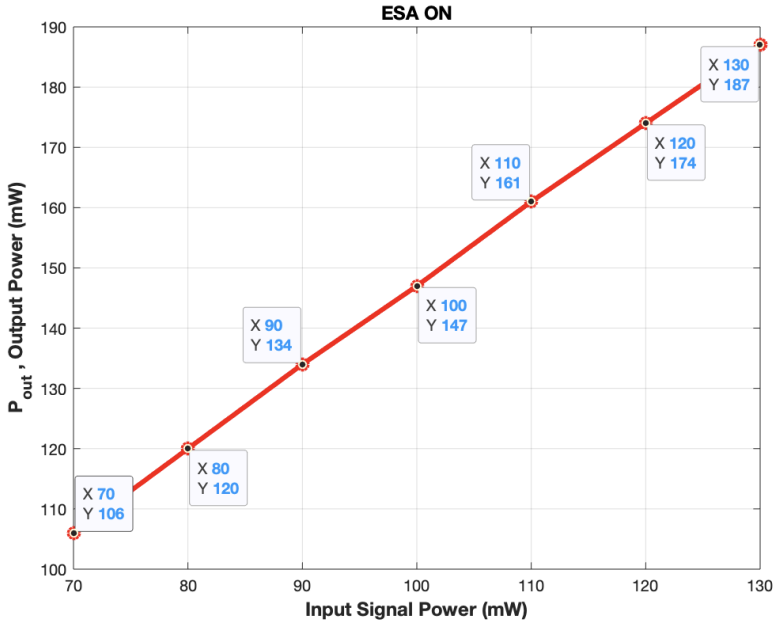

Figure 4.18: Output power of the Dy-doped fiber as a function of the input signal power (ESA ON)

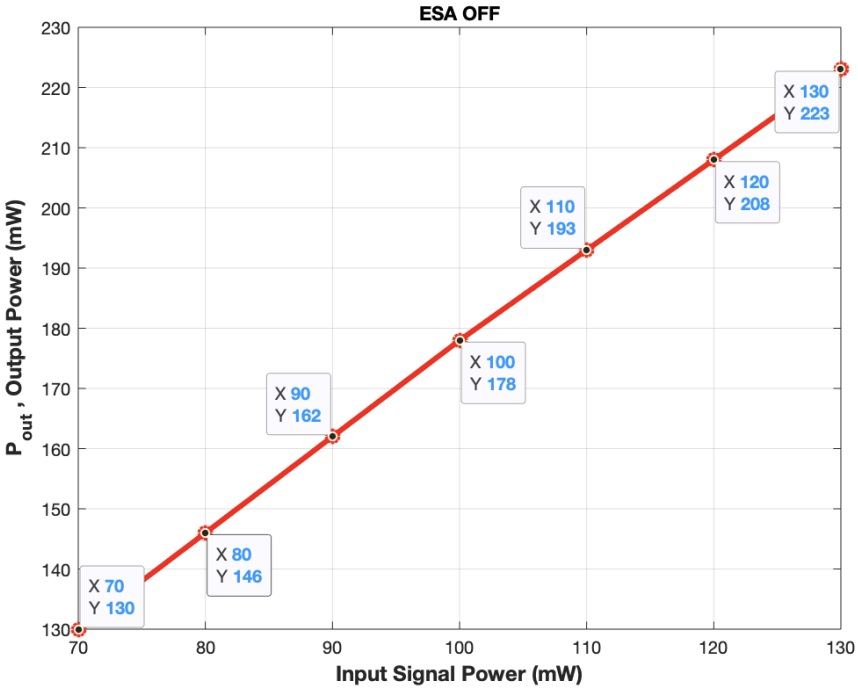

Figure 4.19: Output power of the Dy-doped fiber as a function of the input signal power (ESA OFF)

Again, we considered the signal input power fixed at 100 mW and varied the pump input power from 200 mW to 500 mW. For ignoring ESA effect, output power increases. It is because there is no loss accounted in the analysis.

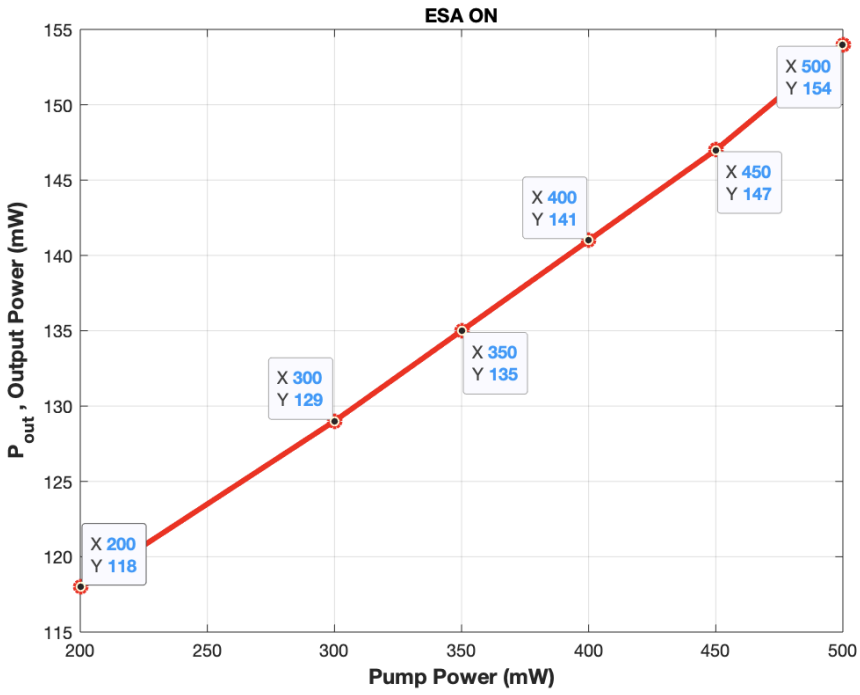

Figure 4.20: Output power of the Dy-doped fiber as a function of the pump power (ESA ON)

(Figure 4.20) illustrate the evaluation of output power of Dy- doped fiber laser as a function of pump power. here, we did the simulation for multiple pump power ranging from 200 mW to 500mW, considering ESA. As the input pump power is goes higher, the output power also rise significantly.

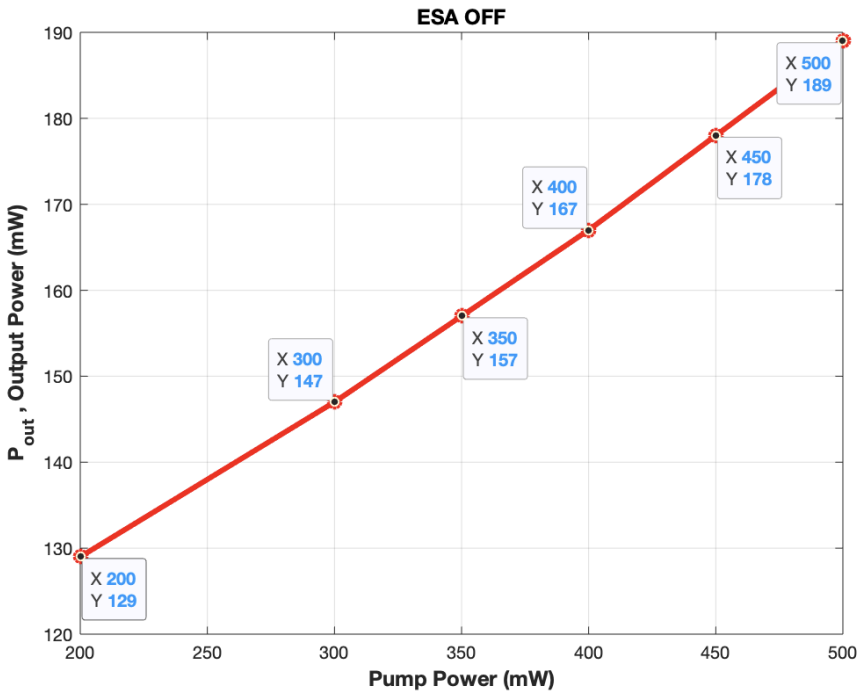

Figure 4.21: Output power of the Dy-doped fiber as a function of the pump power (ESA OFF)

We further analyzed the output power as a function of pump power (ESA OFF) in (Figure 4.21). The output powers for different pump power is reported while ESA is ignored. since we are not considering the any losses, a significant changes to the output power is noticeable.

4.7.4 Amplified Spontaneous Emission power evolution

We analyzed the amplified spontaneous emission (ASE) both in forward and backward directions Figure (4.22) and (4.23). This parameter has been calculated in the presence and absence of ESA in the emission wavelength spectrum from 550nm to 600 nm [111]. From the demonstrated graph it can be remarked that, on ASE power,

excited state absorption have shown their significant effects. when we consider ESA, energy level ${}^4F_{9/2}$ population rises. If we consider little higher input signal power, ESA effect will be prominent and ASE power will drop. We tried to compare the ASE power along different fiber length such as 1m, 2m and 3 meters for both forward and backward ASE.

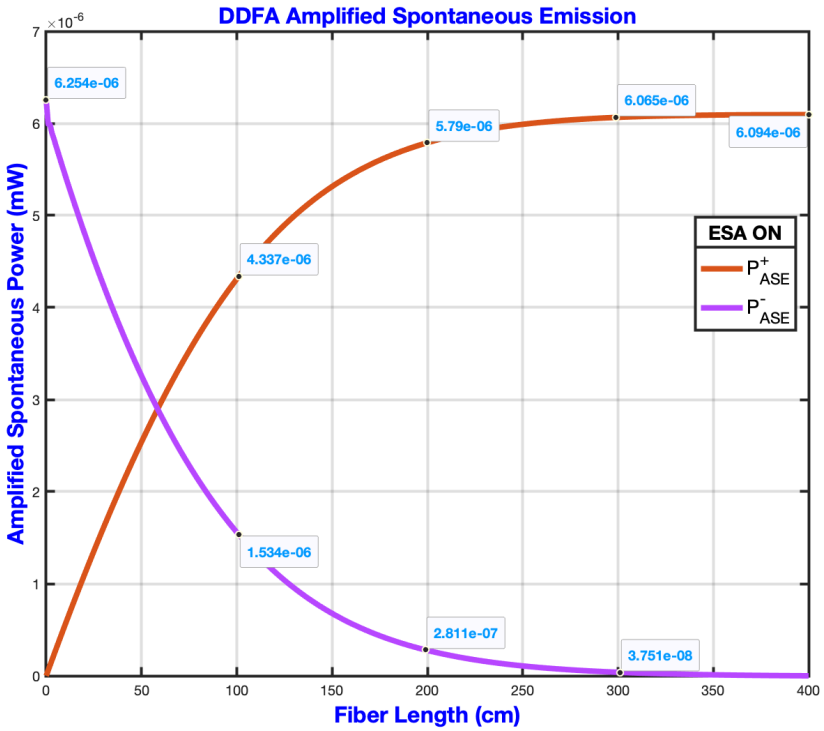

Figure 4.22: Forward and backward Amplified Spontaneous Emission power evolution along the Dy-doped fiber. Input power 100mW for both ESA ON

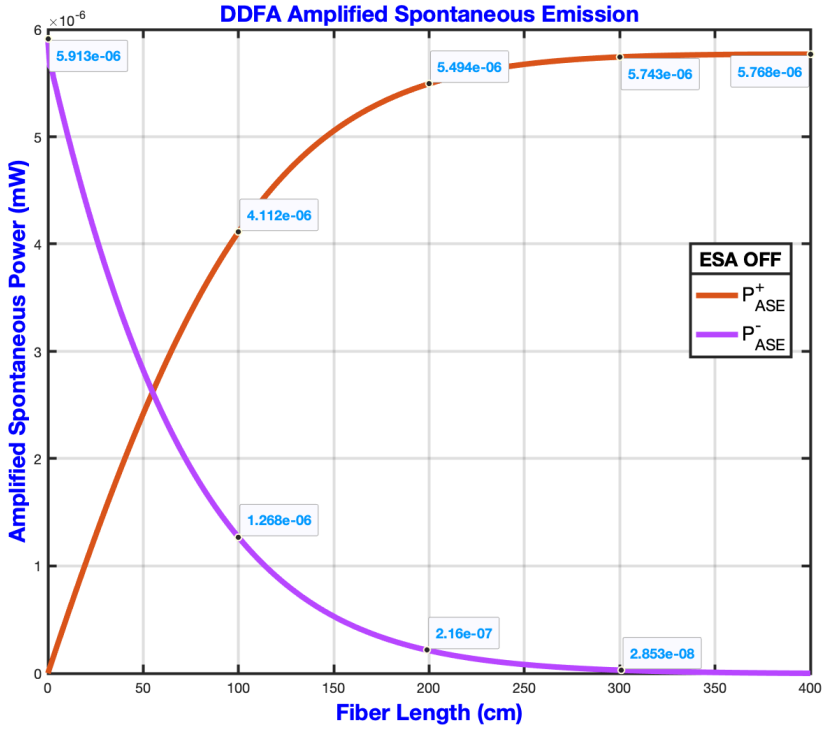

Figure 4.23: Forward and backward Amplified Spontaneous Emission power evolution along the Dy-doped fiber. Input power 100mW for ESA OFF

4.7.5 Effect of core diameter

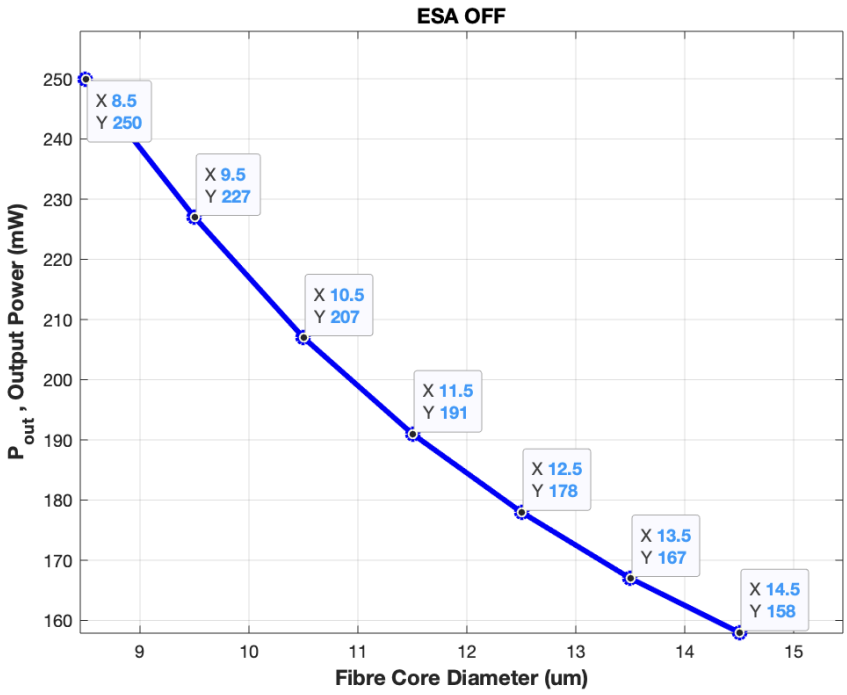

Figure 4.24: Output power of the Dy-doped fiber as a function of fiber core diameter for ESA OFF.

From the figure 4.24 and 4.25 we have analyzed the output power evaluation along with the fiber core diameter variation. It has been observed that, as we change the fiber core diameter from 8.5 micrometer to 14.5 micrometer the output power sightly decreased. But by ignoring ESA the output power changes significantly. There is no background loss considered by ignoring ESA effect. Again the effect of ESA is very prominent in this analysis. the output power drastically drop while ESA is considered compared to ESA OFF. Also, Fiber length is a key parameter. the optimal length is 4m for our experiments. But for our experiments we changed the length to observe the output power of laser. varying core diameter also plays significant role to the

output of laser. As the core diameter decrease the light is more confined inside the core and we are able to get more efficient laser output.

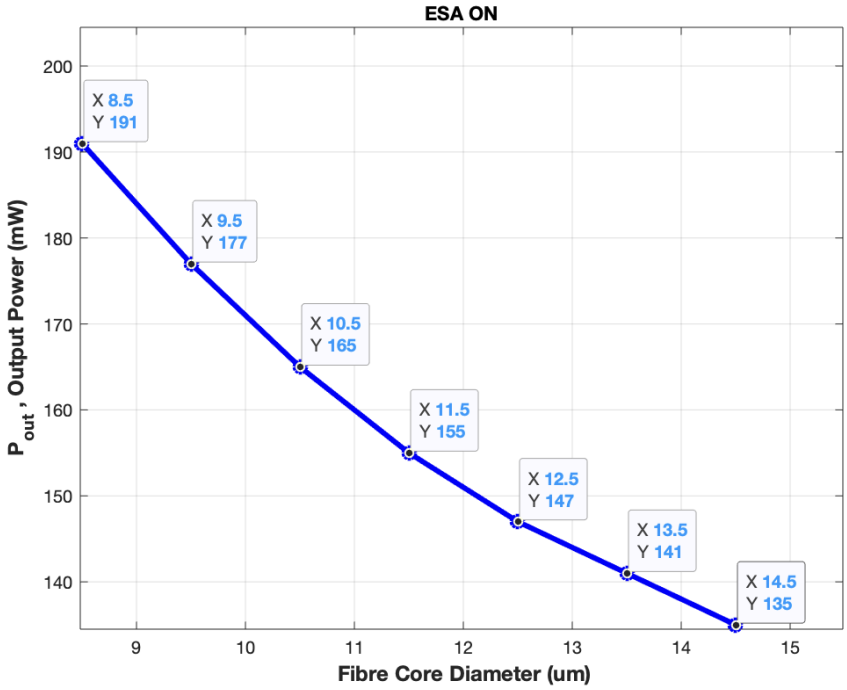

Figure 4.25: Output power of the Dy-doped fiber as a function of fiber core diameter for ESA ON.

4.7.6 Effect of lifetime

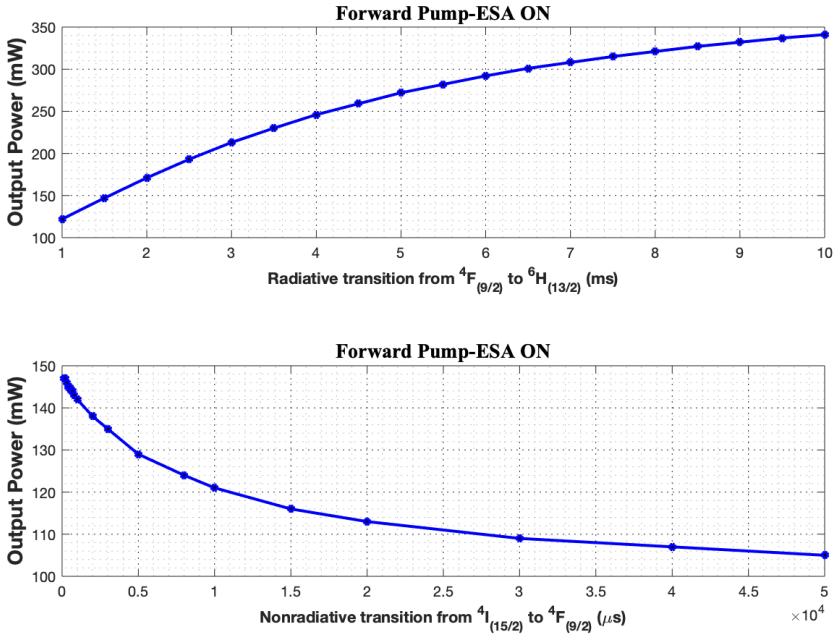

Figure 4.26: Output power of Dy-doped fiber as a function of lifetime of transition level $^4F_{9/2}$ to level $^6H_{13/2}$ and from $^4I_{15/2}$ to level $^4F_{9/2}$ respectively

Finally, For numerical analysis, we performed a simulation to analyze the effect of the lifetime of transition level $^4F_{9/2}$ to level $^6H_{13/2}$ and from $^4I_{15/2}$ to level $^4F_{9/2}$ respectively (Figure 4.26). For ESA ON, Forward pump, Length of the fiber is 4m. signal wavelength, λps = 573 nm, pump wave length, λp = 450 nm, signal power, Ps=100 mW, pump power, Pp= 450 m. Focused on the impact of the lifetimes of energy levels,Effect on output power of laser by varying the lifetime of level $^4F_{9/2}$ and $^4I_{15/2}$.

As the lifetime has been varied for level $^4F_{9/2}$ a significant change was observed in the output power of the Dy-doped fiber. Output power increases as we change the

lifetime. Increasing lifetime 3x for level $^4F_{9/2}$ output power is almost double. varying the lifetime from μs to ms for the level $^4I_{15/2}$ an exponential decay was reported. This work has demonstrated the influence of the lifetime on the output power of a Dy-doped yellow fiber laser. From this part of the experiment, it has been observed that for analyzing the fiber effect of the output power it is necessary to do more simulation by varying other parameters. The experimental data is inadequate. By decreasing tau to the value $10^{-5}\mu s$, the Excited state absorption (ESA) on the output power of laser can drastically reduce. The length of the fiber is also an important parameter.

Conclusion

In the first part of the thesis, we discussed the solar cell basics and laser scribing process for solar cells. This part aimed to apply scribing techniques in different solar cell samples. Different solar cell categories were briefly explained in chapter one of this thesis. IMEM-CNR provided different solar cells to experiment laser scribing, and the results were compared to mechanical scribing. Laser scribing was performed on three different types of solar cells. Such as: standard CIGS solar cells, then Antimony selenide solar cells, and Semitransparent solar cells. for each type of cell after the scribing process, SEM analysis was done by IMEM to observe whether TCO of cell is removed properly or not. Since the aim of our work was to remove TCO and make the electrical connection to the solar cell. And this should be done carefully in such a way that solar cell is not damaged, or any other part is not scribed. To achieve this, we had to consider many parameters for scribing technique. The experiment was done by Innolight Helios IR laser. Average power for this laser is 5W. pulse duration is 500- 800 ps, repetition rate 30-70 KHz, beam diameter 2.5-5.5 mm. for the first CIGS solar cell laser scribing speed was 1000 mm/s and 2000 mm/s. pulse frequency was chosen 25 KHz. After reporting all the electrical measurements, it was observed that all scribing traces do not show melting sign since it occurs the deterioration in cell performance. Some lines are not continuous and some of them are wider. TCO was partially removed and some places TCO was not removed at all. The cell area was reduced by 20 percents. The current dropped was also marked. In conclusion, this scribing measurement shows very positive results and confirmed that proposed LS for P3 scribing was successfully done on CuInGaSe based solar cell on glass.

Another type of cells consists multilayer CIGS. in this cell the absorber was replaced by Sb2Se3 (1.5 micron). The scribing was done at very high speed 1000 mm/s, 5000 mm/s. this speed occurs individual spots of scribing on cells. And this affects the multilayers of solar cells. By SEM analysis it has been cleared that TCO was removed, and absorber was undamaged. Therefore, the laser test shows promising results. By the EDAX results it shows that significantly TCO was removed in this type of solar cell. Thus, it can be said that higher speed can be effective for laser scribing process. From the final process after doing mechanical and laser scribing, all the electrical measurements were achieved for this type of cell. Since there was TCO presence, the sample was washed by ethanol for 3 minutes to overcome this problem. However, it reduces the V_{ocs} over 50 percent. So, this experiment is not recommended for this structure. Finally, the semitransparent cell was considered for our experiments. This structure is developed in a way that CIGS absorber can be coupled with a silicon-based cell to improve efficiency. The first step was done by scribing at speed of 1000 and 2000 mm/s. then we consider different scribing speed V= 20, 30,50,100,200,500 mm/s. from the SEM analysis was done for different speed. From SEM analysis it is observed that the effects are visible at three lowest speeds. Finally, the scribing was done at 100 mm/s, and this shows a discontinuous trace.

In this part of the thesis fiber laser for ocular disease has been analyzed. A model was developed of Dysprosium doped fiber laser and the physical and numerical parameters was analysis to observe the laser output efficiency. The rate equation and power propagation equation of the dy-doped fiber laser were implemented. Then this model was verified for other rear earth doped. Theoretical analysis of dysprosium doped ZBLAN fiber laser was performed by a MATLAB model. The optimized parameters of simulation were studied from many other researchers. Normalized population inversion for different energy level can be observed for different signal input power with ESA ON state and ESA OFF. Again, another simulation was performed for ASE effect to analyzed output power. Effect of ESA for power evaluation in dysprosium doped fiber laser showed in this part of the thesis. Finally, the simulation of the effect of lifetime of transition level on output power was observed. As a final remark, choosing optimal fiber parameters for simulation and their effects on output

power of laser is investigated. But this model requires more numerical simulation by varying other parameters to achieve the highest efficiency. During all of the simulation it is important to compare the results for both condition in presence of ESA and ignoring ESA. Nevertheless, intensive research is required for this dysprosium doped laser model. And further development is necessary to get the high output efficiency of laser.

List of Publications

[1] Wahida Chowdhury, Khozeymeh F, Federica Poli, Annamaria Cucinotta ,“Analysis of decay characteristics and radiative, non-radiative transition in a dysprosium doped fiber laser”, 3rd International Conference on Dielectric Photonic Devices and Systems Beyond Visible (D-Photon 2023),Bari,11-13July2023.

[2] Wahida Chowdhury, Foroogh Khozeymeh, Annamaria Cucinotta,” Analyzing the impact of numerical and experimental parameters on Dy-doped yellow fiber lasers for the treatment of eye diseases. , SPIE Photonics Europe 2024.

[3] F. Khozeymeh, F. Poli, W. Chowdhury and A. Cucinotta, "Analysis and Optimization of Dysprosium-Doped Yellow Fiber Lasers for Ophthalmology Applications," in IEEE Photonics Journal, vol. 16, no. 1, pp. 1-8, Feb. 2024, Art no. 1500108, doi: 10.1109/JPHOT.2023.3339595.

[4] A. Cucinotta, F. Khozeymeh, W. Chowdry, V. Serafini and G. Perrone, "Yellow Fiber Laser System for the Treatment of Ocular Diseases," 2024 24th International Conference on Transparent Optical Networks (ICTON), Bari, Italy,2024, pp. 1-1, doi: 10.1109/ICTON62926.2024.10648087.

[5] Wahida chowdhury, Foroogh Khozeymeh, Annamaria Cucinotta, Analysis and influence of signal and pump power evolution of yellow emitting Dy-doped fiber laser for advance eye treatment, ICOP, Firenze, Italy, 2024.

Bibliography

[1] Jeff Hecht. A short history of laser development. *Applied Optics*, 49(25):F99, 8 2010.

[2] Webb Colin E. and Julian D. C. Jones. *Handbook of Laser Technology and Applications: Principles*. CRC Press, 1 2004.

[3] Bahaa Saleh. *The Laser*. Springer, Cham, 1 2016.

[4] Frank S. Barnes. *Laser Theory*. IEEE Press, 1 1972.

[5] Jeff Hecht and Dick Teresi. *Laser*. Courier Corporation, 1 1998.

[6] George Basalla. *The evolution of technology*. Unknown, 1 1988.

[7] Laura D. Houk and Tatyana Humphreys. Masers to magic bullets: an updated history of lasers in dermatology. *Clinics in Dermatology*, 25(5):434–442, 9 2007.

[8] Terry D. Myers. THE FUTURE OF LASERS IN DENTISTRY. *Dental Clinics of North America*, 44(4):971–980, 10 2000.

[9] J.R. Deepak, Anirudh RP, and S. Saran Sundar. Applications of lasers in industries and laser welding: A review. *Materials Today Proceedings*, 2 2023.

[10] K. L. Chopra, P. D. Paulson, and V. Dutta. Thin-film solar cells: an overview. *Progress in Photovoltaics Research and Applications*, 12(2-3):69–92, 3 2004.

[11] Kosuke Kurokawa. *Photovoltaic energy conversion*. Unknown, 1 2003.

[12] D. M. Chapin, C. S. Fuller, and G. L. Pearson. A New Silicon p-n Junction Photocell for Converting Solar Radiation into Electrical Power. *Journal of Applied Physics*, 25(5):676–677, 5 1954.

[13] Maycock pd. top pv cell/module producers. photovoltaic news 2003; 22(2): 2.

[14] Eric Martinot, Akanksha Chaurey, Debra Lew, José Roberto Moreira, and Njeri Wamukonya. Renewable energy markets in developing countries. *Annual Review of Energy and the Environment*, 27(1):309–348, 10 2002.

[15] K. L. Chopra and S. R. Das. *Thin film solar cells*. Springer Science and Business Media, 11 2013.

[16] Shiozawa LR, Augustine F, A Sullivan, Smith MJ, and Cook WR. Research on the mechanism of the photovoltaic effect in high efficiency cds thin-film solar cells. *Aerospace Research Laboratories*, 1969.

[17] Thomas A. Ciulla, Armando G. Amador, and Bernard Zinman. Diabetic retinopathy and diabetic macular edema. *Diabetes Care*, 26(9):2653–2664, 9 2003.

[18] Miho Nozaki, Ryota Ando, Toshiya Kimura, Fusae Kato, and Tsutomu Yasukawa. The role of laser photocoagulation in Treating diabetic macular edema in the era of intravitreal drug Administration: A Descriptive review. *Medicina*, 59(7):1319, 7 2023.

[19] Marcus Kernt, Raoul Cheuteu, Efstathios Vounotrypidis, Christos Haritoglou, Anselm Kampik, Michael W. Ulbig, and Aljoscha S. Neubauer. Focal and panretinal photocoagulation with a navigated laser (NAVILAS®). *Acta Ophthalmologica*, 89(8):e662–e664, 10 2010.

[20] Mark S. Blumenkranz, Dimitri Yellachich, Dan E. Andersen, Michael W. Wiltberger, David Mordaunt, George R. Marcellino, and Daniel Palanker. SEMI-

AUTOMATED PATTERNED SCANNING LASER FOR RETINAL PHOTOCOAGULATION. *Retina*, 26(3):370–376, 2 2006.

[21] Kishiko Ohkoshi and Tatsuo Yamaguchi. Subthreshold micropulse diode laser photocoagulation for diabetic macular edema in Japanese patients. *American Journal of Ophthalmology*, 149(1):133–139.e1, 10 2009.

[22] Siyun Lee and Joonhyung Kim. Rhegmatogenous Retinal Detachment with Giant Retinal Tear: Case Series and Literature Review. *Journal of Clinical Medicine*, 13(16):4690, 8 2024.

[23] Bryan Chin Hou Ang, Sheng Yang Lim, Bjorn Kaijun Betzler, Hon Jen Wong, Michael W. Stewart, and Syril Dorairaj. Recent Advancements in Glaucoma Surgery—A review. *Bioengineering*, 10(9):1096, 9 2023.

[24] Ridia Lim. The surgical management of glaucoma: A review. *Clinical and Experimental Ophthalmology*, 50(2):213–231, 1 2022.

[25] Ruchi Shah, Cynthia Amador, Kati Tormanen, Sean Ghiam, Mehrnoosh Saghizadeh, Vaithi Arumugaswami, Ashok Kumar, Andrei A. Kramerov, and Alexander V. Ljubimov. Systemic diseases and the cornea. *Experimental Eye Research*, 204:108455, 1 2021.

[26] Alice Y. Zhang, Dipen Kumar, and Koushik Tripathy. Laser principles in ophthalmology, 8 2023.

[27] Pabitra K. Nayak, Suhas Mahesh, Henry J. Snaith, and David Cahen. Photovoltaic solar cell technologies: analysing the state of the art. *Nature Reviews Materials*, 4(4):269–285, 3 2019.

[28] Athil S. Al-Ezzi and Mohamed Nainar M. Ansari. Photovoltaic solar cells: a review. *Applied System Innovation*, 5(4):67, 7 2022.

[29] Askari Mohammad Bagher. Types of solar cells and application. *American Journal of Optics and Photonics*, 3(5):94, 1 2015.

[30] Alan L. Fahrenbruch, Richard H. Bube, and Robert V. D'Aiello. Fundamentals of Solar cells (Photovoltaic Solar Energy Conversion). *Journal of Solar Energy Engineering*, 106(4):497–498, 11 1984.

[31] Muhammad Aamir Iqbal, Maria Malik, Wajeehah Shahid, Syed Zaheer Ud Din, Nadia Anwar, Mujtaba Ikram, and Faryal Idrees. Materials for photovoltaics: overview, generations, recent advancements and future prospects. *Thin Films Photovoltaics*, 2022.

[32] Lewis Fraas and Larry Partain. *Solar Cells: A Brief History and Introduction*, chapter 1, pages 1–15. John Wiley and Sons, Ltd, 2010.

[33] José Luceño-Sánchez, Ana Díez-Pascual, and Rafael Peña Capilla. Materials for photovoltaics: state of art and recent developments. *International Journal of Molecular Sciences*, 20(4):976, 2 2019.

[34] Ryan P. Smith, Angela An-Chi Hwang, Tobias Beetz, and Erik Helgren. Introduction to semiconductor processing: Fabrication and characterization of p-n junction silicon solar cells. *American Journal of Physics*, 86(10):740–746, 9 2018.

[35] Donald A. Neamen. *Semiconductor Physics and Devices*. McGraw-Hill Education, 1 2011.

[36] Ewa Radziemska. Thermal performance of Si and GaAs based solar cells and modules: a review. *Progress in Energy and Combustion Science*, 29(5):407–424, 1 2003.

[37] Chaomin Zhang. *High Efficiency GaAs-based Solar Cells Simulation and Fabrication*. Arizona State University, 2014.

[38] Arno Smets, Klaus Jäger, Olindo Isabella, René Van Swaaij, and Miro Zeman. *Solar energy*. Bloomsbury Publishing, 1 2016.

[39] Feng Wang, Xiao-Ke Liu, and Feng Gao. *Fundamentals of solar cells and Light-Emitting diodes*. Elsevier eBooks, 1 2019.

[40] Marius Grundmann. *The Physics of semiconductors*. Springer Science and Business Media, 11 2006.

[41] C. P. Please. An analysis of semiconductor P-N junctions. *IMA Journal of Applied Mathematics*, 28(3):301–318, 1 1982.

[42] Ben G. Streetman. *Semiconductors and transistors*. Elsevier eBooks, 1 2002.

[43] T. Ibn-Mohammed, S.C.L. Koh, I.M. Reaney, A. Acquaye, G. Schileo, K.B. Mustapha, and R. Greenough. Perovskite solar cells: An integrated hybrid lifecycle assessment and review in comparison with other photovoltaic technologies. *Renewable and Sustainable Energy Reviews*, 80:1321–1344, 6 2017.

[44] Mehreen Gul, Yash Kotak, and Tariq Muneer. Review on recent trend of solar photovoltaic technology. *Energy Exploration and Exploitation*, 34(4):485–526, 5 2016.

[45] A. V. Shah, H. Schade, M. Vanecek, J. Meier, E. Vallat-Sauvain, N. Wyrsch, U. Kroll, C. Droz, and J. Bailat. Thin-film silicon solar cell technology. *Progress in Photovoltaics Research and Applications*, 12(2-3):113–142, 3 2004.

[46] Peter N. Ciesielski, Frederick M. Hijazi, Amanda M. Scott, Christopher J. Faulkner, Lisa Beard, Kevin Emmett, Sandra J. Rosenthal, David Cliffel, and G. Kane Jennings. Photosystem I – Based biohybrid photoelectrochemical cells. *Bioresource Technology*, 101(9):3047–3053, 1 2010.

[47] Omer Yehezkeli, Ran Tel-Vered, Julian Wasserman, Alexander Trifonov, Dorit Michaeli, Rachel Nechushtai, and Itamar Willner. Integrated photosystem II-based photo-bioelectrochemical cells. *Nature Communications*, 3(1), 3 2012.

[48] Elshan Musazade, Roman Voloshin, Nathan Brady, Jyotirmoy Mondal, Samaya Atashova, Sergey K. Zharmukhamedov, Irada Huseynova, Seeram Ramakrishna, Mohammad Mahdi Najafpour, Jian-Ren Shen, Barry D. Bruce, and Suleyman I. Allakhverdiev. Biohybrid solar cells: Fundamentals, progress, and

challenges. *Journal of Photochemistry and Photobiology C Photochemistry Reviews*, 35:134–156, 4 2018.

[49] J.H. Wohlgemuth and S. Narayanan. Buried contact concentrator solar cells. In *The Conference Record of the Twenty-Second IEEE Photovoltaic Specialists Conference - 1991*, pages 273–277 vol.1, 1991.

[50] D. Jordan and J.P. Nagle. Buried contact concentrator solar cells. *Progress in Photovoltaics: Research and Applications*, 2:171–176, 1994.
.

[51] Vasilis Fthenakis and Hyung Chul Kim. Life-cycle uses of water in U.S. electricity generation. *Renewable and Sustainable Energy Reviews*, 14(7):2039–2048, 3 2010.

[52] Vasilis Fthenakis. Considering the total cost of electricity from sunlight and the alternatives [Point of view]. *Proceedings of the IEEE*, 103(3):283–286, 3 2015.

[53] Ken Zweibel, James Mason, and Vasilis Fthenakis. A solar Grand Plan. *Scientific American*, 2 2024.

[54] Abhijit Supekar, Ramesh Kapadnis, Sanjay Bansode, Pankaj Bhujbal, S Kale, Sandesh Jadkar, and Habib Pathan. Cadmium Telluride/Cadmium Sulfide Thin Films Solar Cells: A review. *ES Energy and Environments*, 1 2020.

[55] U.S. department of energy. "doe solar energy technologies program peer review". In *2010 SOLAR PROGRAM PEER REVIEW REPORT: An Independent Evaluation of Program Activities for FY2009 and FY2010*, 2010.

[56] S. C. Bhatia. *Advanced Renewable Energy Systems, (Part 1 and 2)*. WPI Publishing, 4 2014.

[57] Nikola Papež, Rashid Dallaev, Ştefan Ţălu, and Jaroslav Kaštyl. Overview of the current state of gallium Arsenide-Based solar cells. *Materials*, 14(11):3075, 6 2021.

[58] S.J. Moss and A. Ledwith. *Chemistry of the semiconductor industry*. Springer Science and Business Media, 2 1989.

[59] Delia J. Milliron, Ilan Gur, and A. Paul Alivisatos. Hybrid Organic–Nanocrystal solar cells. *MRS Bulletin*, 30(1):41–44, 1 2005.

[60] Sean E. Shaheen, David S. Ginley, and Ghassan E. Jabbour. Organic-Based Photovoltaics: Toward Low-Cost power generation. *MRS Bulletin*, 30(1):10–19, 1 2005.

[61] Brian R. Saunders and Michael L. Turner. Nanoparticle–polymer photovoltaic cells. *Advances in Colloid and Interface Science*, 138(1):1–23, 10 2007.

[62] E. Kymakis and G. A. J. Amaratunga. Single-wall carbon nanotube/conjugated polymer photovoltaic devices. *Applied Physics Letters*, 80(1):112–114, 1 2002.

[63] N. S. Sariciftci, L. Smilowitz, A. J. Heeger, and F. Wudl. Photoinduced Electron Transfer from a Conducting Polymer to Buckminsterfullerene. *Science*, 258(5087):1474–1476, 11 1992.

[64] Frederik C. Krebs. Fabrication and processing of polymer solar cells: A review of printing and coating techniques. *Solar Energy Materials and Solar Cells*, 93(4):394–412, 12 2008.

[65] American Solar Energy Society. Monocrystalline vs Polycrystalline Solar Panels | American Solar Energy Society.

[66] Christoph J. Brabec. Organic photovoltaics: technology and market. *Solar Energy Materials and Solar Cells*, 83(2-3):273–292, 4 2004.

[67] Fraunhofer Institute for Solar Energy Systems. Photovoltaics report.

[68] Singh H. K. Sarojwal A., Katiyar A. Transparent solar cells: A powerful and affordable source of energy. *International Journal of Mechanical Engineering*, 2021.

[69] Amy J.C. Trappey, Charles V. Trappey, Gilbert Y.P. Lin, and Yu-Sheng Chang. The analysis of renewable energy policies for the Taiwan Penghu island administrative region. *Renewable and Sustainable Energy Reviews*, 16(1):958–965, 10 2011.

[70] Mohammad Hossein Ahmadi, Mahyar Ghazvini, Milad Sadeghzadeh, Mohammad Alhuyi Nazari, Ravinder Kumar, Abbas Naeimi, and Tingzhen Ming. Solar power technology for electricity generation: A critical review. *Energy Science and Engineering*, 6(5):340–361, 9 2018.

[71] Neelam Rathore, Narayan Lal Panwar, Fatiha Yettou, and Amor Gama. A comprehensive review of different types of solar photovoltaic cells and their applications. *International Journal of Ambient Energy*, 42(10):1200–1217, 3 2019.

[72] Farzad Jamaatisomarin, Ruqi Chen, Sajed Hosseini-Zavareh, and Shuting Lei. Laser Scribing of Photovoltaic Solar Thin Films: a review. *Journal of Manufacturing and Materials Processing*, 7(3):94, 5 2023.

[73] Erteza Tawsif Efaz, Md Meganur Rhaman, Safayat Al Imam, Khandaker Lubaba Bashar, Fahmid Kabir, Md Ehasan Mourtaza, Syed Nazmus Sakib, and F. A. Mozahid. A review of primary technologies of thin-film solar cells. *Engineering Research Express*, 3(3):032001, 9 2021.

[74] Taesoo D. Lee and Abasifreke U. Ebong. A review of thin film solar cell technologies and challenges. *Renewable and Sustainable Energy Reviews*, 70:1286–1297, 12 2016.

[75] Xiangbo Song, Xu Ji, Ming Li, Weidong Lin, Xi Luo, and Hua Zhang. A review on development prospect of CZTS based thin film solar cells. *International Journal of Photoenergy*, 2014:1–11, 1 2014.

[76] B. Stegemann, F. Fink, V. Quaschning, R. Schlatmann, B. Rau, I. Dirnstorfer, J. Bonse, H. Endert, H.-u. Pahl, M. Richter, M. Schüle, and C. Schultz. P1,

P2 and P3 Structuring of CIGSE Solar Cells With A Single Laser Wavelength. *26th European Photovoltaic Solar Energy Conference and Exhibition*, pages 2540–2543, 10 2011.

[77] A. Wehrmann, H. Schulte-Huxel, M. Ehrhardt, D. Ruthe, K. Zimmer, A. Braun, and S. Ragnow. Change of electrical properties of CIGS thin-film solar cells after structuring with ultrashort laser pulses. *Proceedings of SPIE, the International Society for Optical Engineering/Proceedings of SPIE*, 7921:79210T, 1 2011.

[78] Felix Utama Kosasih, Lucija Rakocevic, Tom Aernouts, Jef Poortmans, and Caterina Ducati. Electron microscopy characterization of P3 lines and Laser Scribing-Induced perovskite decomposition in perovskite solar modules. *ACS Applied Materials and Interfaces*, 11(49):45646–45655, 10 2019.

[79] Keith G. Brooks and Mohammad Khaja Nazeeruddin. Laser processing methods for perovskite solar cells and modules. *Advanced Energy Materials*, 11(29), 6 2021.

[80] Tai-Wook Kim, Jeong-Yun Lee, Do-Hun Kim, and Heui-Jae Pahk. Ultra-short laser patterning of thin-film CIGS solar cells through glass substrate. *International Journal of Precision Engineering and Manufacturing*, 14(8):1287–1292, 8 2013.

[81] Shiro Nishiwaki, Andreas Burn, Stephan Buecheler, Martin Muralt, Sönke Pilz, Valerio Romano, Reiner Witte, Lukas Krainer, Gabriel J. Spühler, and Ayodhya N. Tiwari. A monolithically integrated high-efficiency Cu(In,Ga)Se2 mini-module structured solely by laser. *Progress in Photovoltaics Research and Applications*, 23(12):1908–1915, 2 2015.

[82] F. Fink, B. Stegemann, V. Quaschning, B. Rau, R. Schlatmann, C.A. Kaufmann, M. Weizman, M. Schuele, C. Schultz, and K. Stelmaszczyk. Investigation of Thin-Film CIGS Degradation under P2 Scribe Laser Illumination.

29th European Photovoltaic Solar Energy Conference and Exhibition, pages 1763–1769, 11 2014.

[83] Shuting Lei, Xin Zhao, Xiaoming Yu, Anming Hu, Sinisa Vukelic, Martin B. G. Jun, Hang-Eun Joe, Y. Lawrence Yao, and Yung C. Shin. Ultrafast Laser Applications in Manufacturing Processes: A State-of-the-Art Review. *Journal of Manufacturing Science and Engineering*, 142(3), 1 2020.

[84] Duc Hong Doan, Ryoichi Iida, Byunggi Kim, Isao Satoh, and Kazuyoshi Fushinobu. Bessel beam laser-scribing of thin film silicon solar cells by ns pulsed laser. *Journal of Thermal Science and Technology*, 11(1):JTST0011, 1 2016.

[85] Bert Stegemann and Christof Schultz. Laser patterning of thin films. *digital Encyclopedia of Applied Physics*, pages 1–30, 8 2019.

[86] Yukiko Kamikawa-Shimizu, Hironori Komaki, Akimasa Yamada, Shogo Ishizuka, Masayuki Iioka, Hirofumi Higuchi, Miwako Takano, Koji Matsubara, Hajime Shibata, and Shigeru Niki. Highly efficient CU(IN,GA)SE2Thin-Film submodule fabricated using a Three-Stage process. *Applied Physics Express*, 6(11):112303, 11 2013.

[87] Erik Wallin, Ulf Malm, Tobias Jarmar, Olle Lundberg Marika Edoff, and Lars Stolt. World-record Cu(In,Ga)Se2-based thin-film sub-module with 17.4 *Progress in Photovoltaics Research and Applications*, 20(7):851–854, 5 2012.

[88] Reiner Witte, Bruno Frei, Stefan Schneeberger, Stephan Bücheler, Shiro Nishiwaki, Andreas Burn, Martin Muralt, Valerio Romano, and Lukas Krainer. Investigation of a reliable all-laser scribing process in thin film Cu(In,Ga)(S,Se)2manufacturing. *Proceedings of SPIE, the International Society for Optical Engineering/Proceedings of SPIE*, 8607:86071B, 3 2013.

[89] Bert Stegemann, Frank Fink, Heinrich Endert, Manuel Schüle, Christof Schultz, Volker Quaschning, Jürgen Niederhofer, and Hans-Ulrich Pahl. Novel

concept for laser patterning of thin film solar cells. *Laser Technik Journal*, 9(1):25–29, 1 2012.

[90] Paulius Gečys, Edgaras Markauskas, Shiro Nishiwaki, Stephan Buecheler, Ronny De Loor, Andreas Burn, Valerio Romano, and Gediminas Račiukaitis. CIGS thin-film solar module processing: case of high-speed laser scribing. *Scientific Reports*, 7(1), 1 2017.

[91] Thomas Feurer, Patrick Reinhard, Enrico Avancini, Benjamin Bissig, Johannes Löckinger, Peter Fuchs, Romain Carron, Thomas Paul Weiss, Julian Perrenoud, Stephan Stutterheim, Stephan Buecheler, and Ayodhya N. Tiwari. Progress in thin film CIGS photovoltaics – Research and development, manufacturing, and applications. *Progress in Photovoltaics Research and Applications*, 25(7):645–667, 10 2016.

[92] David J. Hwang, Seungkuk Kuk, Zhen Wang, Shi Fu, Tao Zhang, Gayeon Kim, Won Mok Kim, and Jeung-Hyun Jeong. Laser scribing of CIGS thin-film solar cell on flexible substrate. *Applied Physics A*, 123(1), 12 2016.

[93] A. Bosio, M. Sozzi, D. Menossi, S. Selleri, A. Cucinotta, and N. Romeo. Polycrystalline CdTe thin film mini-modules monolithically integrated by fiber laser. *Thin Solid Films*, 562:638–647, 4 2014.

[94] Fabio Giovanardi, Francesco Bissoli, Edmondo Gilioli, Giovanna Trevisi, Massimo Mazzer, and Stefano Selleri. Ultrashort pulse laser scribing of CIGS-based thin film solar cells. *2020 Italian Conference on Optics and Photonics (ICOP)*, 9 2020.

[95] Govind P. Agrawal. *Fiber-Optic communication systems*. John Wiley and Sons, 6 2021.

[96] Johan Meyer, Justice Sompo, and Suné Von Solms. *Fiber lasers*. 12 2021.

[97] Matan. Fiber Lasers | How it works, Application and Advantages, 10 2023.

[98] Walter Koechner. *Solid-State Laser Engineering*. 1 1988.

[99] Hatem Krema. *Principles of laser therapy*. 1 2019.

[100] K. Himeno. Basics and features of high-power fiber laser. *Fujikura Technical Review no. 44*, 2015.

[101] Galina Nemova. Brief review of recent developments in fiber lasers. *Applied Sciences*, 14(6):2323, 3 2024.

[102] Rüdiger Paschotta. *Encyclopedia of Laser Physics and Technology*. Wiley-VCH, 12 2008.

[103] Michel J.F. Digonnet. *Rare-Earth-Doped fiber lasers and amplifiers, revised and expanded*. 5 2001.

[104] Kobi Aflalo, Moshe Ben-David, Adrian Stern, and Irit Juwiler. Theoretical investigation of using a yellow (577nm) laser for diabetic retinopathy. *OSA Continuum*, 3(11):3253, 11 2020.

[105] Yasushi Fujimoto, Osamu Ishii, and Masaaki Yamazaki. 575 nm laser oscillation in Dy3+-doped waterproof fluoro-aluminate glass fiber pumped by violet GaN laser diodes. *Proceedings of SPIE, the International Society for Optical Engineering/Proceedings of SPIE*, 1 2011.

[106] Md Ziaul Amin, Matthew Majewski, and Stuart D. Jackson. Yellow emission from dysprosium-doped ZBLAN fiber laser. *Proceedings of the SPIE, Volume 11260, id. 112601K 7 pp. (2020).*, 2 2020.

[107] Jinhai Zou, Tianran Li, Yanbo Dou, Jin Li, Nan Chen, Yikun Bu, and Zhengqian Luo. Direct generation of watt-level yellow Dy3+-doped fiber laser. *Photonics Research*, 9(4):446, 11 2020.

[108] Joel M. Krauss and Carmen A. Puliafito. Lasers in ophthalmology. *Lasers in Surgery and Medicine*, 17(2):102–159, 1 1995.

[109] Foroogh Khozeymeh, Federica Poli, Wahida Chowdhury, and Annamaria Cucinotta. Analysis and optimization of Dysprosium-doped yellow fiber lasers for ophthalmology applications. *IEEE photonics journal*, 16(1):1–8, 12 2023.

[110] M. Z. Amin, S. D. Jackson, and M. R. Majewski. Experimental and theoretical analysis of Dy3+-doped fiber lasers for efficient yellow emission. *Applied Optics*, 60(16):4613, 5 2021.

[111] Foroogh Khozeymeh Sarbishe. Experimental characterization and modelling of specialty optical fibres for bio-medical applications. 1 2024.

[112] Giacomo Bolognesi, Daniela Parisi, Davide Calonico, Giovanni Antonio Costanzo, Filippo Levi, Philip Werner Metz, Christian Kränkel, Günter Huber, and Mauro Tonelli. Yellow laser performance of dy3+ in co-doped dy,tb:liluf$_4$. $OpticsLetters, 39(23) : 6628, 112014$.

[113] Lei Zhang, Huawei Jiang, Shuzhen Cui, Jinmeng Hu, and Yan Feng. Versatile Raman fiber laser for sodium laser guide star. *Laser and Photonics Review*, 8(6):889–895, 7 2014.

[114] Daniel Lavinsky, Jenny Wang, Philip Huie, Roopa Dalal, Seung Jun Lee, Dae Yeong Lee, and Daniel Palanker. Nondamaging retinal laser therapy: Rationale and applications to the macula. *Investigative Ophthalmology and Visual Science*, 57(6):2488, 5 2016.

[115] Christopher F. Blodi, Stephen R. Russell, Jose S. Pulido, and James C. Folk. Direct and Feeder Vessel Photocoagulation of Retinal Angiomas with Dye Yellow Laser. *Ophthalmology*, 97(6):791–797, 6 1990.

[116] Susanne E. McCoy MBBS. Copper bromide laser treatment of facial telangiectasia: Results of patients treated over five years. *Copper bromide laser treatment of facial telangiectasia: Results of patients treated over five years*, 1998.

[117] Bernard Jacquier. *Rare Earth-Doped fiber lasers and amplifiers*. Springer eBooks.

[118] Setsuhisa Tanabe, Teiichi Hanada, Masayuki Watanabe, Tetsusuke Hayashi, and Naohiro Soga. Optical Properties of Dysprosium-Doped Low-Phonon-

Energy Glasses for a Potential 1.3 micro-meter Optical Amplifier. *Journal of the American Ceramic Society*, 78(11):2917–2922, 11 1995.

[119] P. C. Becker, N. A. Olsson, and J. R. Simpson. *Erbium-Doped Fiber Amplifiers: Fundamentals and Technology*. Academic Press, 3 1999.

[120] Stefano Selleri, Luca Vincetti, and Annamaria Cucinotta. *Optical and photonic components*. Societa Editrice Esculapio, 1 2015.

Acknowledgement

I would like to express my sincere gratitude to everyone who contributed to this research. Special thanks go to Professor Annamaria Cucinotta, for her invaluable guidance, support, and encouragement throughout this project. I am also deeply grateful to my research group and colleagues at the University of Parma. for their constructive discussions and assistance during the experimental phase. I am immensely grateful to my friend Hossein, who is like my brother, whose support and encouragement have been instrumental in reaching this milestone. Lastly, I would like to extend my thanks to my family, my brother Dip, and his wife Sabrina Zerin, for their unwavering support and patience during this journey.